Intricate Dynamics of Droplet-Substrate Interactions Beyond Conventional Limits

Wenge Huang

Dissertation submitted to the faculty of the Virginia Polytechnic Institute and State
University in partial fulfillment of the requirements for the degree of

Doctor of Philosophy
In
Mechanical Engineering

Jiangtao Cheng, Chair
Wei Zhou
Yang Liu
Mark Paul
Jonathan Boreyko

December 12, 2024
Blacksburg, VA

Keywords: droplet; bubble; capillary wave; evaporation; boiling; jumping.

Intricate Dynamics of Droplet-Substrate Interactions Beyond Conventional Limits

Wenge Huang

ABSTRACT

Droplet dynamics, encompassing relatively static processes such as evaporation to more vigorous phenomena like self-propelled jumping, are of considerable interest due to their significance in both natural phenomena and practical applications. These behaviors are pivotal in facilitating mass, momentum, and energy transfer between droplets and their surroundings, with applications spanning phase-change heat transfer, material transport, surface engineering, and energy optimization. While droplet dynamics have been extensively studied over the past several decades, advancements in surface engineering, such as the development of functional surface materials, have introduced novel mechanisms governing droplet behavior. These complex droplet-substrate interactions exhibit intricate dynamics that transcend conventional understanding and remain inadequately explored. This dissertation investigates the intricate dynamics of droplet-substrate interactions, spanning processes from evaporation to out-of-surface jumping, offering insights into the interplay of thermal, capillary, and inertial forces that govern these phenomena.

The evaporation of sessile water droplets on heated microstructured superhydrophobic surfaces is experimentally and theoretically explored across a temperature range of 20 - 120 °C. A thermal circuit model is developed to decouple heat and mass transfer contributions from the droplet cap and base. The findings reveal that substrate roughness and temperature significantly influence evaporation behavior, with suppressed boiling observed due to evaporative cooling. The results elucidate the role of substrate microstructures in modulating heat transfer pathways, advancing the understanding of evaporation dynamics on non-wetting surfaces.

As the substrate temperature increases, vapor bubbles form at the droplet base, transitioning the droplet into the nucleate boiling regime. At relatively low temperatures, droplets exhibit versatile jumping behaviors similar to the high-temperature Leidenfrost effect. Unlike the traditional Leidenfrost effect, which occurs above 230 °C, fin-array-like

micropillars enable water microdroplets to levitate and jump off the surface within milliseconds at just 130 °C, triggered by the inertia-controlled growth of individual vapor bubbles at the droplet base. The droplet jumping, driven by momentum interactions between the expanding vapor bubble and the droplet, can be modulated by adjusting the thermal boundary layer thickness through pillar height. This allows for precise control over bubble expansion, switching between inertia-controlled and heat-transfer-limited modes. These two modes lead to distinct droplet jumping behaviors: one characterized by constant velocity and the other by constant energy.

Bubble expansion provides an effective method for achieving droplet out-of-surface jumping. To better understand the gas-liquid-substrate three-phase interactions, we inject an air bubble into a sessile droplet to explore the bubble burst-induced droplet jumping process. Upon bubble bursting, the surface energy released from both the inner and outer surfaces of the bubble drives the droplet jumping. Specifically, the bursting bubble generates capillary waves that propagate nearly vertically towards the substrate, causing the droplet to retract with minimal spreading upon impact with the capillary waves. When sufficient surface energy is released, this bubble burst-based strategy facilitates efficient momentum transfer through direct and localized capillary wave-solid surface interactions, enabling the lifting of puddles on the centimeter scale.

Intricate Dynamics of Droplet-Substrate Interactions Beyond Conventional Limits

Wenge Huang

GENERAL AUDIENCE ABSTRACT

Have you ever noticed how water droplets can sit on a surface, evaporate into thin air, or even jump away on their own? These fascinating behaviors might seem simple, but they play a big role in how heat, energy, and even materials move around in nature and in technology. My research looks at how droplets behave in different situations, from slowly disappearing through evaporation to suddenly jumping off a surface, and what makes these behaviors possible.

One part of my work explores how tiny droplets evaporate on special surfaces designed to repel water. I found that the texture of the surface and how hot it is can change how quickly droplets evaporate. Interestingly, the surfaces I studied keep water from boiling, even at high temperatures, because the droplets cool themselves as they evaporate.

Another part of my research investigates something even more dramatic: droplets jumping off surfaces. By using surfaces covered in tiny structures, I discovered that droplets can jump away at temperatures much lower than expected—around 130 °C instead of over 230 °C, which is typical in other scenarios. This happens because bubbles forming underneath the droplet give it a little “push” that helps it leap into the air.

Finally, I studied how bursting a bubble inside a droplet can make the entire droplet jump. The burst sends out ripples, like waves in a pond, but these waves hit the surface below the droplet and bounce it upward. By tweaking the surface texture, we can control this jumping behavior and even lift very large droplets. These findings could help design surfaces that clean themselves or remove liquids quickly and efficiently.

Acknowledgements

I would like to express my deepest gratitude to my academic advisor, Dr. Jiangtao Cheng. His unwavering support and respect for my research interests and ideas have been instrumental in shaping my dissertation and enabling me to pursue my Ph.D. studies. His mentorship and insightful guidance have not only inspired my work but also motivated me to grow into a better researcher, laying a strong foundation for my future career.

I am also profoundly thankful to the professors on my committee—Dr. Wei Zhou, Dr. Jonathan Boreyko, Dr. Yang Liu, and Dr. Mark Paul—for their generous commitment of time and their invaluable advice on my research. Their expertise and thoughtful feedback have greatly enriched my academic journey.

A heartfelt thanks goes to my lab members and friends, whose support and camaraderie have been indispensable throughout these five years. Dr. Xukun He, Dr. Lei Zhao, Mr. Yang Li, and Mr. Mohammad Shamsodini Lori have shared both the joyful moments and the challenges of this journey, making it all the more rewarding and colorful.

I owe my sincerest gratitude to my parents, Jiangang Huang and Yunjiao Li, for their unconditional support and encouragement. Their steadfast belief in me has been a source of strength during moments of doubt or difficulty.

I am grateful for the financial support provided by my department and the National Science Foundation, as well as the resources and technical assistance offered by Advanced Research Computing and the Cleanroom at Virginia Tech. Their contributions have been essential to the successful completion of my Ph.D. work.

To everyone who has played a part in this journey, I extend my deepest appreciation. Thank you for making this experience both meaningful and memorable.

Table of Contents

List of Figures

Chapter 1

Introduction

Droplet dynamics encompass a broad spectrum of behaviors, ranging from steady processes like evaporation [1-5] to highly energetic phenomena such as self-propelled jumping [6-8]. These processes are integral to the exchange of mass, momentum, and energy between droplets and their surrounding environment, shaping various natural and engineered systems. For instance, evaporation plays a critical role in environmental water cycles and cooling technologies, while droplet jumping has applications in self-cleaning surfaces, condensation heat transfer enhancement, and anti-icing strategies. Collectively, these behaviors impact key areas such as phase-change heat transfer [9-11], material transport in microfluidic systems [12, 13], surface design for improved wettability control [14, 15], and energy-efficient thermal management solutions.

Over the past several decades, substantial progress has been made in understanding the basic mechanisms governing droplet dynamics. Traditional studies have largely focused on the fundamental forces like surface tension, viscosity, and gravity. However, recent advancements in surface engineering, such as the development of functional surface materials [16, 17], have introduced new factors that significantly alter droplet behavior. These materials, including microstructured and superhydrophobic surfaces, have led to novel mechanisms such as droplet jumping and enhanced evaporation, presenting new challenges in understanding the complex interactions between droplets and substrates.

Although droplet dynamics have been extensively studied, the intricate nature of droplet-substrate interactions remains insufficiently explored. The dynamics of these interactions often transcend conventional models, with new phenomena emerging that are not yet fully understood. As surface engineering techniques continue to advance, new and complex behaviors are being uncovered, requiring a more integrated approach that combines experimental studies with theoretical and computational modeling.

1.1. The wetting state of a droplet.

When a droplet is deposited on a solid surface, its shape is primarily dictated by the surface properties, which determine the droplet’s wetting state [18-20]. Generally, two extreme wetting scenarios are observed. In the first scenario, known as complete wetting, a droplet brought into contact with the solid surface spreads spontaneously, forming a thin liquid film with a contact angle θ approaching 0°. This occurs when the surface energy favors maximum contact between the liquid and the solid. In contrast, the second extreme, termed complete non-wetting or complete drying, occurs when the liquid minimizes its interaction with the substrate. In this case, the droplet retains a nearly spherical shape, maintaining a contact angle θ close to 180°, indicative of negligible contact with the surface. The first theoretical investigation of the droplet wetting state was conducted by Young and Laplace [21], based on the assumption of an ideal surface that is perfectly flat and chemically homogeneous. Their analysis focused on the force balance at the three-phase contact line, where the gas, liquid, and solid phases meet as shown in Fig. 1-1. In equilibrium, this force balance involves the interfacial tensions: the solid-gas interfacial tension γ_{sg}, liquid-solid interfacial tension γ_{sl}, and liquid-vapor interfacial tension γ_{lg}.

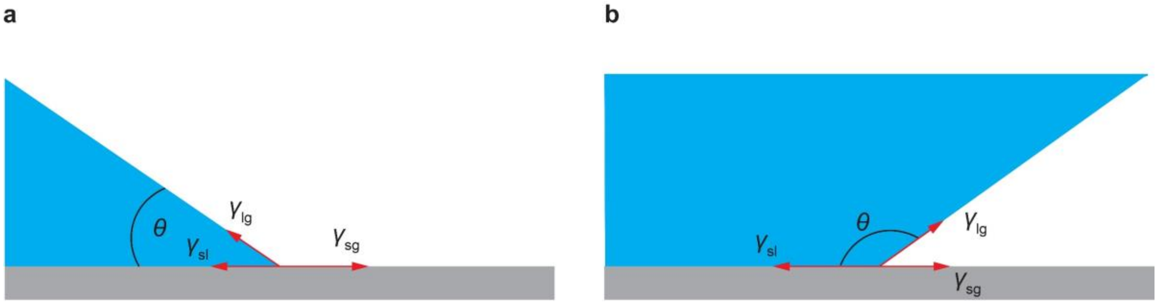

Figure 1-1. Diagram of surface tension balance at the three-phase contact line. a Surface tension balance on hydrophilic surface. **b** Surface tension balance on hydrophobic surface.

$$\gamma_{sg} = \gamma_{sl} + \gamma_{lg} \cos\theta \tag{1-1}$$

In reality, even surfaces that appear flat are inherently rough at the micro- or nanoscale, featuring intricate structures that significantly influence droplet behavior. The contact angle observed on such surfaces is an apparent contact angle, which often differs from the intrinsic contact angle predicted by the Young-Laplace equation for ideal surfaces. To address this mismatch, Wenzel [22] proposed a model in 1936 that incorporates surface roughness r —a ratio of the actual surface area to the apparent surface area of the rough surface — to adjust the apparent contact angle. According to the Wenzel model, the relationship between the apparent contact angle θ^* and the intrinsic contact angle θ is given by:

$$\cos\theta^* = r\cos\theta \tag{1-2}$$

For a droplet to conform to the Wenzel model, it must fully penetrate the rough structures of the solid surface, ensuring complete contact between the liquid and the substrate as shown in Fig. 1-2 **a**. A droplet in such a configuration is termed a Wenzel state droplet. In contrast, another wetting state, proposed by Cassie and Baxter [23], arises when the droplet rests on the tips of the microstructures, with air pockets trapped beneath it as shown in Fig. 1-2 **b**. This configuration, often referred to as the Cassie-Baxter state, is characterized by a composite interface consisting of both solid and air. The apparent contact angle θ^* in this state is related to the intrinsic contact angle θ by the equation:

$$\cos\theta^* = f(1+\cos\theta) - 1 \tag{1-3}$$

where f represents the solid-liquid interface fraction.

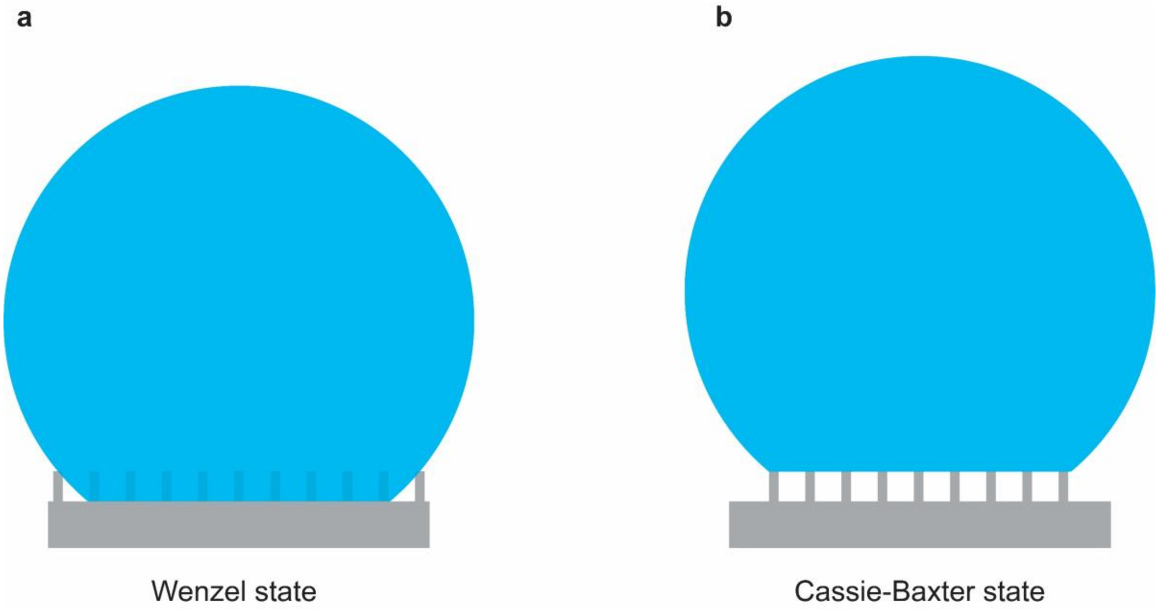

Figure 1-2. Diagram of a sessile droplet in a Wenzel state and in b Cassie-Baxter state droplet

The equilibrium contact angle θ_c for the Wenzel-to-Cassie transition can be determined by balancing the apparent contact angle equations for these two states. The relationship is given by:

$$\cos\theta_c = \frac{f-1}{r-f} \tag{1-4}$$

To ensure a droplet remains in the Wenzel state, the equilibrium contact angle should exceed the intrinsic contact angle θ.

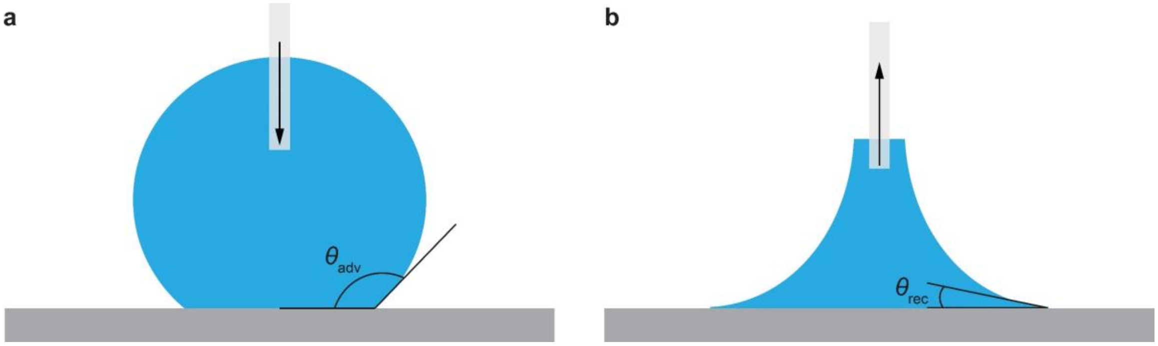

Figure 1-3. Diagram of dynamic contact angle. a Advancing contact angle. **b** Receding contact angle.

Over the past 15 years, significant advancements have deepened our understanding of wetting phenomena, with dynamic contact angles emerging as a pivotal metric. Unlike static contact angles, which offer only a limited snapshot of droplet behavior, dynamic contact angles are measured when a liquid droplet moves across a solid surface, causing the three-phase contact line to be in motion. These angles are characterized by two key values: the advancing contact angle, observed as the droplet spreads, and the receding contact angle, observed as the droplet shrinks. The difference between these values, known as contact angle hysteresis, reflects the influence of surface roughness and heterogeneity. By inherently accounting for pinning effects—where surface imperfections hinder the motion of the contact line—dynamic contact angles provide a more comprehensive framework for quantifying wetting. This ability to capture the interplay between droplet movement and surface properties has solidified their importance in understanding the complex wetting behaviors of liquids on diverse substrates.

1.2. Droplet Evaporation.

Evaporation of a sessile droplet occurs spontaneously due to the gradient in vapor concentration between the liquid surface and the surrounding environment. The evaporation of droplets is a fundamental process with wide-ranging applications, including printing technologies, thermal management, surface engineering, microfluidics, artistic methods, and biomedical research. In 1963, Mangel and Baer conducted a pioneering study on the evaporation of sessile droplets on solid surfaces [24]. They observed that during the initial stages of evaporation, the droplet volume decreased primarily through a reduction in the contact angle, while the contact radius remained constant as the droplet stayed pinned to the surface. As evaporation progressed, the contact angle eventually reached a threshold, known as the receding contact angle. At this point, the liquid-solid contact area began to shrink, while the contact angle remained constant. In 1977, Picknett and Bexon [25] expanded upon this understanding by identifying two distinct evaporation modes for droplets on smooth surfaces: the constant-contact-angle (CCA) mode and the constant-contact-radius (CCR) mode as shown in Fig. 1-3.

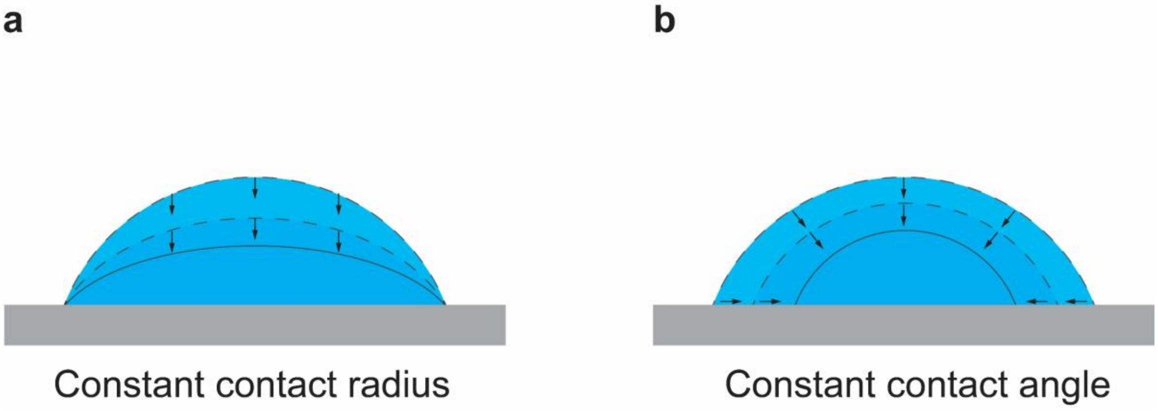

Figure 1-4. Diagram of droplet contact radius and contact angle dynamics during evaporation. a Constant contact radius (CCR) mode**. b** Constant contact angle (CCA) mode.

The evaporation process of a sessile droplet can be theoretically modeled by solving the Laplace equation in toroidal coordinates, which describes the vapor-diffusion process around the droplet [26]. This vapor-diffusion model accounts for the nonuniform vapor concentration distribution in the vicinity of the droplet and provides an exact solution for the evaporation flux $J_m(r)$ along the droplet's surface.

$$J_m(r) = \frac{D_{\mathrm{diff}}\big(c_{\mathrm{s}}(T_{\mathrm{i}}) - H_{\mathrm{h}} c_{\mathrm{s}}(T_\infty)\big)}{r_c} \cdot j(\theta) \qquad (1\text{-}5)$$

$$j(\theta) = \Big[\tfrac{1}{2}\sin(\theta) + \sqrt{2}(\cosh(\beta) + \cos(\theta))^{3/2} \cdot \int_0^\infty \frac{\cos\mathrm{h}(\theta\tau)}{\cos\mathrm{h}(\pi\tau)} \tan\left[(\pi - \theta)\tau\right] \cdot P_{-0.5+i\tau}\big(\cosh(\beta)\big)\tau \cdot \mathrm{d}\,\tau\ \Big] \qquad (1\text{-}6)$$

where D_{diff} represents the diffusion coefficient, c_{s} is the saturated vapor concentration at different temperatures, T_{i} and T_∞ denote the interface temperature and the ambient temperature, respectively, H_{h} is the far-field relative humidity and r_c is the contact radius.

As a result, for a droplet with a given contact angle θ, the evaporation rate of the droplet can be expressed as:

$$\frac{dM}{dt} = \rho_l \frac{dV}{dt} = -\pi r_c D_{\mathrm{diff}}\big(c_{\mathrm{s}}(T_{\mathrm{i}}) - H_{\mathrm{h}} c_{\mathrm{s}}(T_\infty)\big) \cdot f(\theta) \qquad (1\text{-}7)$$

$$f(\theta) = \frac{\sin(\theta)}{1+\cos(\theta)} + 4\int_0^\infty \frac{1+\cos\mathrm{h}(1\theta\tau)}{\sinh(2\pi\tau)} \tan\left[(\pi - \theta)\tau\right] \mathrm{d}\,\tau \qquad (1\text{-}8)$$

where M is the droplet mass, V is the droplet volume, ρ_l is the liquid density and the term $f(\theta)$ is a is a contact angle-dependent factor that captures the asymmetry in evaporation caused by the presence of the substrate. It can be empirically expressed as a finite series [27].

$$f(\theta) = \begin{cases} 0.3183\theta + 0.04796\theta^2 - 0.03072\theta^2 & \left(0 \le \theta \le \frac{\pi}{18}\right) \\ 0.00004479 + 0.3167\theta + 0.058\theta^2 - 0.04439\theta^3 + 0.005165\theta^4 & \left(\frac{\pi}{18} \le \theta \le \pi\right) \end{cases} \qquad (1\text{-}9)$$

1.3. The Leidenfrost effect.

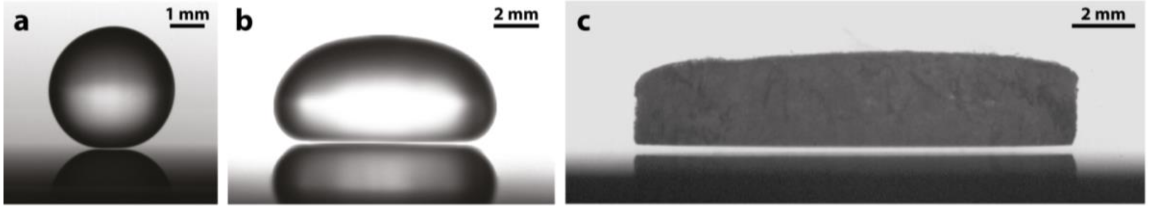

Figure 1-5. Leidenfrost droplets on a hot flat surface at 300 °C. a A small water droplet in the Leidenfrost state. **b** A large water puddle in the Leidenfrost state. **c** A small disk of

dry ice in the Leidenfrost-like hovering state. (Fig. 1, David Quere, Annu. Rev. Fluid Mech. 45:197-215)

The Leidenfrost effect [28-30], observed when a droplet is placed on a substrate at a very high temperature, is a fascinating phenomenon where droplets exhibit blistering or bouncing motions. This effect was first documented by Johann Gottlob Leidenfrost in the 18th century when he noticed that water droplets placed on a hot surface seemed to "skate" across the surface rather than evaporating immediately. The phenomenon occurs when the temperature of the substrate is high enough that the bottom of the droplet vaporizes instantly upon contact, creating a thin insulating layer of vapor. This layer prevents further direct contact between the droplet and the hot surface, allowing the droplet to remain suspended and move across the surface as shown in Fig. 1-4.

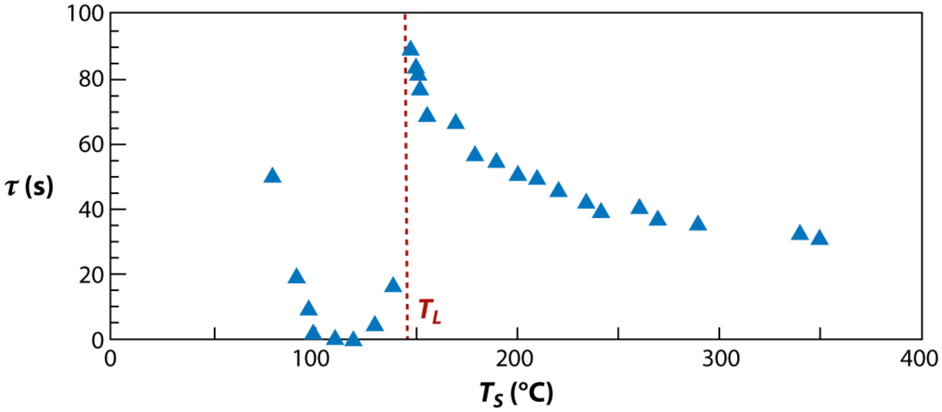

Figure 1-6. Droplet lifetime as a function of substrate temperature. The plotted data represent droplets with a radius of approximately 1 mm deposited on a flat duralumin surface at varying temperatures. (Fig. 2, David Quere, Annu. Rev. Fluid Mech. 45:197-215)

The Leidenfrost point (LFP) is the critical temperature at which a liquid droplet levitates above a heated surface due to the formation of a stable vapor cushion. This behavior is typically determined by plotting droplet lifetime against substrate temperature, as illustrated in Fig 1-5 for a water droplet (1 mm in diameter) on a duralumin plate. Below 100 °C, the droplet rapidly boils upon contact with the surface, resulting in a significant decrease in lifetime, reaching approximately 200 milliseconds at 100 °C. As the substrate temperature rises between 100 °C and 150 °C, the droplet's lifetime increases sharply, signaling the onset of a stable vapor layer beneath the droplet. The temperature corresponding to this maximum lifetime is defined as the Leidenfrost temperature. Beyond the LFP, the droplet lifetime gradually decreases as evaporation continues in the presence of the insulating vapor cushion.

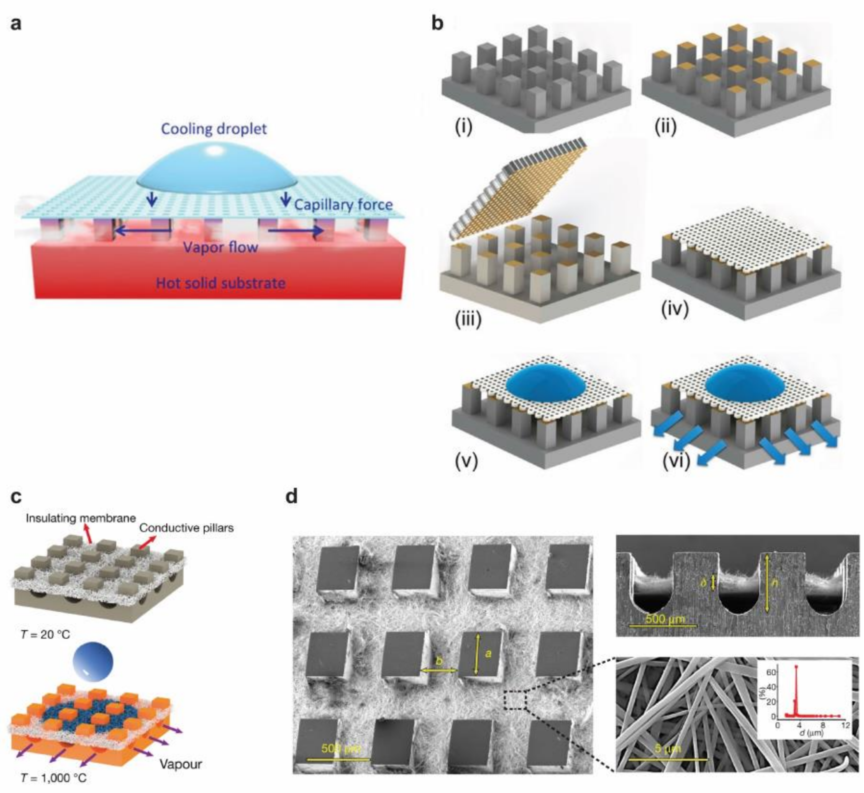

Figure 1-7. Hierarchical structures for enhancing the Leidenfrost point. a A hierarchical structure combining microstructures and nanomembranes. (Figs. 1 and 2, Farokhnia et al, Langmuir 33, 2541-2550, 2017). **b** Schematic illustration of the fabrication steps for a decoupled hierarchical structure. **c** Configuration featuring an array of thick pillars paired with a superhydrophilic membrane. **d** Scanning electron microscopy (SEM) images showcasing the structural details. (Fig.1, Jiang et al. Nature 601, 568-572, 2022).

The Leidenfrost phenomenon significantly hinders heat transfer on high-temperature surfaces by forming a stable vapor layer between the liquid and solid, which increases thermal resistance and reduces cooling efficiency in applications like thermal management and cooling systems. To mitigate this effect, raising the Leidenfrost point (LFP) is crucial, as it delays vapor layer formation and preserves direct liquid-solid contact over a broader temperature range, thereby enhancing heat transfer. This can be achieved through textured and hierarchical structures that improve liquid-solid interactions and facilitate vapor evacuation. Nanostructures, known for their strong capillary wicking, and microstructures, which provide effective vapor pathways, work in tandem to suppress the Leidenfrost phenomenon. For instance, rigid membranes with high thermal conductivity (~30 $W \cdot m^{-1} \cdot K^{-1}$) and one-dimensional nanopores on silicon pillar arrays have demonstrated the ability to raise the LFP to approximately 570°C as shown in Fig.1-6 **a** [31]. Further advancements, such as multiscale anodic alumina membranes and structural thermal armor, have achieved LFPs as high as 1150°C, highlighting their potential for transformative improvements in thermal management and cooling as shown in Fig. 1-6 **b** [32].

On the other hand, Leidenfrost droplets eliminate physical contact between the liquid and the surface, effectively minimizing interfacial hydrodynamic resistance by reducing contact line pinning and solid-liquid friction. This characteristic is particularly advantageous for agile droplet manipulations. Huang et al, [33] demonstrated that through the design of microstructured surfaces, Leidenfrost-like droplet levitation could be activated at a significantly reduced temperature of 130°C, far below the conventional Leidenfrost point. This achievement underscores the potential to harness the benefits of Leidenfrost phenomena while maintaining heat transfer performance, presenting exciting opportunities for future research and practical applications.

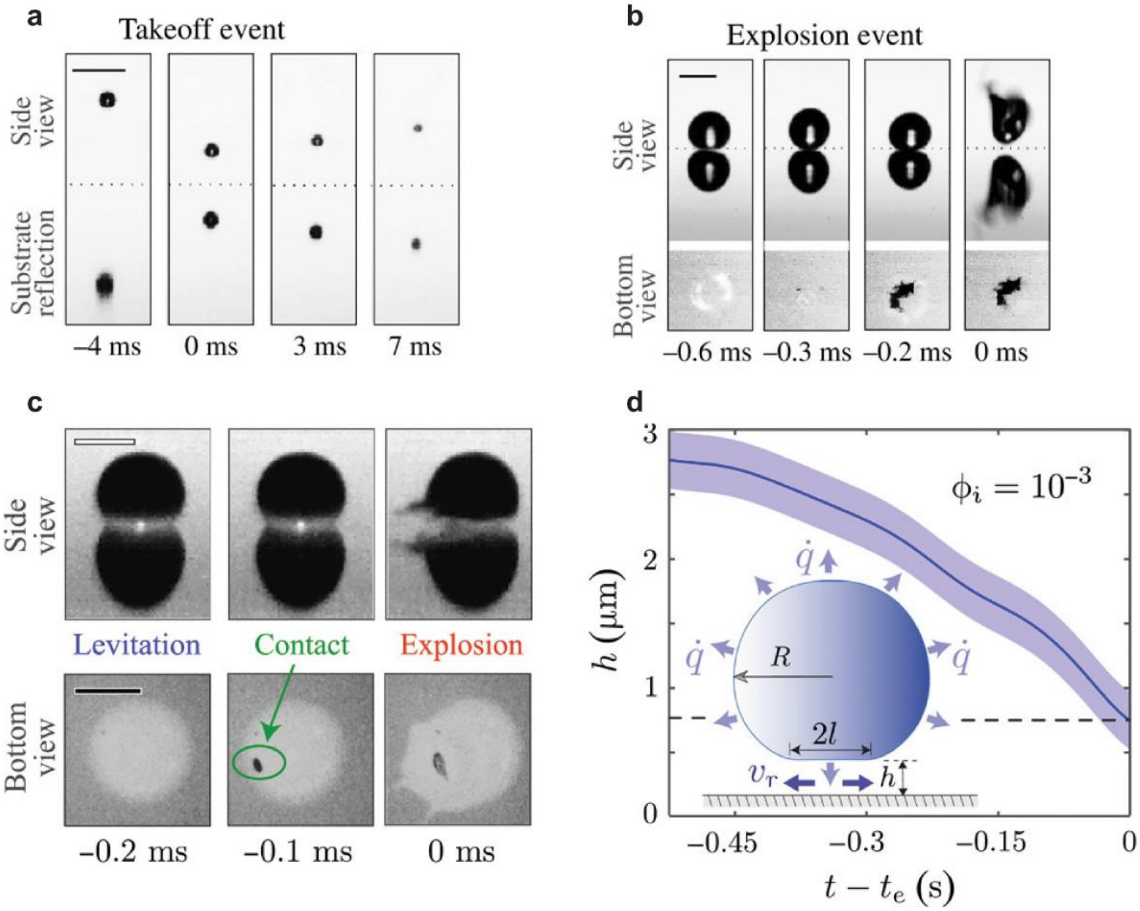

Figure 1-8. Droplet explosion on hot surface. a Sideview of a small ethanol droplet. b Sideview of a large ethanol droplet. c Side and bottom views of a suspension droplet just before and at the point of explosion. D Vapor layer thickness versus time to explosion for an evaporating droplet. (Fig. 1 Lyu et al. Sci. Adv. 2019; 5)

In addition to the jumping phenomena explored in this dissertation, other jumping effects in Leidenfrost drops have been well-documented, particularly those that arise during evaporation. For instance, when the vapor film supporting a Leidenfrost drop suddenly collapses—either due to external disturbances or the evaporation process reaching a critical point—the drop can experience a rapid and unexpected takeoff as shown in Fig. 1-8. This collapse leads to a brief, high-pressure state beneath the droplet, propelling it off the surface. Furthermore, self-takeoff can occur for sufficiently small Leidenfrost drops, where the vapor film is not thick enough to fully support the drop, causing it to lift off spontaneously. These effects are primarily driven by the dynamics of the vapor film and the interaction between the drop and the underlying surface, contributing to the complex behaviors observed during Leidenfrost phenomena. Understanding these existing jumping effects is crucial for advancing the current understanding of droplet dynamics, particularly in the context of the low-temperature Leidenfrost-like jumping behaviors explored in this dissertation, which extend the capabilities of droplet actuation beyond the traditional high-temperature regime.

1.4. Droplet out-of-surface jumping.

The removal of condensed matter from surfaces plays a crucial role in both daily life and industrial processes, including surface cleaning, drying, condensation heat transfer, electrospray printing, and additive manufacturing. Nature-inspired phenomena, such as water droplets jumping and shedding on lotus-leaf-like surfaces, offer a cost-effective solution for surface cleaning. This has spurred growing interest in methods to achieve passive out-of-surface droplet jumping, with two primary strategies being proposed: impact-rebound and coalescence-induced jumping. On superhydrophobic textured surfaces, impinging droplets can exhibit a complete rebound at the end of their retraction. In coalescence-induced jumping, surface energy is released during the coalescence process, triggering the formation of liquid bridges at the droplet's base, which eventually lift the droplet off the surface.

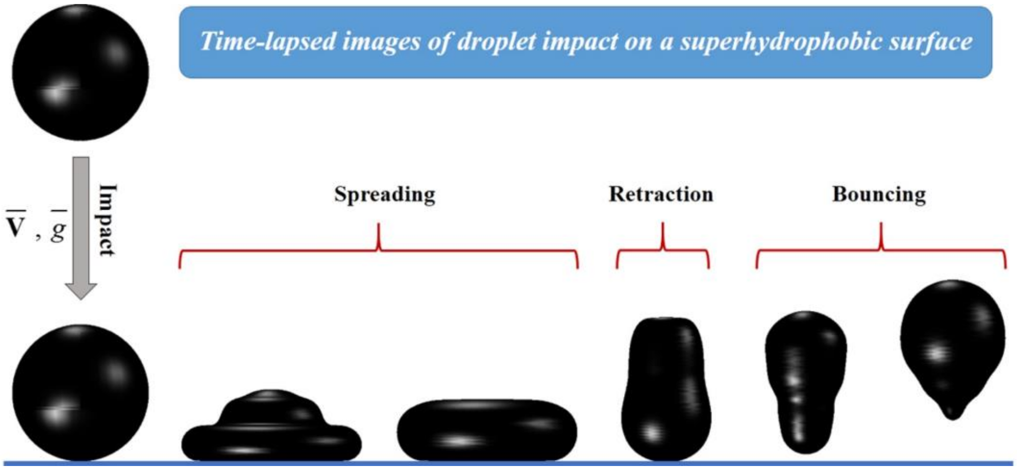

Figure 1-9. Droplet impact and rebound demonstrating out-of-surface jumping. (Fig. 1, Khojasteh et al, J. Ind. Eng. Chem. 42, 1-14, 2016).

Upon impacting a solid surface, a droplet undergoes a sequence of well-defined stages: spreading, retraction, and rebound [34]. Initially, upon contact, the droplet rapidly flattens and spreads radially outward, driven by its inertial forces surpassing the cohesive effects of surface tension. The extent of spreading, characterized by the maximum spreading diameter, is governed by parameters such as impact velocity, surface wettability, and the droplet's physical properties, including viscosity and density. As the droplet reaches its maximum spread, surface tension becomes the dominant force, initiating the retraction phase. During this stage, the liquid retracts toward the droplet's center, restoring its shape and conserving surface energy. The rebound phase follows, during which the combined effects of surface tension and the kinetic energy retained during retraction propel the droplet off the surface.

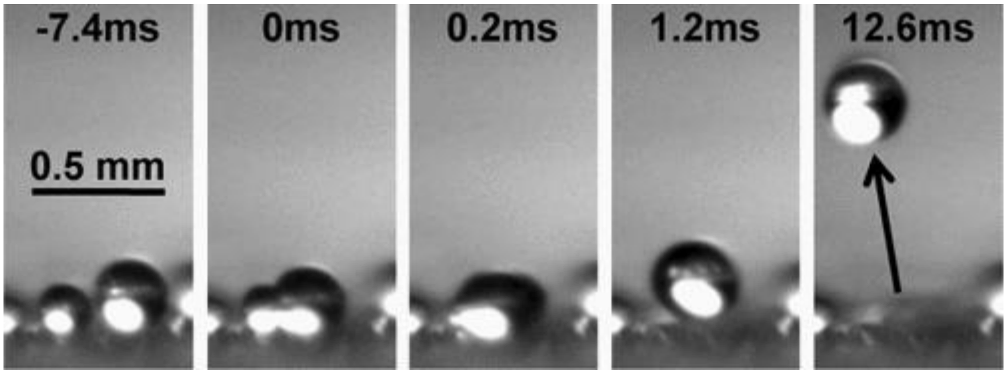

Figure 1-10. Coalescence-induced droplet out-of-surface jumping. (Fig. 3, Boreyko et al, Phy. Rev. Lett. 103, 184501, 2009).

Droplet coalescence-induced jumping is a dynamic process in which two or more droplets merge on a surface, leading to their spontaneous detachment and ejection from the substrate [35]. This phenomenon occurs due to the release of excess surface energy during the coalescence process, which is converted into kinetic energy that propels the merged droplet away from the surface. The process begins when two droplets come into close proximity, forming a liquid bridge at their interface. The curvature difference between the coalescing droplets drives capillary flows within the liquid bridge, rapidly equalizing the pressure distribution. This redistribution of liquid causes a sudden contraction in the contact area, generating a recoil force. The surface energy released during this contraction significantly exceeds the energy losses from viscous dissipation, resulting in a pronounced upward motion of the merged droplet. On superhydrophobic surfaces, the minimal adhesion between the droplet and the substrate ensures that the majority of the energy released during coalescence is directed toward achieving out-of-surface jumping. The outcome is a spherical droplet that detaches cleanly from the surface with substantial velocity.

1.5. Dissertation Overview.

In this dissertation, we investigate the intricate dynamics of droplet-substrate interactions, encompassing processes from evaporation to out-of-surface jumping. Through systematic experimental, theoretical, and computational studies, we unravel the interplay of thermal, capillary, and inertial forces that govern these phenomena, offering novel insights with implications for heat transfer, droplet manipulation, and surface engineering.

In Chapter 2 we explored the evaporation dynamics of sessile water droplets placed on micro-pillared silicon substrates, with substrate temperatures ranging from 20 - 120 °C. A comprehensive thermal circuit model is developed to capture the effects of substrate roughness and temperature on evaporation rates. The study systematically distinguishes two primary components of heat and mass transfer: the droplet cap surface and the interstitial liquid-vapor interface at the droplet base. The experimental and theoretical results highlight distinct evaporation behaviors during the constant contact radius and constant contact angle modes, revealing the dominant factors driving the decreasing evaporation rate. Additionally, the role of internal fluid flow is considered for high-temperature substrates (>100 °C), and an effective thermal conductivity is adopted to account for convection effects. The findings elucidate temperature gradients between the droplet base and the substrate, providing insights into delayed or suppressed boiling phenomena on heated rough surfaces.

In Chapter 3 we investigated the modulation of Leidenfrost-like jumping of sessile water microdroplets on micropillared surfaces at a significantly reduced substrate temperature of 130 °C. The fin-array-like micropillars enable vapor bubble generation at the droplet base, triggering droplet levitation and jumping within milliseconds. By tailoring pillar height to regulate the thermal boundary layer thickness, the droplet jumping behavior is modulated between inertia-controlled and heat-transfer-limited modes, characterized by constant velocity and constant energy regimes, respectively. This strategy facilitates the controlled removal of wetting liquid droplets on rough or structured surfaces, with potential applications in rapid fouling media removal and thermal management.

In Chapter 4 we demonstrated the feasibility of breaking the theoretical capillary length limitation for passive droplet jumping through the burst of an embedded bubble. The upward jet generated by bubble bursting, coupled with the downward propagation of capillary waves along the droplet surface, facilitates efficient momentum transfer to lift centimeter-scale water puddles from superhydrophobic surfaces. The linear dependence of capillary wave momentum on bubble size leads to a quadratic increase in droplet jumping height, providing new insights into fluid-solid interactions and broadening the size spectrum of droplet dynamics studies. This work deepens our understanding of the synergistic roles of bubble bursting and capillary waves in overcoming size constraints for droplet manipulation.

In Chapter 5 we summarized the key contributions of this dissertation, highlighting advancements in understanding droplet evaporation, low-temperature Leidenfrost-like behaviors, and bubble burst-induced jumping. Potential future directions for leveraging these findings in thermal management, anti-icing, and condensation applications are discussed.

Chapter 2

Droplet Evaporation on Hot Micro-Structured Superhydrophobic Surfaces: Analysis of Evaporation from Droplet Cap and Base Surfaces

Disclosure:

This chapter was adapted from a publication in the *International Journal of Heat and Mass Transfer*: Wenge Huang, Xukun He, Cong Liu, Xiaojie Li, Yahua Liu, C. Patrick Collier, Bernadeta R. Srijanto, Jiansheng Liu, Jiangtao Cheng. “Droplet Evaporation on Hot Micro-Structured Superhydrophobic Surfaces: Analysis of Evaporation from Droplet Cap and Base Surfaces” *International Journal of Heat and Mass Transfer* 185 (2022) 122314.

2.1. Introduction

Evaporation of sessile liquid droplets is a ubiquitous phenomenon in nature, which plays an important role in a variety of applications, including inkjet printing [36], DNA mapping [37], spray cooling [38], analyte enrichment/detection [39], and colloidal assembly [5]. Yet, sessile droplet evaporation is a complex process controlled by several interdependent factors, such as droplet contact angle dynamics [40], contact line motion [41, 42], substrate structures and temperature [43, 44], and the surrounding environment [45, 46].

Since the seminal work of Picknett and Bexon in 1977 [47], sessile droplet evaporation on smooth surfaces has been systematically studied, in which droplet evaporation was distinguished into three evaporation modes: (1) constant contact radius (CCR) mode: the droplet contact line is pinned with a constant contact radius while the contact angle keeps decreasing; (2) constant contact angle (CCA) mode: once the contact angle approaches the receding contact angle, the contact line keeps receding with the contact angle unchanged; (3) mixed mode: both the contact radius and contact angle decrease near the end of evaporation. In several recent studies about the droplet evaporation on structured superhydrophobic surfaces, a special stick-slip mode [48] was observed, in which droplet contact line is moved by the pinning and depinning forces alternately.

Several theoretical models have been proposed to predict the evaporation rate of sessile droplets on various surfaces. In the classical work of Picknett and Bexon [47], the sessile droplet evaporation at room temperature was firstly assumed to be driven by vapor diffusion, ignoring the heat transfer and convective flow inside/outside the droplet. And the analytic evaporation rate could be obtained based on an analogy between the concentration field and the electrostatic field [49]. During the past two decades, this diffusion-driven model was extensively studied, which has been applied in modeling the evaporation of sessile droplets with an arbitrary contact angle in the CCR mode or with a slipping contact line in the CCA mode. The excellent agreement between the analytical evaporation rate and the experimental data confirms the validity of the diffusion-driven model of sessile droplet evaporation not only on hydrophilic surfaces [50-52] but also on hydrophobic surfaces [53, 54].

However, when the diffusion-driven model was employed for analyzing sessile droplet evaporation on non-wetting surfaces with microstructures [55], especially on the heated superhydrophobic surfaces, an overestimation of evaporation rate was observed by Garimalla [56, 57]and Aldhaleai [58]. This deviation from the analytically predicted evaporation rate should result from evaporative cooling, giving rise to a temperature reduction on the liquid-vapor interface, which is in contradiction to the pivotal assumption made in the classical diffusion-driven model that the temperature of the droplet surface is constant and same as the substrate temperature [50-52]. For instance, the maximum temperature mismatch of ~20 °C between the droplet surface and the substrate was experimentally observed when the substrate was heated at 70 °C [59]. Furthermore, the applicability of the diffusion-driven model might become worse when the wetting states of droplet on micro-structured surfaces, *i.e.*, the Cassie state or the Wenzel state [22], are considered. For the evaporation of a sessile droplet in the Cassie state, the existence of the air/vapor cushion layer between the droplet base and the microstructures would lead to two different components of droplet evaporation, *i.e.*, one from the liquid-vapor interface at the droplet cap and the other from the droplet base. However, the effect of this extra evaporative interface from the droplet base on superhydrophobic surfaces was generally ignored in the majority of previous work [56, 57, 60]. Indeed, in recent work of Wang [61, 62] and Kim [63], the non-negligible evaporation flux through the vapor-liquid interface over the substrate cavities has been experimentally confirmed on heated superhydrophobic surfaces, whereas these works mainly focused on the wetting or dynamics of the evaporating droplet. Therefore, a systematic study about droplet evaporation on heated micro-structured surfaces by considering the comprehensive effects of the discontinuous liquid-vapor interfaces at the droplet base and the continuous liquid-vapor interface at the droplet cap is entailed.

In this paper, the evaporation of water droplets on hot micro-structured superhydrophobic substrates is experimentally and theoretically investigated. First, a water microdroplet was placed on the superhydrophobic substrates heated at 40 °C - 80 °C. The droplet evaporated in the Cassie state during most of its evaporation time and transited to the Wenzel state at the very end of evaporation. Based on a comprehensive thermal resistance analysis, a thermal circuit model was developed to predict the droplet cap surface temperature and to calculate the evaporation rates from the droplet cap surface and the base surface, respectively. Then, the substrate was further heated from 80 - 120 °C until a further small increase of the substrate temperature would otherwise lead to the boiling of the droplet. As such, an effective thermal conductivity was adopted as a correction factor to account for the effect of convection heat transfer inside the water droplet. The average temperatures of the droplet base surface were calculated and then the temperature differences between the droplet base and the substrate base were obtained, manifesting the depressed or delayed boiling of droplets on the superheated substrates. This study could deepen our understanding of droplet evaporation on hot micro-structured surfaces and provide us a potential way to control the sessile droplet evaporation on non-wetting surfaces.

2.2. Experimental Methodology

2.2.1. Substrates with micropillars

Micropillared silicon devices were manufactured by standard contact photolithography process and deep reactive ion etching method [39]. Three kinds of substrates of 1 mm thick and textured with cylindrical micropillar arrays with varying micropillar periodicity (*P*) were fabricated in this study. The geometry information of the substrates is listed in Table 1 and the scanning electron microscope (SEM) image of one sample substrate is shown in Fig. 1 (a). All the substrates were conformally coated with silane (Trichloro (1H,1H,2H,2H-per fluorooctyl)-silane, Sigma-Aldrich) using standard chemical vapor deposition (CVD) process for superhydrophobicity enhancement [64]. Then the substrates were baked on a hot plate at 100 °C for 60 min. Water droplet exhibits a contact angle of 155° ± 2° on thus-prepared substrates. To mitigate the sample edge effect on the droplet evaporation process, substrate samples were cut into square pieces with the dimension of 2 cm × 2 cm and water droplets were deposited at the center of each piece for evaporation study.

Table 1. Micropillar diameter, periodicity and height on the sample substrates

Substrate	Micropillar diameter D (μm)	Micropillar periodicity P (μm)	Micropillar height H (μm)
Device 1	20	40	40
Device 2	20	50	40
Device 3	20	60	40

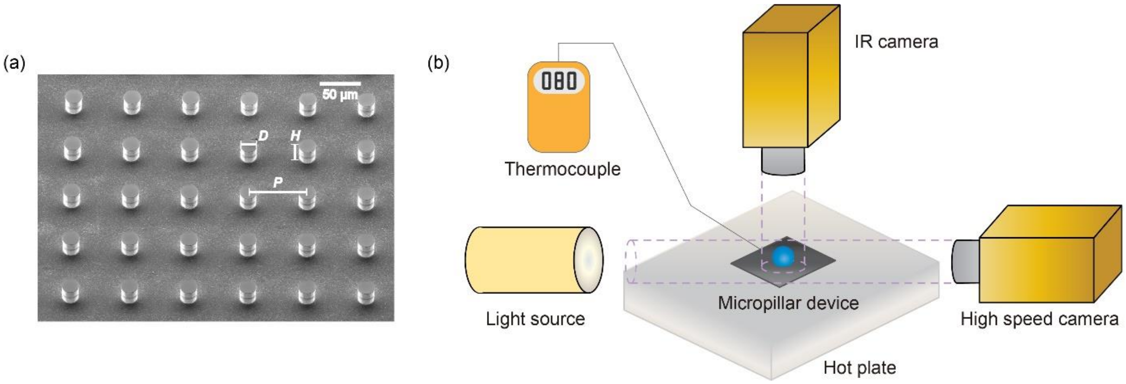

Figure 2-1. Experimental setup. (a) Scanning electron micrograph of the sample device with regularly patterned micropillars for droplet evaporation study. (b) Schematic diagram of the experimental setup including IR camera, device decorated with micropillars on the substrate, hot plate, thermocouple, light source and a high-speed CCD camera mated to an optical tensiometer.

2.2.2. Experimental setup

The schematic of the experimental setup is shown in Fig. 1(b). In this study, deionized (DI) water (Type 1, >18 MΩ cm resistivity) was used as the liquid. A DI water droplet of 4 ± 0.1 μL was generated by a syringe pump (EW-74905, Cole-Parmer Corporation) through a FISNAR dispense tip with 0.15 mm internal diameter and 0.30 mm external diameter. Then the water droplet was gently dispensed on the center of the micro-structured substrate for evaporation study. At least five trials were carried out for each droplet evaporation experiment to ensure the repeatability of the evaporation measurements. Because of the small volume, the shape of the sessile water droplet resembled a spherical cap. The substrate was intimately affixed on a hot plate by double-side copper tape and a K-type thermocouple with ± 0.5 °C uncertainty was used to measure the surface temperature of the substrate during the experiment. The base temperature of the substrate was maintained at a constant level on the hot plate ranging from 40 - 120 °C, beyond which even a small temperature increase would otherwise lead to the onset of boiling of the sessile droplet. Two cameras parallel and normal to the substrate were used to record the evaporation process of the droplets. An infrared (IR) camera (FLIR A655sc) was fixed above the droplet and normal to the substrate to measure the surface temperature evolution of the droplet cap (Calibration process of the IR camera is given in the supplementary materials). A water droplet sitting on the superhydrophobic substrate exhibits a large contact angle and only the upper hemispherical surface of the droplet can be focused by the IR camera. Regardless of the influence of droplet internal flow on its surface temperature distribution, the temperature measured by the IR camera was taken as the average surface temperature of the upper hemispherical cap of the droplet. Aligned in parallel to the substrate, a high-speed CCD camera mated with an optical tensiometer (Theta Lite, OneAttension Corporation) was used to capture the images of the evaporating droplet. The droplet shape was assumed to be axisymmetric. Based on the captured snapshots, the water droplet was vertically divided into multiple layers and the local height and diameter of each water layer were obtained by image processing. Then, the droplet volume was calculated by integrating the volume of each discrete layer. With the snapshots obtained by the high-speed camera, the transient droplet volume, contact angle, contact radius and droplet height were collected for subsequent analysis. During the experiment, the ambient temperature and relative humidity were maintained at $T_{\mathrm{lab}} = 23 \pm 2$°C and $R_{\mathrm{h}} = 35\ \pm 5\%$, respectively.

2.3. Analytical Methodology

2.3.1. Wetting state

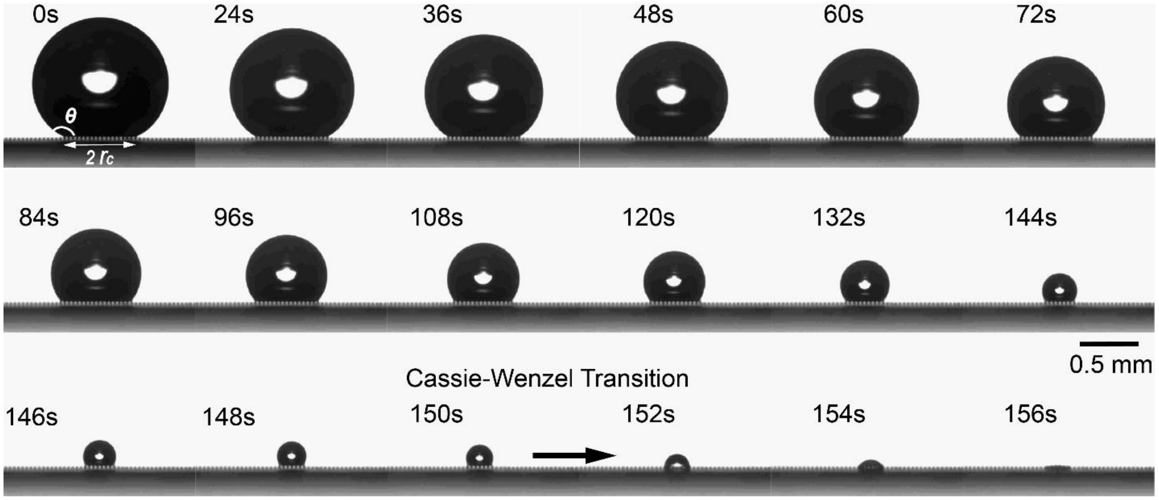

Figure 2-2. Snapshots of the evaporation process of a 4 μL water droplet on sample 1 at 80 °C. The void interstitial cavities under the droplet base during 0 – 150 s indicate that the droplet was in the Cassie state. Cassie to Wenzel transition occurred between 150 s and 152 s as evidenced by the disappearance of void cavities after 152 s.

Water droplets can exhibit different wetting states on the micro-structured substrate during the evaporation. Specific air/vapor cavities underneath the droplet were observed during the majority period of the evaporation, indicating that the droplet was at least partially in the Cassie state. At the very end of the evaporation, water was observed to completely fill the surface cavities underneath the droplet and the droplet was in the Wenzel state during this period. The snapshots of the water droplet during evaporation are shown in Figure 2. Though the droplet exhibited two distinct wetting states during evaporation, the droplet stayed in the Cassie state during most of the evaporation process. In this work, we focus on the evaporation process of the droplet in the Cassie state and the thermal circuit model developed by us is based on the Cassie droplet.

2.3.2. Energy balance model

When a droplet is deposited on the hot device surface, heat transfers from the hot substrate through the micropillars into the sessile droplet due to the temperature difference between them as shown in Fig. 3(a). This heat transfer process results in the temperature increase inside the droplet and accelerate the heat and mass transfer between the droplet and the ambient air. The energy balance of the evaporating sessile droplet is given by:

$$q_{\mathrm{s}} = q_{\mathrm{rise}} + q_{\mathrm{conv}} + q_{\mathrm{rad}} + q_{\mathrm{evap}} \tag{2-1}$$

where q_{s} is the overall heat transfer rate from the substrate to the droplet, q_{rise} accounts for the sensible heat required for the temperature increase within the bulk water, q_{conv} is the convective heat transfer rate between the water droplet and the ambient, q_{rad} is the radiation heat transfer rate from the droplet surface to the ambient, and q_{evap} is the evaporation heat transfer rate. So, we have:

$$q_{\mathrm{rise}} = c_{\mathrm{w}}\rho_{\mathrm{w}}V\frac{dT_{\mathrm{bulk}}}{dt} \tag{2-2}$$

$$q_{\mathrm{rad}} = \varepsilon\sigma S\left(T_{\mathrm{cap}}^4 - T_{\infty}^4\right) \tag{2-3}$$

$$q_{\mathrm{conv}} = h_{\mathrm{conv}}S\left(T_{\mathrm{cap}} - T_{\infty}\right) \tag{2-4}$$

$$q_{\mathrm{evap}} = h_{\mathrm{fg}}\rho_{\mathrm{w}}\frac{dV}{dt} \tag{2-5}$$

where c_{w}, ρ_{w}, T_{cap}, T_{bulk}, V and h_{fg} are the specific heat capacity, density, droplet cap surface temperature, droplet bulk temperature, volume and latent heat of the water droplet, respectively; ε is the emissivity of the water droplet surface and σ is the Stefan-Boltzmann constant; S is the liquid-vapor interface area and h_{conv} is the natural convection heat transfer coefficient of the ambient air.

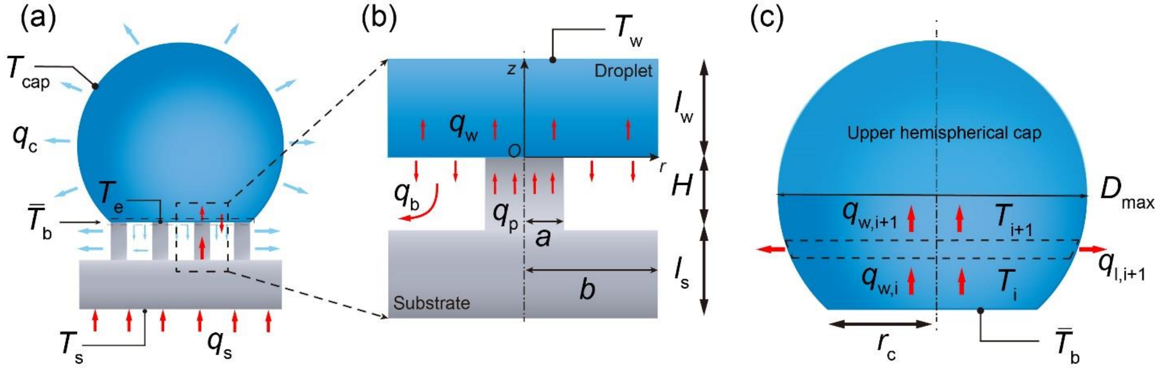

Figure 2-3. Evaporation process (a) Diagram of droplet evaporation on a hot micro-structured superhydrophobic subface. (b) Diagram of heat transfer from a micropillar unit into droplet base surface. (c) Diagram of heat transfer through the sessile water droplet. The upper hemispherical cap is the top portion above the maximum diameter $\boldsymbol{D}_{\mathbf{max}}$ of the droplet cap. The IR camera above a sessile droplet can only detect the temperature distribution on the upper hemispherical surface.

Because of the high efficiency of phase change heat transfer, the evaporation rate q_{evap} is dominant over the other heat transfer modes. Thus, the overall heat transfer from the substrate to the water droplet can be estimated as the heat released from the droplet surface to the ambient by evaporation [65]. Therefore, the energy balance of the sessile droplet can be rewritten as:

$$q_{\mathrm{s}} \approx q_{\mathrm{evap}} \tag{2-6}$$

2.3.3. Average temperature of droplet base surface

In section 3.2, by analyzing the energy balance of a water droplet during evaporation, we found that the heat transfer rate from the substrate q_{s} can be estimated by the evaporative heat transfer rate q_{evap}. Because of the periodicity of the micropillar array, the heat transfer process in one micropillar cell as illustrated in Fig. 3(b) can be representative of the heat transfer process between the droplet base and the substrate micropillars [61, 66]. Thus, we focus on the heat transfer from one micropillar cell into the droplet base and the heat transfer rate in one unit cell is calculated as:

$$q_{\mathrm{p}} = \frac{q_{\mathrm{s}}}{N} = \frac{q_{\mathrm{evap}}}{N} \tag{2-7}$$

where *N* is the total number of the micropillars underneath the droplet, *i.e.*, the ratio of the droplet apparent contact area to one unit cell area.

A unit of the micropillar cell consists of one micropillar and the cavity around it. In general, heat transfer from both the silicon micropillar and the vapor cavity surrounding it should be considered. However, the thermal resistance of the vapor layer is much larger than that of the silicon micropillar due to the order of magnitude difference in the thermal conductivities of silicon micropillars (100 W·m^{-1}·K^{-1})[61] and water vapor (0.025 W·m^{-1}·K^{-1}) [62]. Therefore, it is reasonable to assume that heat primarily conducts from the micropillar to the water droplet while the vapor-solid interface of the cavity can be regarded as adiabatic. The thermal resistance per unit cell of the silicon substrate can be calculated as:

$$R_{\mathrm{s}} = \frac{l_{\mathrm{s}}}{k_{\mathrm{Si}} P^2} + \frac{4H}{k_{\mathrm{Si}} \pi D^2} \tag{2-8}$$

where k_{Si} is the thermal conductivity of silicon and l_{s} is the thickness of the silicon substrate excluding the micropillar height.

The effects of droplet internal flow are not significant for droplet evaporation on a relatively low temperature substrate, *i.e.*, < 80 °C. The characteristic fluid velocity in a 3 μL water droplet evaporating on a 60 °C substrate is about tens microns per second and the Peclet number is less than 1 [56]. Thus, it is reasonable to consider just the conduction heat transfer while neglecting the internal convection of the water droplet on a substrate with a relatively low temperature. The time scale for heat conduction in the droplet is on the order of $\frac{r_{\mathrm{w}}^2 \rho_{\mathrm{w}} c_{\mathrm{w}}}{k_{\mathrm{w}}} \sim 0.01\mathrm{s}$, where r_{w} is the radius of the droplet. The total evaporation time of the droplet on the substrate is on the order of 100 s. The ratio of the time scale for heat conduction to that of evaporation is about 0.0001, implying that the conductive heat transfer process may be considered as quasi steady.

To estimate the temperature distribution near the liquid-solid interface, *i.e.*, at the tip of the micropillar in contact with the droplet base, a thin water layer with a thickness of l_{w} in a unit cell (Fig. 3b) is considered. The conductive heat transfer equation for the water layer therein is:

$$\frac{\partial^2 T}{\partial r^2} + \frac{1}{r}\frac{\partial T}{\partial r} + \frac{\partial^2 T}{\partial z^2} = 0 \tag{2-9}$$

where T denotes the temperature of the water film.

Due to the relatively small size of the micropillar, the heat flux across the liquid-solid (tip) interface and the liquid-vapor interface in a unit cell could be assumed to be uniform. As a result, we have the first boundary condition:

$$k_{\mathrm{w}} \frac{\partial T}{\partial z} = \begin{cases} \frac{q_{\mathrm{p}}}{\pi a^2} & 0 < r < a; \quad z = 0 \\ -\frac{q_{\mathrm{b}}}{\pi (b^2 - a^2)} & a < r < b; \quad z = 0 \end{cases} \tag{2-10}$$

where k_w is the thermal conductivity of water, a is the radius of the micropillar, b is the radius of one unit cell [67], q_{b} is the heat transfer rate from the droplet base-vapor interface within one unit cell as shown in Fig. 3(b).

Temperature inside the water layer is assumed to quickly become uniform. Hence, a uniform temperature boundary could be assumed at $z = l_w$:

$$T(r; z) = T_w \qquad 0 < r < b; \quad z = l_w \tag{2-11}$$

Moreover, considering the periodicity of the unit cells, we assume the adiabatic boundary between the chosen unit cell and its neighboring cells inside the water layer. Thus, we obtain the following adiabatic boundary condition:

$$\frac{\partial T}{\partial r} = 0 \qquad r = b; \quad 0 < z < l_w \tag{2-12}$$

Solving the heat transfer equation Eq. (11) with the three boundary conditions Eqs. (10)-(12), we can obtain the temperature distribution inside the water layer as:

$$T_{\mathrm{b}}(\mathrm{r}, \mathrm{z}) = T_{\mathrm{w}} + \frac{q_p(l_{\mathrm{w}} - z)}{\pi k_{\mathrm{w}}}\left(\frac{(1-\varphi)}{b^2}\right) + \frac{2aq_{\mathrm{p}}}{\pi k_{\mathrm{w}}}\left(\frac{1}{a^2} + \frac{\varphi}{b^2 - a^2}\right)\sum_{n=1}^{\infty}\left[J_1\left(\frac{a}{b}\alpha_n\right)J_0\left(\frac{r}{b}\alpha_n\right)/\left(\alpha_n^2 J_0^2(\alpha_n)\right)\right]\frac{\sinh\left(\frac{\alpha_n}{b}(l_{\mathrm{w}} - z)\right)}{\cosh\left(\frac{\alpha_n}{b}l_{\mathrm{w}}\right)} \tag{2-13}$$

where φ is the evaporation ratio, *i.e.*, the heat transfer across the droplet base-vapor interface over the overall heat transfer from the substrate to the droplet $\varphi = q_{\mathrm{b}}/q_{\mathrm{p}}$. Here $J_0(x)$ and $J_1(x)$ are the first kind Bessel functions with orders of 0 and 1, respectively, α_n is the n$^{\mathrm{th}}$ root of $J_1(x) = 0$ [68].

The temperature at the droplet base ($z = 0$) is calculated as:

$$T_{\mathrm{b}}(\mathrm{r}, 0) = T_{\mathrm{w}} + \frac{q_p l_{\mathrm{w}}}{\pi k_{\mathrm{w}}}\left(\frac{(1-\varphi)}{b^2}\right) + \frac{2aq_{\mathrm{p}}}{\pi k_{\mathrm{w}}}\left(\frac{1}{a^2} + \frac{\varphi}{b^2 - a^2}\right)\sum_{n=1}^{\infty}\left[J_1\left(\frac{a}{b}\alpha_n\right)J_0\left(\frac{r}{b}\alpha_n\right)/\left(\alpha_n^2 J_0^2(\alpha_n)\right)\right]\tanh\left(\frac{\alpha_n}{b}l_{\mathrm{w}}\right) \tag{2-14}$$

Thus, the average temperature of the droplet base could be obtained as:

$$\bar{T}_{\mathrm{b}} = \frac{\int_0^b 2\pi r T_{\mathrm{b}}(r)dr}{\pi b^2} \tag{2-15a}$$

$$\bar{T}_{\mathrm{b}} = T_w + \frac{q_p l_{\mathrm{w}}}{\pi k_{\mathrm{w}}}\left(\frac{(1-\varphi)}{b^2}\right) \tag{2-15b}$$

The average temperature of the liquid-solid (tip) interface at the droplet base could be estimated as:

$$T_{\mathrm{b,p}} = \frac{\int_0^a 2\pi r T_{\mathrm{b}}(r)dr}{\pi a^2} \tag{2-16a}$$

$$T_{\mathrm{b,p}} = \bar{T}_{\mathrm{b}} + \left\{\frac{2aq_{\mathrm{p}}}{\pi k_{\mathrm{w}}}\left(\frac{1}{a^2} + \frac{\varphi}{b^2 - a^2}\right)\sum_{n=1}^{\infty}\left[J_1^2\left(\frac{a}{b}\alpha_n\right)/\left(\alpha_n^3 J_0^2(\alpha_n)\right)\right]\tanh\left(\frac{\alpha_n}{b}l_{\mathrm{w}}\right)\right\} \tag{2-16b}$$

Considering the heat conduction in the silicon substrate, the temperature on the tip of the micropillar could be calculated as:

$$T_{\mathrm{p}} = T_{\mathrm{s}} - \frac{q_{\mathrm{p}}}{R_{\mathrm{s}}} \tag{2-17}$$

The temperature at the liquid-solid interface should be same as the contact temperature [69-71], we have:

$$T_{\mathrm{b,p}} = T_{\mathrm{e}} = \frac{\sqrt{\rho_{\mathrm{w}} k_{\mathrm{w}} c_{\mathrm{w}}} T_{\mathrm{o}} + \sqrt{\rho_{\mathrm{Si}} k_{\mathrm{Si}} c_{\mathrm{Si}}} T_{\mathrm{p}}}{\sqrt{\rho_{\mathrm{w}} k_{\mathrm{w}} c_{\mathrm{w}}} + \sqrt{\rho_{\mathrm{Si}} k_{\mathrm{Si}} c_{\mathrm{Si}}}} \tag{2-18}$$

where ρ, c and k are the density, specific heat and thermal conductivity of water (w) and silicon (Si), respectively; T_{o} is the initial temperature of the water droplet.

Thus, the average temperature of the water droplet base is given b

$$\bar{T}_{\mathrm{b}} = T_{\mathrm{e}} - \frac{2aq_p}{\pi k_w}\left(\frac{1}{a^2} + \frac{\varphi}{b^2 - a^2}\right)\sum_{n=1}^{\infty}\left[J_1^2\left(\frac{a}{b}\alpha_n\right)/\left(\alpha_n^3 J_0^2(\alpha_n)\right)\right] \tag{2-19}$$

2.3.4. Evaporation from droplet cap surface

For the sessile droplet evaporating at the relatively low temperature (40 °C – 80 °C), we only considered the conduction heat transfer in the bulk water and the internal convection process was neglected as discussed before. Thus, we employed one-dimensional heat conduction model to describe the heat transfer process inside the droplet as shown in Fig. 3(c). The water droplet was discretized into a series of thin layers (i = 1, … X, where X is the total number of water layers) parallel to the substrate. Here, temperatures at the bottom surface (T_{i}) and the top surface ($T_{\mathrm{i+1}}$) of the ith water layer are assumed to be laterally uniform, respectively. Then, in the ith water layer, we have:

$$T_{\mathrm{i+1}} = T_{\mathrm{i}} - q_{\mathrm{w,i}} \cdot R_{\mathrm{i}} \tag{2-20}$$

where $R_{\mathrm{i}} = \frac{\Delta h}{k_{\mathrm{w}} \pi r_{\mathrm{i}}^2}$ is the thermal resistance of the ith water layer, Δh is the thickness of each water layer, and r_{i} is the radius of the ith water layer.

Taking the ith layer as the control volume, heat transfer into the ith water layer from the bottom surface ($q_{\mathrm{w,i}}$) is balanced by the heat transfer to the top surface ($q_{\mathrm{w,i+1}}$) and the evaporation rate ($q_{\mathrm{l,i}}$) from the side surface. Thus, the energy balance in the ith water layer is:

$$q_{\mathrm{w,i+1}} = q_{\mathrm{w,i}} - q_{\mathrm{l,i}} \tag{2-21}$$

where $q_{\mathrm{l,i}} = J_{\mathrm{i}}(r) \cdot h_{\mathrm{fg}} \cdot \Delta S_{\mathrm{i}}$, ΔS_{i} is the side surface area of the ith water layer, h_{fg} is the latent heat, and $J_{\mathrm{m,i}}(r)$ is the local evaporation mass flux.

Then we applied the diffusion-driven model to estimate the local evaporation flux, which is the solution to the Laplace equation based on Fick's law of vapor diffusion around the droplet. Hence, the exact solution of the local evaporation mass flux is given by [52]:

$$J_{\mathrm{m}}(r)=\frac{D_{\mathrm{d}}\left(c_{\mathrm{s}}(T_{\mathrm{i}})-R_{\mathrm{h}}c_{\mathrm{s}}(T_{\infty})\right)}{r_c}\cdot\left[\frac{1}{2}\sin(\theta)+\sqrt{2}\left(\cosh(\beta)+\cos(\theta)\right)^{3/2}\cdot\right.$$
$$\left.\int_0^{\infty}\frac{\cosh(\theta\tau)}{\cosh(\pi\tau)}\tan[(\pi-\theta)\tau]\cdot P_{-0.5+i\tau}\left(\cosh(\beta)\right)\tau\cdot d\tau\right] \quad (2\text{-}22)$$

where T_{i} is approximated to be the temperature at the side surface, c_{s} is the saturated vapor concentration, D_{d} is the diffusion coefficient of vapor, and R_{h} is the relative humidity. And β is the toroidal coordinate related uniquely to the cylindrical coordinate *r* on the cap surface.

The evaporation heat transfer rate from the droplet cap surface is calculated by integrating all the local evaporation rates:

$$q_{\mathrm{c}}=\sum_{i=1}^{X}q_{\mathrm{l,i}} \quad (2\text{-}23)$$

The evaporation heat transfer from the droplet cap should be the same as the heat transferred through the water droplet:

$$q_{\mathrm{c}}=(1-\varphi)q_s \quad (2\text{-}24)$$

As mentioned above, the temperature measured by the IR camera can be taken as the average temperature of the upper hemispherical surface as illustrated in Fig. 3(c). With the average droplet base temperature obtained, we can calculate the surface temperature distribution based on the heat transfer equation Eq. (20) for each of the discretized water layers. Thus, we can approximate the average temperature of the upper hemispherical surface of the droplet as:

$$T_{\mathrm{model}}=\sum_{i=1}^{M}T_{\mathrm{i}}\cdot\Delta S_{\mathrm{i}}/2\pi r_w^2 \quad (2\text{-}25)$$

where *M* is the number of discrete water layer in the upper hemisphere of the droplet spherical cap, r_{w} is the radius of the spherical cap.

2.3.5. Algorithm for calculating the surface temperature and evaporation ratio

The algorithm for calculating the droplet surface temperature and the evaporation ratio φ is shown in the flowchart of Fig. 4. The base temperature of the substrate T_s is measured by the thermocouple and the heat transfer rate from the substrate q_s is obtained by calculating the droplet volume decreasing rate based on Eq. (5). An initial estimate of the evaporation ratio $\varphi=0.5$ is used in the boundary condition to solve the heat transfer equation Eq. (9) at the droplet base. Then the temperature distribution at the droplet base is calculated by Eq. (14) and consequently the average temperature of the droplet base $\bar{T}_b$

is obtained. The nonuniform surface temperature distribution of the droplet cap is calculated based on the one-dimensional heat conduction model inside the droplet and the evaporation rate q_{c} from the droplet cap is then obtained. The evaporation heat transfer from the droplet cap should be the same as the heat transfer through the droplet body from the droplet base and the value of φ' is then obtained by Eq. (24) as the new evaporation ratio in the next iteration of calculation. After the iteration loop achieves convergence, both the stable evaporation ratio φ and the temperature distribution on the droplet cap surface are obtained. With the temperature distribution on the droplet cap obtained, the average temperature of the upper hemispherical surface of the droplet cap surface T_{model} is calculated and compared with the experimental results for the validation of our thermal circuit model.

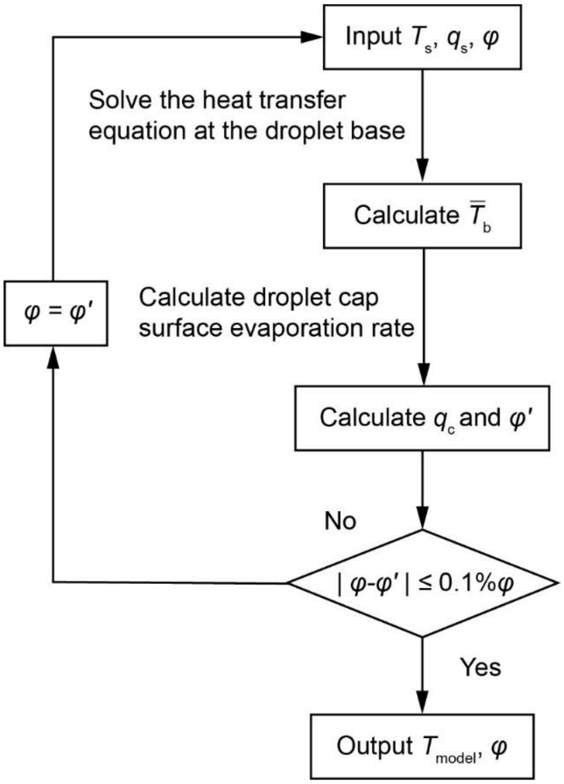

Figure 2-4. Flowchart for calculating the droplet surface temperature and evaporation ratio $\boldsymbol{\varphi}$, which is defined as the ratio of evaporation rate from the droplet base surface to the total heat transfer rate through a droplet.

It is not practical to directly measure or calculate the evaporation rate from the droplet base because of the complex micro-pillared structures on the devices. Thus, the evaporation rate from the droplet base is taken as the difference of the total evaporation rate of the droplet and the evaporation rate from the droplet cap. The evaporation rate from the droplet cap is thus estimated by the diffusion-driven model with the droplet surface temperature distribution taken into consideration (Eqs. 22 and 23). This evaporation rate estimation method can be validated by Gleason and Putnam's work [72], in which they reported the droplet evaporation rate by the diffusion-driven model with the droplet surface temperature distribution taken into account and the evaporation rate estimation errors of this method were 1.84% and 2.83% for droplet evaporation on a substrate at 50 °C and 65 °C, respectively.

2.4. Results and Discussion

2.4.1. Droplet evaporation dynamics

The temporal evolutions of the droplet volume on the three devices heated at different temperatures are shown in Fig. 5. In general, droplet volume decreases nonlinearly during the evaporation. The total evaporation time decreases with the rise of the substrate temperature. At the same substrate temperature, the total evaporation time increases with the increasing micropillar periodicity. It can be seen in Fig. 5 that at each substrate temperature, droplet evaporation has the longest total evaporation time on device 3 (60 μm periodicity) and has the shortest total evaporation time on device 1 (40 μm periodicity). The observed increasing trend of total evaporation time can be ascribed to the enhanced thermal resistance between the droplet base and the substrate, which is caused by the increase of the micropillar periodicity with more cavities. The total evaporation time of a 4 μL water droplet on the three devices with varying base temperatures is shown in Table 2.

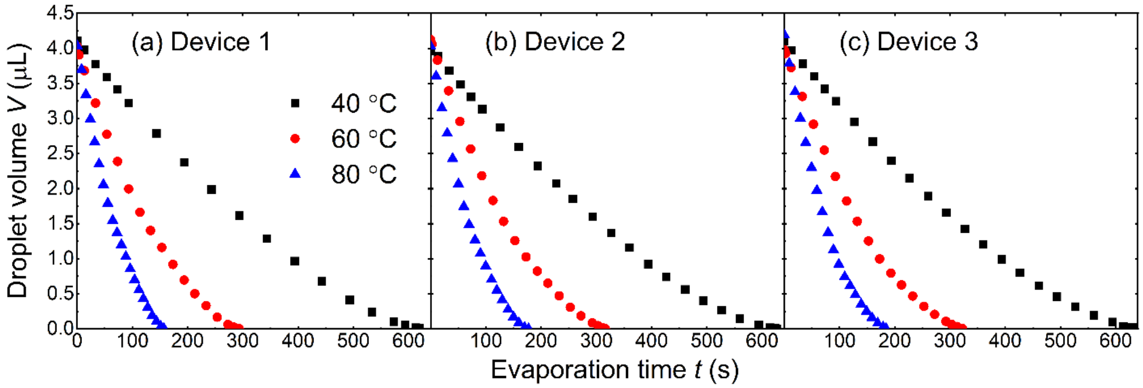

Figure 2-5. Experimentally observed temporal evolution of water droplet volume on (a) device 1, (b) device 2, and (c) device 3. The substrate of each device was heated to 40 °C, 60 °C and 80 °C, respectively. The initial droplet volume was 4 μL.

Table 2. Total evaporation time for water droplet of 4 μL on micro-pillared substrates with different base temperatures.

Substrate	Substrate base temperature (°C)	Total evaporation time (s)
Device 1	40	620.1 ± 13.7
	60	293.3 ± 9.6
	80	156.8 ± 10.6
Device 2	40	627.1 ± 7.6
	60	312.2 ± 6.5
	80	177.1 ± 10.6
Device 3	40	633.3 ± 10.2
	60	322.3 ± 7.7
	80	184.1 ± 12.9

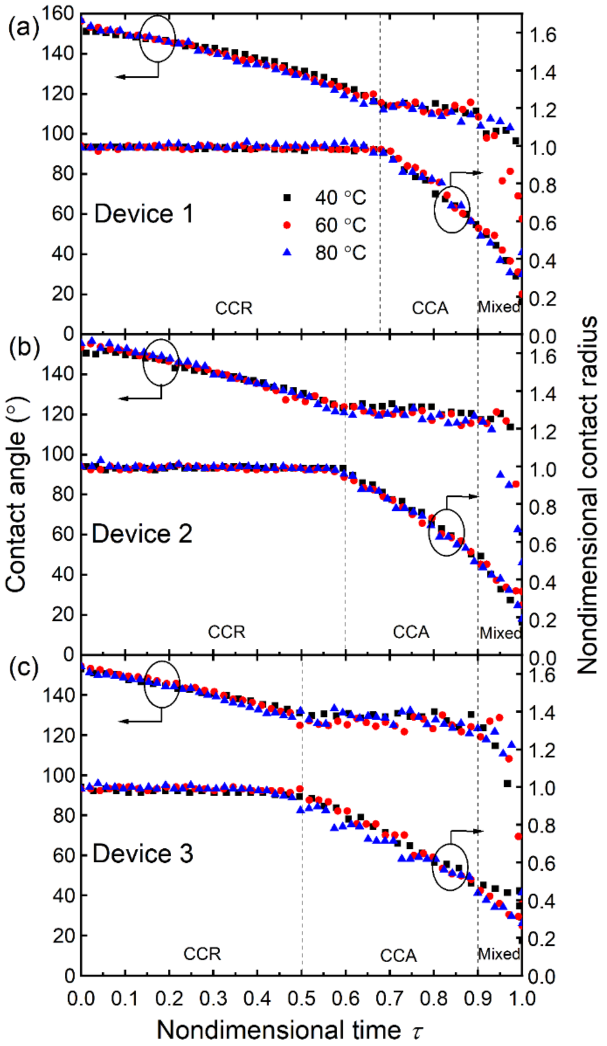

Figure 2-6. Experimental evolution of droplet contact angle and nondimensional contact radius versus nondimensional time on (a) device 1, (b) device 2 and (c) device 3. Each substrate base was heated to 40 °C, 60 °C and 80 °C, respectively.

The evolutions of droplet contact angle and nondimensional contact radius with nondimensional evaporation time are shown in Fig. 6. Here the nondimensional contact radius is defined as the ratio of the contact radius to the initial contact radius, and the nondimensional time is defined as the ratio of the evaporation time to the total evaporation time. It can be seen from Fig. 6 that the evolutions of droplet contact angle and nondimensional contact radius are almost the same for droplet evaporation on each device with different substrate temperatures. For droplet evaporation on device 1 (Fig. 6a), the droplet contact angle continuously decreased during the first 68% portion of the total evaporation time while the contact radius remained unchanged, which was in the constant contact radius (CCR) mode during droplet evaporation. After the contact angle reached the receding contact angle, the contact angle stopped decreasing and was maintained at a constant level while the contact radius started to decrease, which was in the constant contact angle (CCA) mode of droplet evaporation. The droplet evaporation was kept in the CCA mode till the nondimensional time approached 0.9. Then, both the contact angle and contact radius started decreasing, which was the mixed mode for droplet evaporation. For droplet evaporation on the same device with different substrate temperatures, the evaporation process had almost the same compositions of the CCR, CCA and mixed modes, indicating that the substrate structure is more influential on the evaporation mode transition than the substrate temperature at least within a certain range (*i.e.*, ≤ 80 °C). The evolutions of droplet contact angle and nondimensional contact radius on device 2 (Fig. 6b) and device 3 (Fig. 6c) are similar to that on device 1. It is noteworthy that the receding contact angle increases with the increasing periodicity of micropillars on the substrates. The receding contact angles on device 1, device 2 and device 3 are about 112°, 120° and 128°, respectively. Since the initial contact angles of water droplets on these three devices are almost the same (about 155°), a larger receding contact angle results in the shorter term of the CCR mode. The nondimensional evaporation times for the CCR mode on device 1, device 2 and device 3 are about 0.68, 0.6 and 0.5, respectively.

2.4.2. Experimental and modelled droplet cap surface temperature

In this work, IR camera was used to monitor the droplet cap temperature evolution with droplet evaporation. The snapshots of IR thermography for water droplet evaporation on device 2 heated at 40 °C, 60 °C and 120 °C, respectively, are shown in Fig. 7. Distinct surface temperature gradient exhibits in these IR images. The average temperature of the droplet cap surface is extracted from these IR images for comparison with that predicted by the thermal circuit model and the effects of the droplet surface curvature are discussed in the supplementary materials.

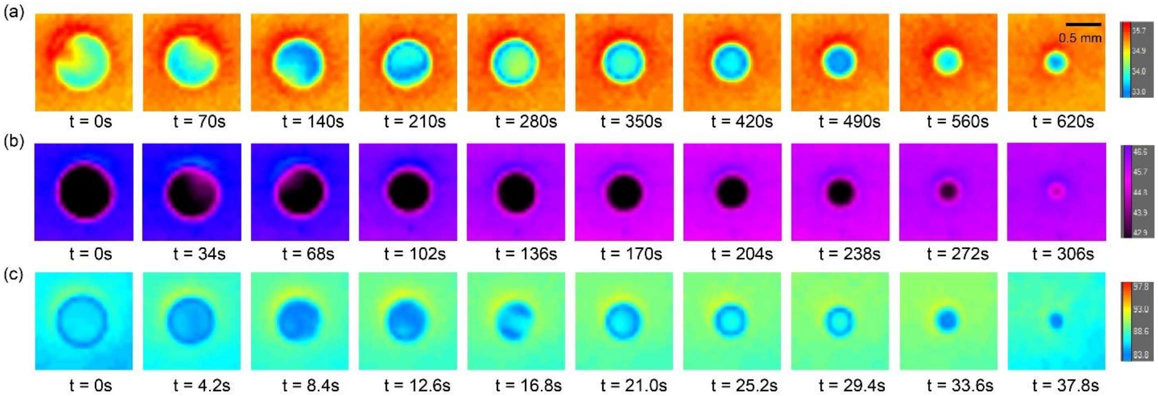

Figure 2-7. Snapshots of IR thermography of droplet evaporation on device 2 heated at (a) 40 °C, (b) 60 °C and (c) 120 °C, respectively.

The evolutions of droplet cap temperature versus the nondimensional time on devices 1, 2 and 3 are shown in Figs. 8(a), (b) and (c), respectively. For droplet evaporation on substrates with temperature in the range of 22 °C – 80 °C, the droplet cap temperature predicted by the thermal circuit model matches well with that measured by the IR camera. There exists a large temperature gradient between the droplet cap surface and the substrate base, which is caused by the thermal resistances of the droplet body, the evaporation at the droplet surface and the conduction through the silicon substrate. It can be seen in Fig. 8 that the average droplet cap temperature increased in the CCR mode and kept almost constant in the CCA mode. Similar trends were also observed by Saenz et al. in their numerical simulation of droplet evaporation on heated surfaces [73]. During the CCR mode, the thermal resistance of the droplet body decreases with the decreasing droplet volume. Meanwhile, the continuously shrinking droplet cap gets closer to the substrate and thus the droplet cap temperature increases. During the CCA mode, the contact area between the droplet base and the substrate continuously decreases. As a result, less heat is transferred into the droplet, hindering the temperature increase of the droplet. During the CCA mode, the shrinking contact area between the droplet base and the substrate results in the almost unchanged temperature on the droplet cap. In the mixed mode, the volume of the evaporating droplet is relatively small (< 0.05 μL) and droplet evaporation in this mode is not a focus of this discussion.

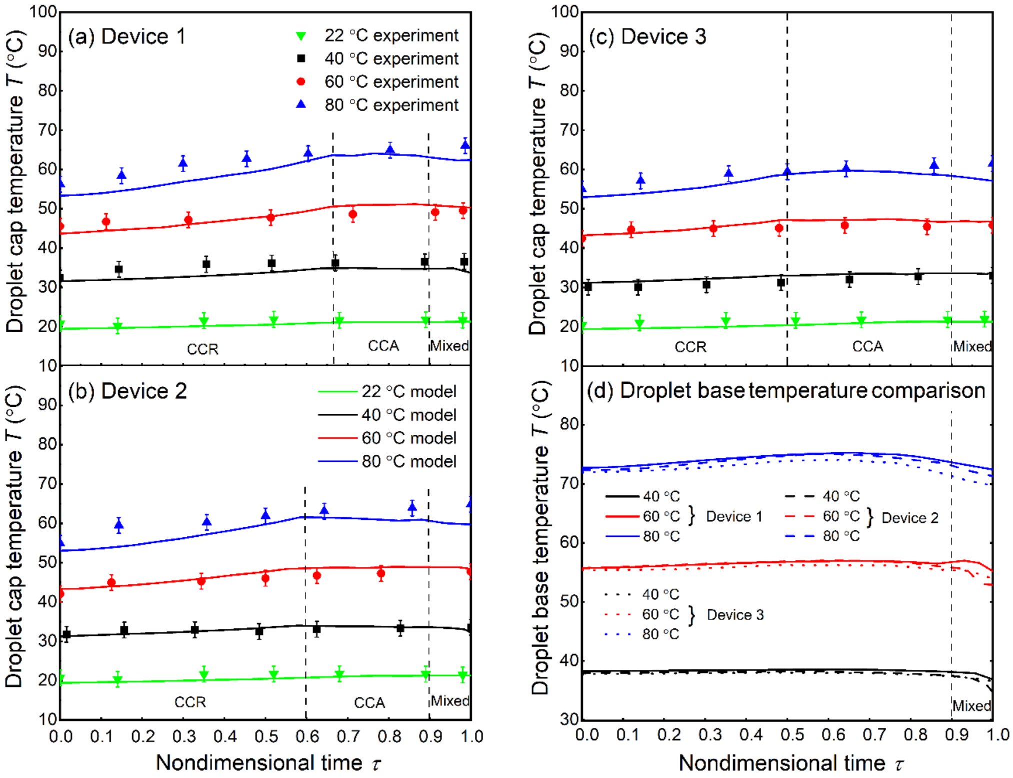

Figure 2-8. Evolutions of droplet cap surface temperature on (a) device 1, (b) device 2, and (c) device 3. The solid lines represent the droplet cap surface temperature calculated by the thermal circuit model and the scatter dots are the experimental results obtained by the IR camera. (d) Evolutions of droplet base temperature on device 1, device 2 and device 3 with the substrate temperature at room temperature and heated at 40 °C, 60 °C and 80 °C, respectively.

The average temperature of the droplet base on each device with different substrate temperatures is shown in Fig. 8(d). There exists an apparent temperature mismatch between the droplet base and the substrate base. Though there is a temperature drop through the substrate because of the substrate's conduction resistance, the large thermal conductivity of silicon (300 W/m·K) should have led to a very small thermal resistance. As such, the temperature drop through the substrate is estimated to be < 1°C. However, the temperature mismatches between the droplet base and the substrate base are about 2 °C, 5 °C and 8 °C with the substrate base temperature maintained at 40 °C, 60 °C and 80 °C, respectively. It is plausible that such an apparent temperature difference between the droplet base and the substrate base may be mainly caused by the local evaporation from the droplet base within the micropillar cavities.

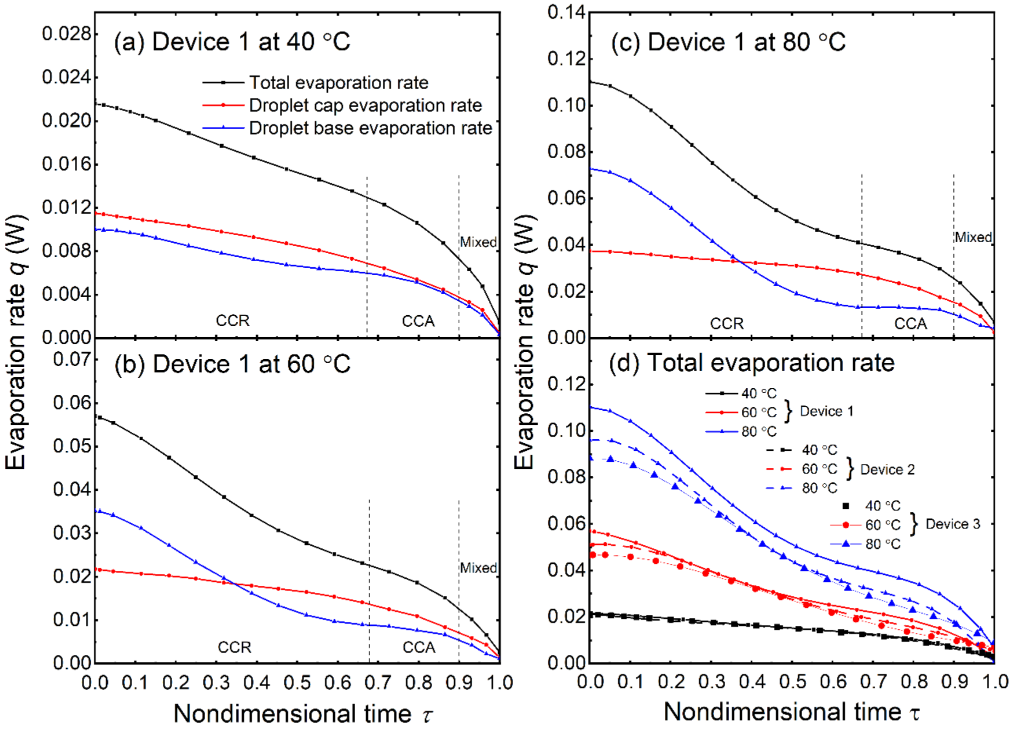

Figure 2-9. Total evaporation rate, evaporation rate from droplet cap surface and evaporation rate from droplet base on device 1 with (a) 40 °C substrate base temperature, (b) 60 °C substrate base temperature and (c) 80 °C substrate base temperature. (d) Total evaporation rate on devices 1, 2 and 3 with substrate base temperature maintained at 40 °C, 60 °C and 80 °C, respectively.

In Figs. 9(a), (b) and (c), we show the transient evolutions of the total evaporation rate, the evaporation rate from droplet cap and the evaporation rate from droplet base on device 1 with the substrate base temperature maintained at 40 °C, 60 °C and 80 °C, respectively. The corresponding evaporation rates of water droplets on device 2 and device 3 are given in the supplementary materials. The total evaporation rate of water droplet is calculated by Eq. (5) and (6), *i.e.*, the droplet volume decreasing rate. The evaporation rate from the droplet cap surface is calculated by the diffusion-driven model with the cap surface temperature distribution predicted by the thermal circuit model. The evaporation rate from the droplet base is the difference between the total evaporation rate and the evaporation rate from droplet cap. Obviously, the increase of the substrate temperature would lead to the evaporation enhancement from both the droplet cap surface and the droplet base surface. Also, both the evaporation rates from the droplet cap and from the droplet base decrease during droplet evaporation on a substrate with a constant temperature. It can be seen that in the CCR mode the slope of the evaporation rate from the droplet cap is smaller than that at the droplet base, indicating a lower decreasing speed of the evaporation rate from the droplet cap. In the CCR mode, the reduction of the droplet contact angle results in the decrease of the evaporation rate from droplet cap surface. Meanwhile, the increase of temperature on the droplet cap surface will enhance the evaporation rate thereon. The effect of droplet cap temperature increase compensates the depressed effect of the droplet contact angle decrease on the evaporation from the droplet cap. The combined effects of the contact angle decrease and the droplet cap temperature increase give rise to the slow decrease of the evaporation rate from the droplet cap in the CCR mode. In the CCA mode, the average temperature of the droplet cap keeps essentially constant, which is in contrary to the increasing trend of the droplet cap temperature in the CCR mode. Meanwhile, the contact radius of the droplet decreases in the CCA mode, which causes the decreasing heat transfer area between the droplet and the substrate. Thus, the evaporation rate from the droplet cap decreases quickly in the CCA mode. In summary, in the CCR mode the decrease of the total evaporation rate of the droplet is mainly caused by the decreasing evaporation rate from the droplet base. Whereas in the CCA mode, the decrease of the total evaporation rate is mainly induced by the decreasing evaporation rate from the droplet cap.

Droplet evaporation on different substates exhibits distinct evaporation rates as shown in Fig. 9(d). Droplet on device 1 (40 μm periodicity) has the maximum evaporation rate while droplet has the minimum evaporation rate on device 3 (60 μm periodicity). Due to the different periodicities of micropillars, the droplet-micropillar contact areas are different on these devices. Since water droplets on these device substrates have almost the same apparent contact area (*i.e.*, base area of the droplet), small periodicity of micropillars means larger heat transfer area between the droplet base and the substrate, *i.e.*, the solid-liquid interface area. The larger solid-liquid interface area results in the higher droplet evaporation rate at the same substrate base temperature.

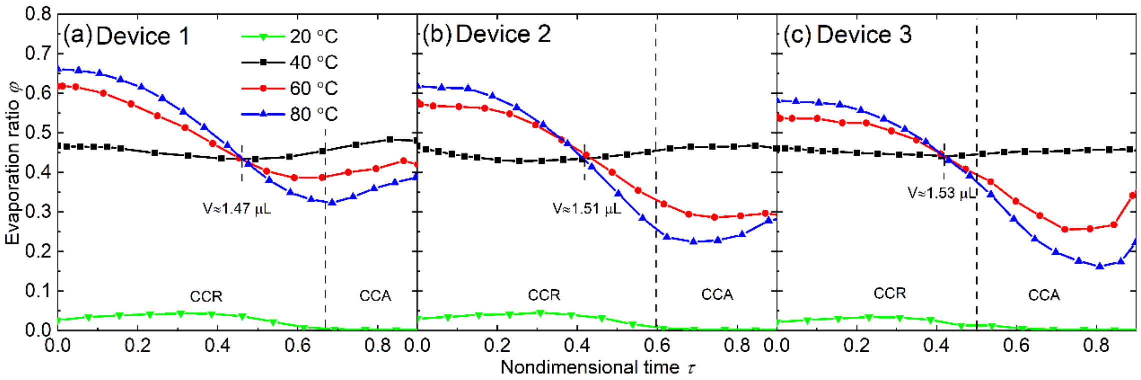

Figure 2-10. Evaporation ratio φ of water droplets with respect to nondimensional time τ on each micro-structured device with different substrate base temperatures.

Evaporation ratio φ is defined as the ratio of the evaporation rate from the droplet base to the total evaporation rate. The evaporation ratio φ with respect to nondimensional time τ on different devices with different substrate base temperatures is shown in Fig. 10. It can be seen that the evaporation ratio φ generally decreases in the CCR mode while increasing close to the end of the CCA mode. This phenomenon is mainly caused by the larger decreasing rate of evaporation from the droplet base in the CCR mode and the relatively smaller decreasing rate of evaporation in the CCA mode, compared with the evaporation rate from the droplet cap. Generally, the evaporation ratio φ increases with the substrate temperature for droplet with a relatively large volume. For droplet evaporation at room temperature, the evaporation ratio φ is almost 0, which means most of the evaporation occurs at the droplet cap surface. The increase of the substrate temperature will directly cause a temperature increase at the droplet base and subsequently induce the temperature increase at the droplet cap. Due to the thermal resistance of the droplet bulk, the temperature increase at the droplet cap is smaller than that at the droplet base in response to the substrate temperature increase. Thus, more evaporation occurs from the droplet base than that from the droplet cap with the increase of the substrate temperature. It can be seen from Fig. 10 that the evaporation ratio φ decreases with the increase of the substrate temperature after the droplet volume shrank to less than ~1.5 μL. This opposite variation of the evaporation ratio is caused by the decreased droplet volume. When the droplet volume shrank to about 1.5 μL, both the droplet height and the droplet cap surface area decreased rapidly, *e.g.*, the surface area of the droplet cap could be reduced by half. As a result, the thermal resistance of the droplet bulk is comparatively small, and the increase of the substrate temperature will cause a higher temperature rise at the droplet cap. Thus, stronger evaporation occurs from the droplet cap than from the droplet base with the increase of the substrate temperature and consequently the evaporation ratio φ decreases.

2.4.3. Effective conductivity of water droplet for evaporation on high temperature substrate

We further conducted droplet evaporation experiments on the same micro-structured surfaces at even higher temperatures. Figs. 11(a), (b) and (c) show the evolutions of droplet cap temperature during droplet evaporation on different devices with the substrate temperature maintained at 100 °C and 120 °C, respectively. The dash lines are the droplet cap temperatures calculated by the thermal circuit model. For droplet evaporation on a substrate with a relatively low temperature (40 °C – 80 °C), the droplet cap temperature calculated by the thermal circuit model matches well with the experimental results. However, for droplet evaporation on a high temperature substrate, there exist large deviations between the model-predicted results and the experimental measurements. These deviations are largely due to the internal fluid flow of the droplet, which becomes stronger at higher temperature and is not considered in the thermal circuit model. The effects of droplet internal flow are not significant for droplet evaporation on relatively low temperature substates (40 °C – 80 °C). As mentioned by Dash and Garimella [56], the characteristic velocity of fluid flow in a 3 μL water droplet evaporating on a 40 °C – 60 °C substrate is of tens of microns per second and the Peclet number is less than 1. Thus, it is reasonable for us to only consider the conduction heat transfer while neglecting the internal convection of the water droplet on a substrate with a relatively low temperature (40 °C – 80 °C). With the further increase of substrate temperature, more heat is transferred through the droplet and the temperature difference between the droplet top and bottom becomes larger. Fluid motion driven by the temperature gradient in the droplet becomes violent and the characteristic velocity of internal flow increases. Thus, we need to account for the effects of the droplet internal flow in the thermal circuit model for high temperature evaporation analysis.

Driven by the surface tension gradient (caused by the surface temperature gradient), water at the droplet bottom will flow upwards, which will in turn minish the temperature gradient on the droplet surface. As a result, the upper hemispherical part of the droplet will get warmed up by the up flowing hot water, and the temperature in the upper hemispherical portion should become relatively higher than the case without internal flow considered. To account for the effect of internal fluid flow, the overall averaged droplet cap surface temperature is calculated as the modified temperature:

$$T'_{\mathrm{model}} = \sum_{i=1}^{X} T_{\mathrm{i}} \cdot \Delta S_{\mathrm{i}} / 2\pi r_w^2 (1 - \cos\theta) \qquad \text{(2-26)}$$

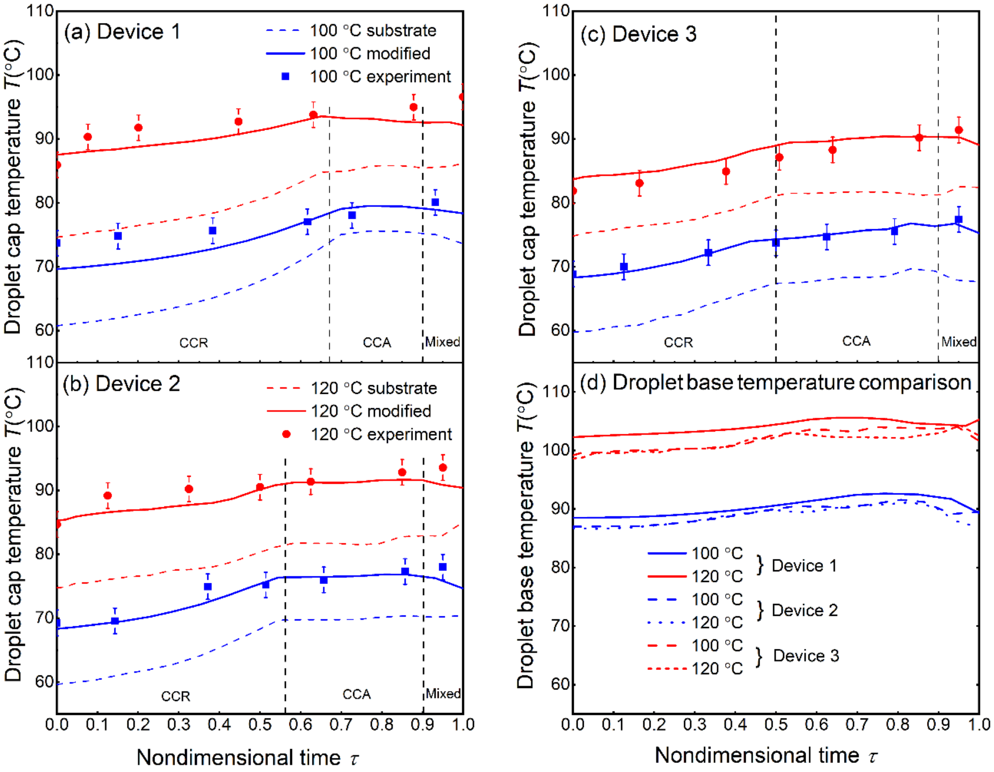

Figure 2-11. Evolution of droplet cap temperature on (a) device 1, (b) device 2 and (c) device 3. The dash lines represent the droplet cap temperatures calculated by thermal circuit model, the solid lines represent the droplet cap temperatures modified with total average temperature and effective conductivity, and the scatter dots are the experimental results by IR camera. (d) Evolution of droplet base temperature on devices 1, 2 and 3 with substrate temperature maintained at 100 °C and 120°C, respectively.

As shown in Figs. 11(a), (b) and (c), the modified temperature calculated by Eq. (26) matches well with the experimental data for droplet evaporation on devices 1, 2 and 3 with the substrate base temperature maintained at 100 °C.

But there still exist large deviations between the modified results and the experimental data for droplet evaporation on devices with the substrate temperature heated up to 120 °C. In this scenario, the convection heat transfer in the droplet cannot be neglected. In the thermal circuit model, only the conductive thermal resistance of the droplet is taken into account. Convection inside the droplet will remarkably enhance heat transfer therein and reduce the total thermal resistances of the droplet. Because of the complexity of internal flow, it is not practical to analyze the convection heat transfer simply based on the droplet characteristic velocity. Alternatively, an effective thermal conductivity is adopted to account for both the convection and conduction heat transfer in the droplet. As such, the effective conductivity[74] of an evaporating droplet is defined as:

$$k_{\mathrm{eff,w}} = e \cdot k_w \tag{2-27}$$

where e is a coefficient of the effective conductivity.

The effective conductivity $k_{\mathrm{eff,w}}$ is adopted in the thermal circuit model in place of the original water conductivity k_w to account for both the conduction and the convection heat transfer in the droplet. In this scenario, the effect of convection in heat transfer is approximately equivalent to an increase of the thermal conductivity of the working fluid. The minimum value of e allowing for the average difference between the model predicted surface temperature and the experimental value less than 2 °C, *i.e.*, $\left|\bar{T}_{\mathrm{model}} - \bar{T}_{\mathrm{expt}}\right| \leq 2\ ^{\circ}\mathrm{C}$, is chosen as the coefficient of the effective conductivity.

The coefficient e for the effective thermal conductivity of droplet evaporation on devices 1, 2 and 3 with the substrate temperature maintained at 120 °C was found to be 3.2, 2.9 and 2.7, respectively. Our estimates of coefficient e are very close to the numerically fitted coefficient of 2.72 that was reported by Abramzon and Sirignano[74]. In our experiments, these device substrates had been heated to a level over the boiling temperature of water. However, no boiling was observed in the droplet even with the substrate temperature reaching 120 °C, which is possibly due to the evaporative cooling at the droplet base. As evaporation at the droplet base could cool down the local surface temperature, we calculated the average temperature of the droplet base as shown in Fig. 11(d). For droplet evaporation on the 100 °C substrate, the base temperature was about 88 °C and for droplet evaporation on the 120 °C substrate, the base temperature was about 102 °C, which is very close to the saturation temperature of 100 °C. Our analysis shows that evaporation cooling from the droplet base can significantly delay the onset of droplet boiling with the substrate temperature even reaching 120 °C.

2.5. Conclusions

In this work, we experimentally and theoretically investigated the evaporation of water droplet on hot micro-pillared superhydrophobic surfaces. Prior studies on sessile droplet evaporation mainly focused on the Leidenfrost effect [75, 76] with the substrate temperature reaching 200 °C – 300 °C. Only few studies investigated the sessile droplet evaporation dynamics on substrates with a relative low temperature in the range of 40 °C – 100 °C and very limited attention had been paid to the evaporation from the droplet base. For the first time, the evaporation rate at the droplet base from the interstitial liquid-vapor interface between micropillars was carefully evaluated by us. According to our theoretical analysis, droplet cap temperature shows distinct trends in different evaporation modes, *i.e.*, droplet cap temperature increases in the CCR mode while keeping almost constant in the CCA mode. The total evaporation rate of the droplet generally decreases during the evaporation process. In the CCA mode, the decrease of the total evaporation rate of the droplet is largely induced by the decreasing evaporation rate from the droplet cap. In the CCR mode, however, the decrease of the total evaporation rate is mainly caused by the decreasing evaporation rate from the droplet base. The evaporation ratio φ decreases in the CCR mode and increases approaching the end of the CCA mode. Also, the evaporation ratio φ increases with the increasing substrate temperature during the early stage of evaporation when the droplet volume still remains relatively large. After the droplet shrinks to a small volume, the evaporation ratio φ decreases with the increasing substrate temperature.

Internal fluid motion starts playing a more influential role on droplet evaporation with a relatively high temperature (100 °C – 120 °C) on the substrate and an effective thermal conductivity $k_{\mathrm{eff,w}}$, which is about three times of water conductivity k_w, is employed by us as a correction factor for the thermal circuit model to account for the convection heat transfer in the water droplet. Furthermore, the average temperature at the droplet base was estimated and a large temperature difference between the droplet base and the substrate surface was unveiled. The apparent temperature differences between the droplet base and the substrate base are about 2 °C, 5 °C, 8 °C, 12.5 °C and 18 °C for the evaporating droplet on the micro-structured substrates with their base temperature maintained at 40 °C, 60 °C, 80 °C, 100 °C and 120 °C, respectively. Our study about the sessile droplet evaporation on hot micro-structured surfaces reveals that relative importance of heat and mass transfer from the droplet base. Moreover, the thermal circuit model developed by us provides a convenient tool to analyze the evaporation dynamics of a sessile droplet on hot micro-structured substrates with a broad range of surface temperature.

Chapter 3

Low-temperature Leidenfrost-like Jumping of Sessile Droplets on Microstructured Surfaces

Disclosure:

This chapter was adapted from a publication in the *Nature Physics*: Wenge Huang, Lei Zhao, Xukun He, Yang Li, C. Patrick Collier, Zheng Zheng, Jiansheng Liu, Dayrl P. Briggs, Jiangtao Cheng. "Low-temperature Leidenfrost-like Jumping of Sessile Droplets on Microstructured Surfaces" *Nature Physics* 20, 1274-1281 (2024).

3.1. Introduction

Research on the Leidenfrost effect dates back to Johann Gottlob Leidenfrost's observation of water droplets' blistering motions on a hot surface in the 18th century [77, 78]. Since then, intensive research has addressed this intriguing phenomenon due to its critical importance in various applications such as boiling heat transfer [79], spray cooling[80], electrospray printing, [81, 82] and additive manufacturing [83]. It is widely accepted that the continuous vapor cushion [29] formed beneath the Leidenfrost droplet eliminates the physical contact between the droplet and the surface [84] and consequently minimizes the interfacial hydrodynamic resistance [85] associated with the contact line pinning and solid-liquid friction [86], which is particularly useful for agile droplet manipulations [87, 88] and sustained liquid transport [12, 85]. However, the thermally-insulating vapor cushion also incurs a large thermal resistance [79] and leads to the severe degradation [32] of solid-liquid heat transfer, which is why a substantial surface temperature, *i.e.*, the Leidenfrost point (LFP), must be reached to sustain the intense liquid vaporization essential for droplet levitation. For water droplets on smooth metal surfaces, LFP is usually around 250 °C [85] whereas the effective heat flux is only one third of that on a 110 °C temperature substrate [89, 90]. Therefore, activation of the Leidenfrost-like droplet levitation without sacrificing the heat transfer performance deserves further research. Possible measures include surface engineering and wettability modifications [91] that can alter liquid vaporization and vapor bubble dynamics during the phase-change heat transfer.

As such, achieving maneuverable droplet levitation on hot engineered surfaces will be of great benefit for many applications in highly demanding heat transfer devices [92, 93]. One of the prominent examples is the purging of surface fouling agents [94], *i.e.*, the physical deposition of contaminating particulates on heat exchanging surfaces, which severely impairs the performance of thermal systems like boilers, condensers, and heat exchangers by impeding the effective heat exchange between the working liquids and the solid surface. In particular, this problem becomes further exacerbated for engineered heat transfer surfaces [14] that incorporate corrugations, posts, pyramids, and fins. In this scenario, neither Leidenfrost droplets nor cold droplets at room temperature, such as in spray cooling and tap water rinsing, can effectively remove the sticky fouling materials from surface roughness and cavities. The presence of a continuous vapor layer prevents Leidenfrost droplets from penetrating surface structures and contacting the fouling particles, whilst factors such as contact line pinning and interfacial friction also hinder the capability of cold droplets to effectively dislodge contaminants from wetted surfaces [95]. Methods to address these problems include the redesign of surface textures that allows the controllable wetting [96] and self-purging [95] of sessile droplets in a controllable manner, *i.e.*, the lotus effect, but the problem still remains a challenge.

In this work, we report a new discovery where controllable levitation and purging of sessile Wenzel-state droplets can be achieved at a temperature well below traditional LFP on an engineered surface decorated with micropillar arrays. Here we show that a fin-like micropillar array that penetrates into the droplet base significantly enhances the solid-liquid heat transfer and facilitates the propagation of the thermal boundary layer (TBL) [97], which fosters a superheated environment for inertia-controlled bubble growth [98]. The immense momentum gained from the droplet-bubble interaction eventually stimulates prompt droplet levitation and instantaneous jumping at a markedly low temperature of 130 °C. Decreasing the micropillar height switches the vapor bubble growth to a heat-transfer-limited mode [99] where the otherwise continuous bubble growth is interrupted by vapor condensation at the bubble-droplet interface, causing significant and prolonged vibration of a droplet prior to its jumping. We reveal the mechanisms underlying the tunable Leidenfrost-like droplet jumping by developing appropriate physical models to elucidate the roles of fine surface structures on bubble dynamics. Importantly, we demonstrate its applications in the facile removal of fouling materials from the cavities of hot engineered surfaces.

3.2. Droplet Explosive jumping

The surface, which consists of a square lattice of round posts with uniform diameter ($D = 20\ \mu\mathrm{m}$), post-to-post spacing ($L = 120\ \mu\mathrm{m}$) and height ($H = 80\ \mu\mathrm{m}$), hereafter named as $[D,\ L,\ H] = [20, 120, 80]\ \mu\mathrm{m}$, was fabricated on a silicon wafer by means of photolithography and deep reactive ion etching [100]. A thin layer of fluoropolymer was then applied via spin-coating to lower the surface energy of the substrate. The droplet levitation experiment was conducted by recording the dynamic behaviors of a sessile water droplet (diameter $D_\mathrm{d} \sim 2$ mm) by a high-speed camera at the rate of 10000 frames per second (Extended Data Fig. 1). At room temperature, the droplet remained in a stable Wenzel state[101] with a static contact angle of 118° ± 1° and a sliding angle of 67° ± 1° (Extended Data Fig. 2), due to the sparse distribution of micropillars. After the sessile droplet and the substrate were gently transferred onto a hot plate maintained at 130 °C (Extended Data Fig. 3), the droplet could be levitated and jump off in a Leidenfrost-like manner, *i.e.*, prompt droplet levitation enabled by the liquid vaporization.

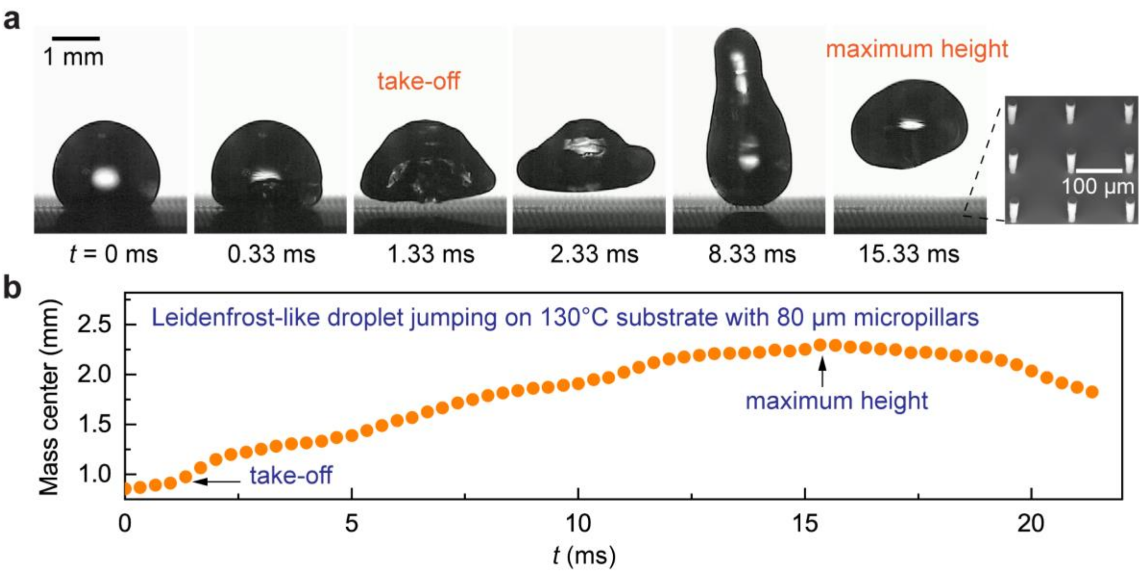

Figure 3-1. Leidenfrost-like droplet jumping dynamics on hot micropillared surface. **a** Selected snapshots of Leidenfrost-like droplet jumping on a micropillared substrate ($[\boldsymbol{D},\ \boldsymbol{L},\ \boldsymbol{H}] = [\mathbf{20}, \mathbf{120}, \mathbf{80}]\ \boldsymbol{\mu}\mathbf{m}$) with surface temperature $\boldsymbol{T}_\mathbf{w} = 130$ °C. The inset in (**a**) is the scanning electron micrography (SEM) of the micropillared substrate. **b** Height

variation of the center of mass of the droplet shown in (**a**). The time $\boldsymbol{t = 0\ \mathrm{ms}}$ denotes the onset of the interfacial deformation. Supplementary Movie S1 provides additional details.

The “cold” Leidenfrost phenomenon on modestly heated substrates has been reported in the past [86, 102-104]. However, what distinguishes our observations from those reported previously is that the low surface superheat utilized here not only triggers the non-wetting transition, but also gives rise to prompt droplet jumping. Fig. 1a shows selected snapshots of the Leidenfrost-like prompt jumping of a sessile water microdroplet. To investigate the kinematic dynamics of the droplet, the onset of the droplet shape deformation, resulting from the capillary perturbations caused by surface heating, was defined as $t = 0\ \mathrm{ms}$. After that, the droplet was levitated and directly jumped off the substrate within only $1.33\ \mathrm{ms}$. In contrast to the conventional thermally-driven droplet actuations, as in the case of trampolining drops in the traditional Leidenfrost effect [105], the droplet in this scenario exhibited an explosive upward motion. In Fig. 1b, its center of mass monotonically rose with time without any discernible oscillations and eventually reached the maximum jumping height of 2.3 mm at $t = 15.33$ ms, suggesting a distinct mechanism for droplet actuations.

3.3. Vapor Bubble expansion

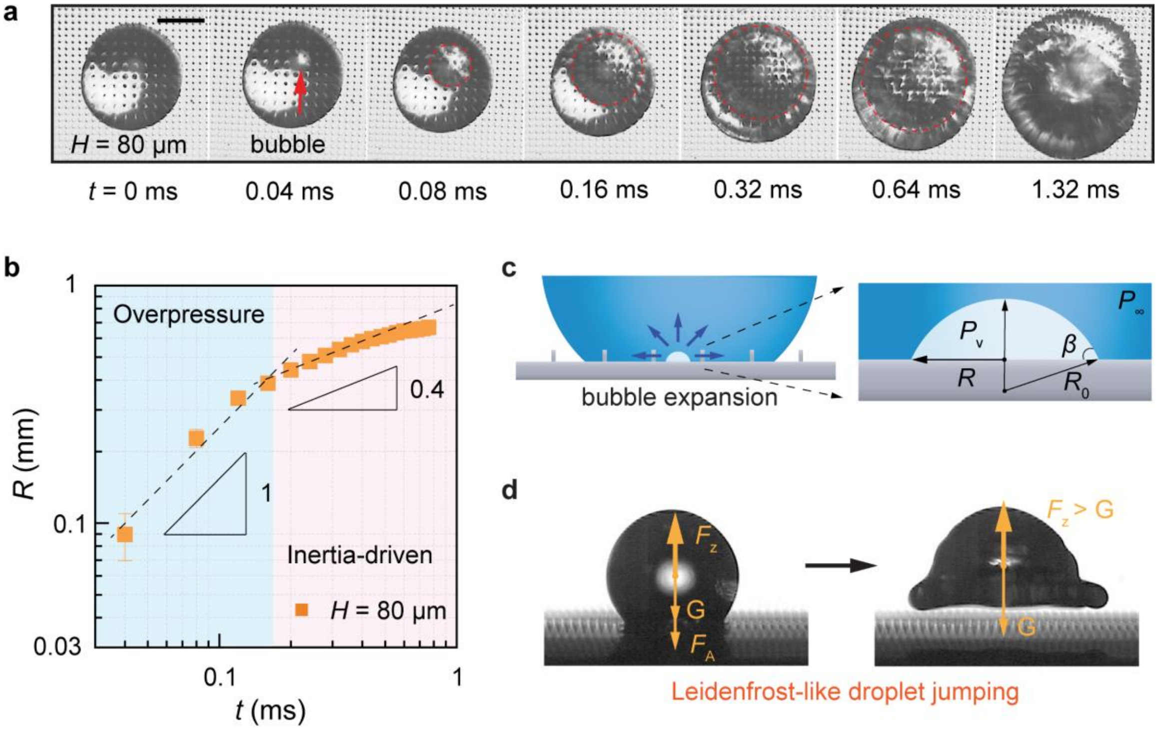

Figure 3-2. Rapid vapor bubble expansion for Leidenfrost-like droplet jumping. a Top-view snapshots of vapor bubble growth on substrate $[\boldsymbol{D},\ \boldsymbol{L},\ \boldsymbol{H}] = [\mathbf{20}, \mathbf{120}, \mathbf{80}]\ \boldsymbol{\mu}\mathbf{m}$ at 130 °C. The scale bar is 1 mm. Supplementary Movie S2 provides additional details. **b** Temporal evolution of the vapor bubble radius from (**a**). **c** Diagram of vapor bubble expansion via momentum interaction with the surrounding liquid. **d** Equivalent upward force generated by the rapid bubble expansion.

We show that the Leidenfrost-like droplet prompt jumping results from the rectification of the kinetic energy carried by the growing vapor bubble into the upward momentum that is sufficient to lift the entire droplet. At surface temperature $T_\mathrm{w} = 130$ °C, contact boiling occurred at the droplet base [90], leading to the successive nucleation and growth of individual vapor bubbles [99]. Fig. 2a shows that an individual vapor bubble firstly nucleated at $t = 0$ ms. After that, the vapor bubble expanded rapidly and reached the droplet's periphery at $t = 1.32$ ms. The striking coincidence between this timescale and the droplet’s dwelling time (1.33 ms) implies that the Leidenfrost-like droplet jumping is contingent on the momentum interactions between this individual vapor bubble and the sessile droplet.

A detailed inspection on the vapor bubble growth in Fig. 2b reveals a bubble expanding velocity as fast as $U_\mathrm{e} \approx$ 4 m/s, leading to an average Reynolds number of $Re = \frac{U_\mathrm{e} D_\mathrm{d}}{\nu} \approx 2 \times 10^4$ and Mach number of $Ma = \frac{U_\mathrm{e}}{c} \approx 2.6 \times 10^{-3}$, where ν is water kinematic viscosity and c is the speed of sound in water. Therefore, the effect of viscous dissipation and water compressibility could be neglected, indicating that the vapor bubble interface expansion follows an inertia-controlled mode[99] . This allows us to treat the vapor bubble expansion using the Rayleigh-Plesset equation in a potential flow approach [99]:

$$\rho_\mathrm{l} R \ddot{R} + \rho_\mathrm{l} \frac{3\dot{R}^2}{2} = \left(P_\mathrm{v} - P_\infty - \frac{2\sigma}{R}\right) \sin^2 \beta \tag{3-1}$$

where R is the bubble contact radius, ρ_l is water density, P_v is pressure inside the bubble, P_∞ is the pressure of bulk water, β is the bubble contact angle and σ is the surface tension, as shown in Fig. 2c. Eq. (1) describes how the overpressure-induced potential energy stored in the expanding vapor bubble is converted into the kinetic energy of the droplet (Supplementary Discussion 2). The vaporization-induced bubble overpressure could be estimated by the Clausius-Clapeyron equation[99] as $P_\mathrm{v} - P_\infty = \left(\frac{\Delta T}{T_\mathrm{sat}}\right) h_\mathrm{lv} \rho_\mathrm{v}$, where ΔT is the vapor bubble superheat temperature change, T_sat is the water saturation temperature, h_lv is specific evaporation enthalpy, and ρ_v is the vapor density. In general, ΔT would vary with time and the position in the bubble, but a constant ΔT could be assumed in the case of a strong thermal diffusion that makes the temperature gradient inside the bubble negligible[106]. This approximation holds true as long as the characteristic diffusion length $L_\mathrm{H} \sim \sqrt{2\alpha_\mathrm{v} t}$ is larger than the bubble size R, where α_v is the thermal diffusivity of water vapor. Using $\Delta T = 30$ K gives rise to a rough estimation of $P_\mathrm{v} - P_\infty \approx 1.08 \times 10^5$ Pa. As shown in Fig. 2b, the detected vapor bubble growth started from $R = 90$ μm, yielding the Laplace pressure $\frac{2\sigma}{R} \leq 1.31 \times 10^3$ Pa. Therefore, the Laplace pressure term in Eq. (1) is neglected. In the first stage of the bubble expansion with a constant ΔT, Eq. (1) can be solved analytically as:

$$R\,(t) = \left[\frac{2}{3}\left(\frac{\Delta T}{T_\mathrm{sat}(P_\mathrm{a})}\right)\frac{h_\mathrm{lv}\rho_\mathrm{v}}{\rho_\mathrm{l}}\right]^{\frac{1}{2}} \sin\beta \cdot t \tag{3-2}$$

Such a linear increase of $R(t)$ with time implies that the bubble expansion would eventually surpass the thermal diffusion [106], which has the time dependence $R \sim t^{0.5}$, after which the cooling effect of vaporization [106] causes ΔT to rapidly deteriorate at the liquid-vapor interface. The overpressure would quickly relax to zero [107], resulting in $P_{\mathrm{v}} - P_{\infty} - \frac{2\sigma}{R} \approx 0$. This prediction aligns well with the sharp turning of the bubble radius curve at $t_1 \approx 0.1\,\mathrm{ms}$ in Fig. 2b. At this moment, the bubble expansion was solely sustained by the droplet inertia and the total kinetic energy of the bubble-droplet system was conserved: $\frac{d}{dt}\left(\rho_{\mathrm{l}} R^3 \dot{R}^2\right) = 0$. The contact bubble radius R for $t > t_1$ can be solved as:

$$R = \left(R_1^{3/2} \dot{R}_1\, t\right)^{0.4} \tag{3-3}$$

where $R_1$is the contact radius at t_1. Fig. 2b shows a remarkable agreement between the experimental results of bubble expansion and the two-stage theoretical model proposed by us, further confirming the dominant role of the overpressure and inertia effect in controlling the bubble growth for Leidenfrost-like droplet jumping.

The inertia-controlled bubble growth contributes to the droplet levitation by its momentum exchange with the water droplet. The propulsive force is obtained by taking the derivative of the droplet's upward momentum M_z (Supplementary Discussion 3).

$$F_{\mathrm{z}} = \frac{dM_{\mathrm{z}}}{dt} \approx \frac{\pi \rho_{\mathrm{l}} R^2 \dot{R}^2 (4-3\cos\beta)\cos\beta}{\sin^4\beta} \tag{3-4}$$

Combining Eq. (3) and Eq. (4) gives an estimated value for $F_{\mathrm{z}} \approx 2.44 \times 10^{-3}\mathrm{N}$. As illustrated in Fig. 2d, the droplet gravity is $G = 4.16 \times 10^{-5}\mathrm{N}$, which is orders of magnitude smaller than F_{z}. Notably, the growing vapor bubble gradually separates the physical contact between the droplet base and the substrate, causing a continually decreasing surface adhesion. Therefore, with the rectified kinetic energy overwhelming the resistance, the water droplet became levitated and instantaneously jumped off the substrate without apparent oscillations, in a Leidenfrost-like manner but at a markedly low temperature of 130 °C.

3.4. Droplet vibration jumping

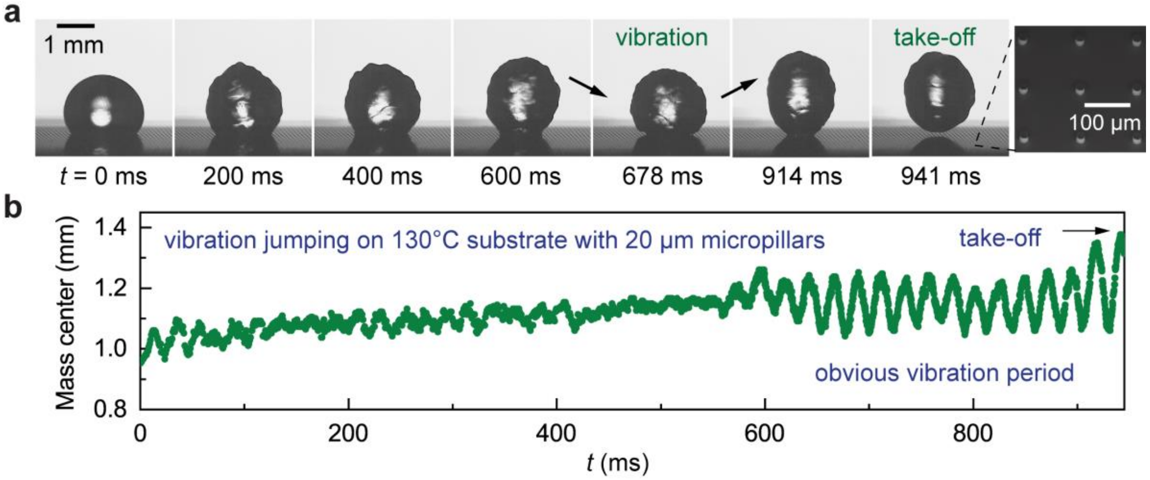

Figure 3-3. Droplet vibration jumping dynamics on hot micropillared surface. a Selected snapshots of droplet's vibrational jumping on the micropillared substrate $[\boldsymbol{D},\ \boldsymbol{L},\ \boldsymbol{H}] = [\mathbf{20}, \mathbf{120}, \mathbf{20}]$ **μm** at 130 °C. The inset in (**a**) is the SEM image of the micropillared substrate. **b** Height variation of the center of mass of the droplet shown in (a). Supplementary Movie S3 provides additional details.

We find the Leidenfrost-like droplet jumping breaks down on substrates with shorter pillars as the droplet-vapor dynamics become different. Fig. 3a presents the selected snapshots of a droplet's actuation on a substrate with short micropillars ($H = 20$ μm). In contrast to the direct Leidenfrost-like jumping, the droplet experienced substantial vertical stretching and vibrations until its ultimate jump off with an extended dwelling time of 941 ms, which is >700 times greater than that for Leidenfrost-like jumping. In Fig. 3b, the droplet actuations could be generally divided into two stages. Before $t = 600$ ms, the droplet fluctuated randomly with a small magnitude and no apparent periodicity. After $t = 600$ ms, the oscillations became more pronounced with an evident frequency of 41.6 Hz, which is consistent with the characteristic frequency of a water spring in bouncing drops [108]. Therefore, we term this phenomenon as vibrational droplet jumping, as the droplet's dwelling time is increased by hundreds of times due to the prolonged vibrations.

3.5. Vapor bubble shrinking

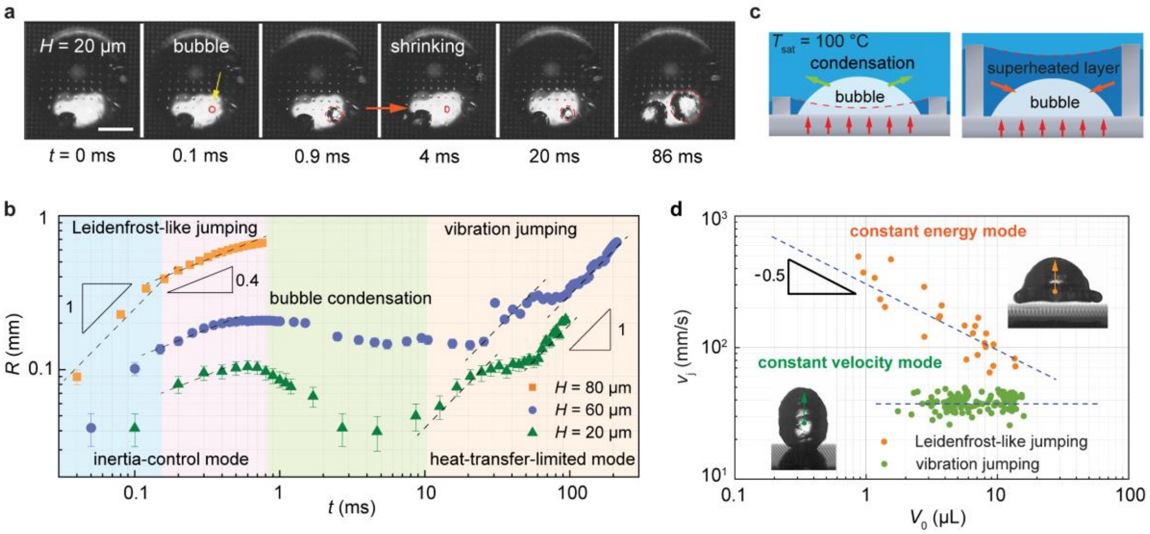

Figure 3-4. Vapor bubble shrinking during the vibrational droplet jumping. a Top-view snapshots of vapor bubble growth on substrate $[\boldsymbol{D},\ \boldsymbol{L},\ \boldsymbol{H}] = [\mathbf{20}, \mathbf{120}, \mathbf{20}]\ \boldsymbol{\mu}\mathbf{m}$ at 130 °C. **b** Temporal evolution of vapor bubble radius on substrates with different micropillar heights ($\boldsymbol{H} = \mathbf{20}, \mathbf{60}, \mathbf{80}\ \boldsymbol{\mu}\mathbf{m}$). Supplementary Movies S4 and S5 provide additional details. **c** Schematic illustrations of superheated interfacial water layer impacting the bubble growth. The growing vapor bubble condensates after meeting the subcooled water outside the TBL. **d** Jumping velocity of droplets with different volumes during vibrational jumping (on substrate $[\boldsymbol{D},\ \boldsymbol{L},\ \boldsymbol{H}] = [\mathbf{20}, \mathbf{120}, \mathbf{20}]\ \boldsymbol{\mu}\mathbf{m}$) and Leidenfrost-like jumping (on substrate $[\boldsymbol{D},\ \boldsymbol{L},\ \boldsymbol{H}] = [\mathbf{20}, \mathbf{120}, \mathbf{80}]\ \boldsymbol{\mu}\mathbf{m}$).

To unveil the mechanism of vibrational droplet jumping, we investigated the dynamics of individual growing bubble as represented by the snapshots in Fig. 4a. Initially, the vapor bubble followed an inertia-controlled expansion (Fig. 4b) because the bubble expansion is always initiated by the vaporization-induced overpressure. However, the bubble growth in vibrational droplet jumping was interrupted by an apparent bubble shrinking process (from 0.9 ms to 4 ms), causing the bubble radius to decrease for several milliseconds and then rise again as shown in Fig. 4b (Extended Data Fig. 4). This intermittent shrinking is attributed to the limited propagation of the TBL, within which the liquid becomes superheated due to surface heating but remains subcooled elsewhere. For the thermal interaction between the sessile droplet and the heating substrate, the thermal timescale

[109] can be estimated as $\tau_{\mathrm{th}} = \frac{K_{\mathrm{w}}\rho_{\mathrm{l}}c_{\mathrm{p}}}{h_{\mathrm{c}}^2} \approx 25$ ms with K_{w} being the thermal conductivity of liquid water, c_{p} being the thermal capacity of liquid water and $h_{\mathrm{c}} \approx 10000$ W/(m^2·K) being the estimated convective heat transfer coefficient between the droplet and the substrate [99]. The Fourier number characterizing the extent of heat conduction is estimated to be $Fo = \frac{\alpha_{\mathrm{w}}\tau_{\mathrm{th}}}{D_{\mathrm{d}}^2} = 1.05 \times 10^{-3}$, verifying the presence of a thin TBL with a steep temperature gradient. Here α_{w} is the thermal diffusivity of liquid water. Then the TBL propagation velocity v_{TBL} can be further evaluated by solving the heat transfer equation at the droplet base (Supplementary Discussion 4).

$$v_{\mathrm{TBL}} = \mathrm{erf}^{-1}\left(\frac{T_{\mathrm{sat}}-T_{\mathrm{w}}}{T_0-T_{\mathrm{w}}}\right)\sqrt{\frac{\alpha_{\mathrm{w}}}{t}} \tag{3-5}$$

where $T_0 = 20$ °C is the initial temperature of water. Specifically, the characteristic TBL propagation velocity can be evaluated as $v_{\mathrm{c,TBL}} \approx 6.4 \times 10^{-4}$ m/s by substituting $t = \tau_{\mathrm{th}}$. This value is three orders of magnitude smaller than the inertial-controlled bubble expansion $U_{\mathrm{i,e}} \approx 4$ m/s. Therefore, the inertial bubble expansion would inevitably surpass the TBL propagation whilst the TBL thickness remains almost constant. As depicted in Fig. 4c, the vapor inside the bubble would condensate once its outer edge breaches the TBL. The bubble growth can continue only if the heat transfer from the substrate eventually surpasses the energy loss via condensation, indicating a heat-transfer-limited mode. Therefore, we applied the energy balance to describe the bubble expansion herein:

$$h_{\mathrm{lv}}\rho_{\mathrm{v}}\frac{d}{dt}\left(\frac{\pi}{3}\frac{(2+\cos\beta)(1-\cos\beta)^2}{\sin^3\beta}R^3\right) = 2\pi R^2 q_{\mathrm{b}} \tag{3-6}$$

where q_{b} represents the heat flux from the silicon substrate to the bubble base. Specifically, the convective heat flux can be estimated as $q_{\mathrm{b}} = h_{\mathrm{c}}(T_{\mathrm{w}} - T_{\mathrm{sat}})$. As a result, the temporal evolution of vapor bubble radius in this stage follows:

$$R\,(t) \sim \frac{q_{\mathrm{b}}}{h_{\mathrm{lv}}\rho_{\mathrm{v}}}\frac{2\sin^3\beta}{(2+\cos\beta)(1-\cos\beta)^2}\cdot t \tag{3-7}$$

Such a linear growth of bubble with time is validated by our experimental results as shown in Fig. 4b.

The propulsive force provided by the heat-transfer-limited bubble growth can be evaluated by combining Eqs. (4) and (7), yielding $F_{\mathrm{z}} \approx 2.16 \times 10^{-6}$ N. Given the droplet gravity $G = 4.16 \times 10^{-5}$ N, the water droplet could not be completely levitated by an individual expanding bubble. The droplet hence entered the trampolining mode with strong capillary oscillations caused by droplet-bubble interactions, until it could build up sufficient kinetic energy for subsequent jumping [105, 110, 111].

3.6. Effect of substrate on droplet jumping behavior

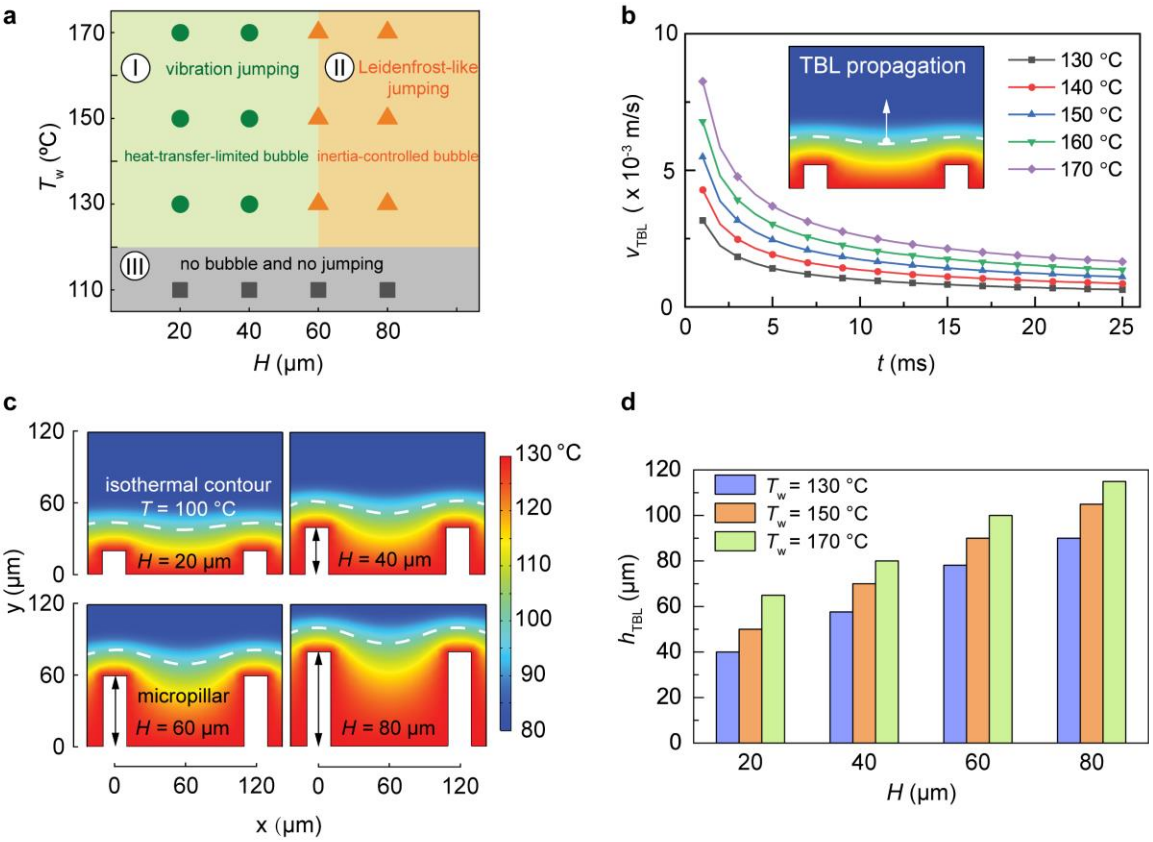

Figure 3-5. Effect of micropillar height H and surface temperature T_w on droplet jumping behavior. a Phase map of occurrence of droplet jumping behaviors on substrates with different micropillar heights and different substrate temperatures. **b** Theoretical prediction of the TBL propagation velocity at different substrate temperatures. **c** Simulated results of temperature distribution showing the TBL on substrates with micropillar height from $\mathbf{20\ \mu m}$ to $\mathbf{80\ \mu m}$. The isothermal contour of 100 °C is donated with white dash line. **d** Simulated TBL thickness on substrates with different micropillar heights (from $\mathbf{20\ \mu m}$ to $\mathbf{80\ \mu m}$) and different substrate temperatures (from 130 °C to 170 °C).

A detailed analysis on the droplet jumping velocity v_j versus the droplet volume V_0 reveals two distinct jumping modes as delineated in Fig. 4d. For Leidenfrost-like droplet jumping, the kinetic energy E_k of the jumping droplet originates from the overpressure potential energy of an individual bubble, which is mainly determined by the superheat[99]. The initial potential energy stored in each individual vapor bubble formed inside droplets with varying volumes can be taken at the same level, considering the droplets are deposited on the substrate with identical surface temperature. As a result, the kinetic energy $E_\mathrm{k} \sim \frac{1}{2}\rho_\mathrm{l} V_0 v_\mathrm{j}^2$ is approximately constant for different droplet volume V_0, yielding a scaling of $v_\mathrm{j} \sim V_0^{-0.5}$ as manifested by Leidenfrost-like droplet jumping (Fig. 4d). For vibrational jumping on the substrate $[D,\ L,\ H] = [20, 120, 20]$ µm, the droplet needs to overcome the gravity G and surface adhesion from the substrate F_A. The surface adhesion F_A is proportional to the pillar perimeter [112] $\sigma\pi D$ and the number of pillars under the droplet base $\left(\frac{D_\mathrm{d}}{L}\right)^2$, giving $F_\mathrm{A} \sim \frac{\sigma\pi D}{L^2} {D_\mathrm{d}}^2 \approx 1.27 \times 10^{-3}$ N. The droplet gravity $G = 4.16 \times 10^{-5}$ N is thus neglected in the force analysis. The propulsive force is scaled by considering the temporal variation of momentum as $F_z \sim \rho_\mathrm{l} D_\mathrm{d}^3 \frac{v_\mathrm{j}}{D_\mathrm{d}/v_\mathrm{j}}$. A threshold velocity acquired by $F_\mathrm{z} = F_\mathrm{A}$ marks the onset of droplet levitation, yielding $v_\mathrm{j} \sim \sqrt{\frac{\sigma D}{L^2 \rho_\mathrm{l}}}$ for vibrational jumping. This prediction indicates that all water microdroplets jump with a constant velocity, aligning well with the observed jumping velocities as shown in Fig. 4d.

To comprehensively understand the influence of micropillars on the droplet-substrate heat transfer and two distinct jumping modes, we conducted experiments of droplet jumping on substrates with varying temperature T_w and pillar height H. The phase map in Fig. 5a depicts three different regimes of droplet behaviors. Increasing T_w above 130 °C gave rise to the vibrational droplet jumping (regime I) and Leidenfrost-like droplet jumping (regime II). We emphasize that the jumping mode is predominantly determined by the micropillar height H and increasing T_w does not necessarily initiate the vibration-to-Leidenfrost-like transition. Specifically, the vibrational droplet jumping occurred for $H <$ 60 µm even with $T_\mathrm{w} =$ 170 °C (Extended Data Fig. 5), and the Leidenfrost-like droplet becomes probable only when $H \geq$ 60 µm. This is a strong indication of the fact that increasing T_w does not impact the TBL propagation whilst the structure of the TBL could be significantly altered by the microstructures. Such effect can be examined by revisiting Eq. (5) to estimate the TBL propagation velocity v_TBL, as shown in Fig. 5b. Increasing T_w from 130 ℃ to 170 ℃ only increases v_TBL by 78.6% from 6.4×10^{-4} m/s to 1.1×10^{-3} m/s, still orders of magnitude smaller than the inertia-controlled bubble expansion ($U_\mathrm{i,e} \approx$ 4 m/s). Therefore, during the short-time inertial bubble expansion that determines the ultimate droplet jumping mode, the TBL remains almost unchanged even when T_w is increased significantly. We conducted heat transfer simulations on COMSOL® 5.6 to investigate the effect of micropillars on the distribution of TBL (Supplementary Discussion 5). Specifically, Fig. 5c shows that the temperature distribution in the vicinity of the substrate. The isothermal contour of $T = 100$ ℃, which marks the boundary of the TBL, conforms to the profile of micropillars, suggesting that the microstructures act as micro-fins to extend the superheated liquid domain. We define the TBL thickness as $h_\mathrm{TBL} = \frac{V_\mathrm{sup}}{L_\mathrm{p}}$, where V_sup corresponds to the total volume of superheated liquid and L_p is the projected length of the computational domain (Supplementary Discussion 5). We compare h_TBL at different T_w and H in Fig. 5d. Increasing T_w from 130 ℃ to 170 ℃ only marginally increases h_TBL from 90 μm to 115 μm, aligning well the theoretical prediction of Eq. (5) that $\Delta h_\mathrm{TBL} = \int_0^{\tau_\mathrm{th}} [v_\mathrm{TBL}(T_\mathrm{w} = 170\ ℃) - v_\mathrm{TBL}(T_\mathrm{w} = 130\ ℃)]dt \approx 20$ μm. Alternatively, for $T_\mathrm{w} = 130$ ℃, h_TBL is substantially increased from 40 μm to 90 μm when the pillar height is increased from 20 μm to 80 μm, confirming that the effect of microstructures in extending the TBL. Moreover, in regime III of Fig. 5a where T_w is below 120 °C, no vapor bubble can be observed and the droplet would steadily remain in the Wenzel state till complete evaporation, due to the insufficient thermal energy input for bubble formation and growth.

We demonstrate that engineering surface microstructures to manipulate the growth of bubble expansion and droplet jumping behaviours can be employed as an effective strategy for rapid droplet shedding on hot substrates. Figs. 6a and 6b show time-lapsed images of ejection of sessile water droplets on tilted substrates with different pillar heights. For the tilted substrate $[D,\ L,\ H] = [20, 120, 20]$ μm, the vibrating droplet initiated the out-of-plane jumping and then the water droplet landed softly on the substrate remaining in the low-friction Cassie state until it slid off the substrate. For the tilted substrate $[D,\ L,\ H] = [20, 120, 80]\ \mu\mathrm{m}$, the explosive droplet jumping caused the droplet to jump off the substrate with a maximum height of 6 mm, which is three times as large as the droplet diameter. Then the droplet experienced repetitive rebounding and falling for several cycles before it finally rolled off the substrate.

The rapid shedding of initially sticky droplets on heated substrates is of particular relevance to the fouling removal on the highly-demanding heat exchanger surfaces. Under spray cleaning or rinsing conditions, neither Leidenfrost nor cold droplets effectively eliminate deposited particulates from surface roughness. A continuous vapor layer restricts Leidenfrost droplets from accessing surface structures, while factors like contact line pinning and interfacial friction impede the ability of cold droplets to dislodge contaminants. Fig. 6c illustrates an alternative process of removing fouling in the interstitial cavities of surfaces by leveraging the explosive droplet jumping discovered by this work. The contaminant used in the experiments was hydrophilic prism polishing powder (~ 3 μm in diameter). To mimic the gradual deposition of particles on the surface of heat exchangers, the powder particles are suspended in a water droplet with later evaporation process to deposit them on the surface, which is analogous to coffee ring effect[113](Supplementary Discussion 6). At first, the droplet was in Wenzel state, which allows it to penetrate into the interstitial cavities to catch the contaminants. As the surface temperature was heated up to a moderate level ($T_\mathrm{w} = 130$ °C), the generation of vapor bubbles effectively dislodged the residual contaminant particles and drove them to suspend in the droplet. Along with the droplet jumping, the fouling even in surface roughness and cavities can be effectively purged in a deep cleaning manner.

3.7. Conclusions

We envisage that the above-mentioned strategy for facile actuations of sessile liquid droplets in an ultrafast, yet controlled manner has a wide range of applications in highly demanding heat transfer and fluid manipulation scenarios. Particularly, this study paves a new path for the deep cleaning of fouling settled in surface cavities, a critical factor that tends to lead to the severe performance degradation of engineered surfaces. From a broader perspective, the exploration of minimizing the thermal cost associated with the vapor-mediated droplet actuations represents an important advance in our understanding of the complex transport of momentum, mass and heat in the phase change heat transfer process, enabling the rational design of surfaces with exceptional heat transfer performance, extended durability, and excellent anti-fouling properties.

Chapter 4

Bubble-Burst-induced Puddle Jumping

Disclosure:

This chapter was adapted from a publication in the manuscript: Wenge Huang, Mohammad Shamsodini Lori, Huachen Cui, Kai Zhuang, Anchenyi Yang, Mojun Chen, Chao Sun, Yuanyuan Duan, Tingzhen Ming, Jiangtao Cheng. “Bubble Burst-induced Large Droplet Jumping Beyond the Capillary Length”.

4.1. Introduction

Droplet jumping widely exists in nature such as raindrops splashing on plant leaves or ricocheting off animal furs. It plays important roles not only in various natural processes, such as disease transmission [114], pollen and seed dispersion [115], but also in many agricultural and industrial applications, including insecticide deposition [116, 117], surface self-cleaning [118-120], inkjet-printing [121, 122], heat transfer and combustion [123, 124]. As a result, extensive research on droplet jumping has been conducted over the past two decades [125-130]. Despite this, the majority of the studies have focused on droplets ranging from micrometer to millimeter scale, with very limited exploration into the self-actuations of even larger droplets. In general, the droplet jumping process involves the exchange of mass, momentum and energy between the droplet and the surface. Maximizing droplet size is often beneficial for improving transfer efficiency, and as such, strategies for enabling large droplet jumping require more attention. However, according to the conventional hydrodynamic theory [131], the balance of gravity and capillarity imposes a theoretical capillary length limitation on droplet size (~2.7 mm for water), beyond which gravitational force becomes dominant over capillarity, preventing droplets from out-of-surface jumping [132, 133]. Of relevance is that the jumping and propagation of micrometer-sized droplets are primarily governed by capillarity and can be easily achieved by liquid fragmentation or splashing processes. For millimeter-scale droplets, gravity plays a more influential role and out-of-surface jumping, either by impact-incurred rebound [7, 111, 134] or by coalescence-induced jumping [35, 135, 136], heavily relies on the development of low-adhesion surfaces. For even larger puddles in centimeter scale, the gravitational force dominates over capillarity, making their out-of-surface jumping more challenging [132, 133, 137-139]. As shown in Figs. 1a and 1b, water puddles of ~8 mm in diameter (250 µL in volume) generally remained on the surfaces without jumping, whether through impact-rebound or coalescence mechanisms. This capillary length limitation restricts our ability to achieve out-of-surface jumping for puddles, hindering both fundamental understanding and potential broader applications.

Here, we demonstrate a strategy for achieving droplet out-of-plane jumping through the bursting of embedded bubbles without the capillary length limitation on the droplet size (Fig. 1c). In essence, the released surface energy from both the inner and outer surfaces of the bursting bubble drives the droplet jumping process. Specifically, the bursting bubble generates capillary waves that propagate nearly vertically towards the substrate and the droplet retracts immediately with minimal spreading during the capillary waves impact. With sufficient surface energy released, this bubble burst-based strategy enables effective momentum transfer through the direct and localized capillary waves-solid surface interaction, which can lift a puddle in the centimeter scale (280 µL in volume) as shown in Fig. 1d.

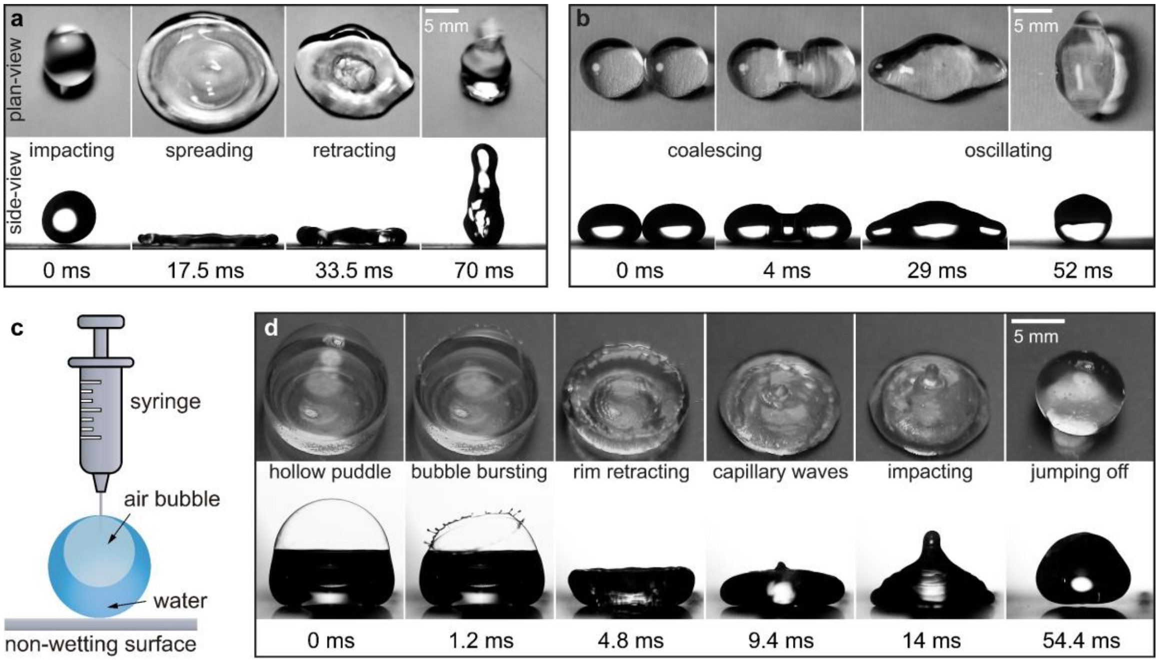

Figure 4-1. Bubble burst-induced puddle jumping. a Selected plan-view and side-view snapshots of a water puddle impacting, spreading, and retracting on a superhydrophobic surface, without achieving out-of-surface jumping. The puddle of 250 µL impacted the

surface at a velocity of 0.6 m/s. During the impacting process of this puddle, a spreading lamina formed and its retraction and oscillation invariably dissipated a large amount of energy. Hence, the gravitational force became influential, leading to droplet flattening on the surface and impeding its counter-gravity motion. **b** Selected snapshots of coalescence of two water puddles of 125 μL each on a superhydrophobic surface, without achieving out-of-surface jumping. Even though the coalescence released excess surface energy and triggered the liquid-bridge impact, it concurrently accumulated the mass of each individual droplet to the merged one, thereby causing additional gravitational and viscous resistances to the puddle's actuations. **c** The experimental setup for studying bubble burst-induced puddle jumping. An air bubble is carefully injected into a puddle on the non-wetting surface, forming a stable hollow droplet. **d** Selected plan-view and side-view snapshots of bubble burst-induced out-of-surface jumping of a puddle. A water puddle of 280 μL was first placed on a superhydrophobic surface. Then an air bubble was injected into the puddle as shown in the first snapshot at $t = 0$ ms. Continuous drainage from the bubble cap eventually caused a puncture thereon, leading to a circularly expanding hole surrounded by a loop of liquid rim. The receding rim on the curved bubble cap surface experienced centripetal acceleration, inducing inertia-driven destabilization of the rim and subsequently resulting in the formation of regularly spaced ligaments, as depicted in the snapshot at $t = 1.2$ ms. Thus-incurred capillary waves transmitting downwards along the puddle surface finally impacted the substrate at $t = 14$ ms, causing the droplet to rebound and achieve out-of-plane jumping at $t = 54.4$ ms.

4.2. Bubble burst-induced droplet jumping

To achieve a comprehensive understanding of bubble bursting dynamics in droplets, we conducted parametric studies by varying water droplet volume from 6.5 μL to 350 μL and adjusting the size of the embedded bubble accordingly. (Supplementary movies 1-2). As such, we started with a small droplet with a radius $R_\mathrm{d} \approx 1.1$ mm (6.5 μL in volume) sitting on a non-wetting surface. Then an air bubble with a radius R_b was carefully injected into it (with $R_\mathrm{b}/R_\mathrm{d} = 0.6$), forming a stable hollow droplet with a radius R_h, as depicted in Fig. 2a. With the Bond number $Bo = \rho_\mathrm{d} g R_\mathrm{d}^2/\gamma \approx 0.18 \ll 1$and Ohnesorge number $Oh = \mu_\mathrm{d}/\sqrt{\gamma \rho_\mathrm{d} R_\mathrm{d}} \approx 0.0034 \ll 1$, the droplet resembled an almost perfect sphere with neglected viscous effect. Here, ρ_d is the liquid density, g the gravitational acceleration, γ the surface tension coefficient and μ_d the dynamic viscosity of liquid. The non-wetting surface was prepared by spin-coating a thin layer of nanoparticle-contained fluoropolymer (FluoroPel PFC M1604V, Cytonix) on a smooth silicon wafer. The droplet exhibited a contact angle of 164° ±1° on thus-prepared surface with a sliding angle of ~1°, further manifesting its non-adhesive nature.

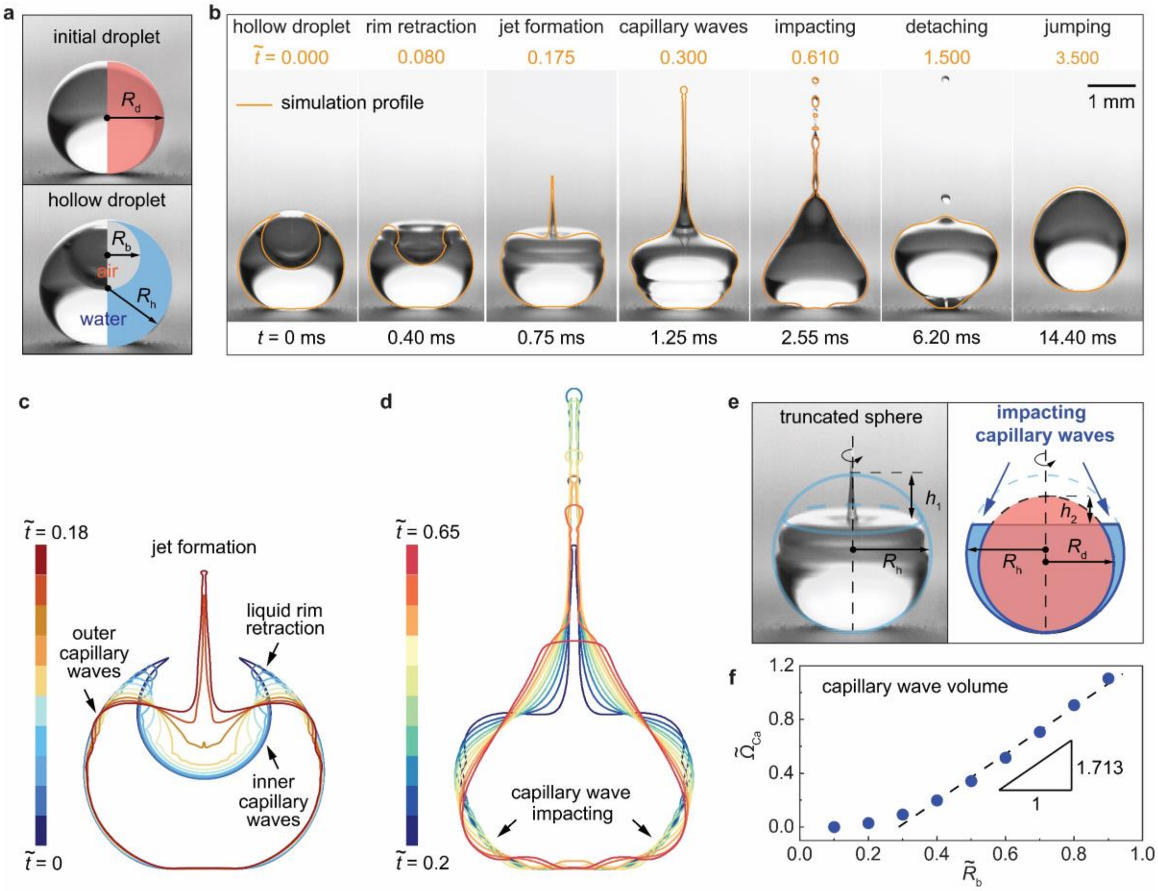

Figure 4-2. Generation of capillary waves on droplet surface via bubble burst. a Illustration of the geometry radii of the initial water droplet $\boldsymbol{R}_\mathbf{d}$, injected air bubble $\boldsymbol{R}_\mathbf{b}$ and hollow droplet $\boldsymbol{R}_\mathbf{h}$. Left parts are experimental images, whereas the right parts are schematics for illustration purpose. **b** Time-lapsed snapshots of bubble burst-induced droplet out-of-surface jumping. These snapshots are overlaid with the DNS-simulated droplet profiles in orange, demonstrating excellent agreement. The time $\boldsymbol{t}$ below each snapshot is the experimental time, while the time $\tilde{\boldsymbol{t}}$ above each snapshot corresponds to the time nondimensionalized by the inertia-capillary time $\boldsymbol{\tau} = \sqrt{\boldsymbol{\rho}_\mathbf{d}\boldsymbol{R}_\mathbf{d}^3/\boldsymbol{\gamma}}$ from the DNS

simulations. The droplet has $\boldsymbol{Bo} = \mathbf{0.18}$ with the nondimensionalized bubble radius $\widetilde{\boldsymbol{R}}_{\mathbf{b}} = \boldsymbol{R}_{\mathbf{b}}/\boldsymbol{R}_{\mathbf{d}} = \mathbf{0.6}$. **c** Temporal evolution of the hollow droplet profile obtained from DNS simulations, illustrating liquid rim retraction, cavity collapse and jet formation after bubble burst. **d** Temporal evolution of droplet profile obtained from DNS simulations, demonstrating the capillary wave propagation and impacting on the substrate. The nondimensional time $\tilde{\boldsymbol{t}}$ is color-coded, progressing from blue to red. **e** Formation of the truncated sphere droplet and the geometric definition of the impacting capillary waves. **f** Plot of the nondimensionalized volume of the capillary waves $\widetilde{\boldsymbol{\Omega}}_{\mathbf{Ca}}$, as defined in e, versus the injected bubble size $\widetilde{\boldsymbol{R}}_{\mathbf{b}}$. It can be seen that $\widetilde{\boldsymbol{\Omega}}_{\mathbf{Ca}}$ scales almost linearly with $\widetilde{\boldsymbol{R}}_{\mathbf{b}}$ for $\widetilde{\boldsymbol{R}}_{\mathbf{b}} > \mathbf{0.3}$.

4.3. Direct numerical simulation

The dynamic processes of bubble burst-induced droplet jumping were captured by high-speed photography, as illustrated in Fig. 2b. The bubble film rupture on the cap occurred at $t = 0$ ms. Subsequently, the initial orifice widened circularly due to the capillarity, following the Taylor-Culick type retraction [140, 141]. Interestingly, the retraction of thus-formed liquid rim generated capillary waves both within the bubble cavity and on the exterior surface of the droplet as shown in Fig. 2b at $t = 0.4$ ms and further detailed in Fig. 2c. Those internal capillary waves converged at the bottom of the cavity, initiating the formation of the Worthington jet [142] as observed at $t = 0.75$ ms. Simultaneously, capillary waves on the droplet's exterior surface traveled downwards and impacted almost normally on the surface, as shown in the snapshots from $t = 1.25$ ms to 2.55 ms. In contrast to the impact of the entire droplet body, here we assume that it is the surface capillary waves with a limited volume Ω_{Ca} that impact locally and directly on the substrate. According to the classical impacting model [7], which treats the droplet as a mass-spring system with the impacting time $\tau_{\mathrm{c}} \sim \sqrt{m/\gamma}$ mainly determined by the impacting mass m, the limited impacting mass of the capillary waves, $\rho_{\mathrm{d}}\Omega_{\mathrm{Ca}}$, would result in a remarkably shortened impacting time compared to droplet bulk impacting mode and consequently lead to constrained lateral spreading[143] after $t = 2.55$ ms. Thus, the contact area at the droplet base promptly shrank without substantial spreading after the impacting, lifting the droplet's center of mass in a more efficient fashion. Eventually, the droplet detached the surface at $t = 6.2$ ms and reached its maximum height at $t = 14.40$ ms. Additionally, to quantitatively characterize the liquid rim retraction, capillary wave impacting and droplet jumping processes, we performed direct numerical simulations (DNS) using the open-source platform Basilisk [144, 145] (Supplementary Discussion 1). We initiated the simulation with an open cavity inside the sessile droplet and the subsequent evolutions of the simulated droplet profiles with the nondimensional time ($\tilde{t} = t/\sqrt{\rho_\mathrm{d} R_\mathrm{d}^3/\gamma}$) exhibit excellent agreement with the experimental images, as shown in Fig. 2b (further comparisons are available in Supplementary movies 1-2). In the following, the dimensionless quantities are represented by adding a tilde hat. The time and length scale used for nondimensionalization are $\sqrt{\rho_\mathrm{d} R_\mathrm{d}^3/\gamma}$ and R_d, respectively.

Figures 2c and 2d illustrate the temporal evolutions of the liquid rim retraction, cavity collapse and jet formation processes (from $\tilde{t} = 0$ to 0.18) and the propagation of capillary waves transmitting downwards along the droplet surface (from $\tilde{t} = 0.2$ to 0.65), respectively, as obtained from DNS, with the progression color-coded from blue to red. A close look at Fig. 2c reveals that the retracting liquid rim quickly filled the bursting bubble cavity while the remainder of the droplet profile remained almost unaltered. This occurred because the retraction velocity of the liquid rim, initiated by a singularity tip, overwhelms the droplet's radial shrinking velocity [146] (Supplementary Discussion 2). Upon filling of the bubble cavity, the droplet resembled a truncated spherical shape with a radius approximated to R_h (neglecting the relatively small volume of the jet) as shown in the left panel of Fig. 2e. The profiles in Fig. 2d illustrate the time-lapsed traces of the capillary wave trains, thereby roughly indicating the domain where the surface capillary waves were present. Due to the surface tension, the deformed truncated-sphere droplet tended to restore to its spherical shape. Thus, in this work, the non-overlapping region between the truncated sphere and the original droplet sphere is defined as the domain of capillary waves transmitting on the droplet surface, which is highlighted in blue in the right panel of Fig. 2e. Consequently, the volume of the capillary waves $\Omega_\mathrm{Ca}(R_\mathrm{b}, R_\mathrm{d})$ can be determined based on this geometric configuration (Supplementary Discussion 3). With R_d held constant, it is found that Ω_Ca increases almost linearly with R_b, as manifested in Fig. 2f. Therefore, a scaling relation that links the volume of the impacting capillary waves to the size of the injected bubble reads:

$$\tilde{\Omega}_{\mathrm{Ca}} \sim \tilde{R}_{\mathrm{b}} \qquad \text{for } \tilde{R}_{\mathrm{b}} > 0.3 \tag{4-1}$$

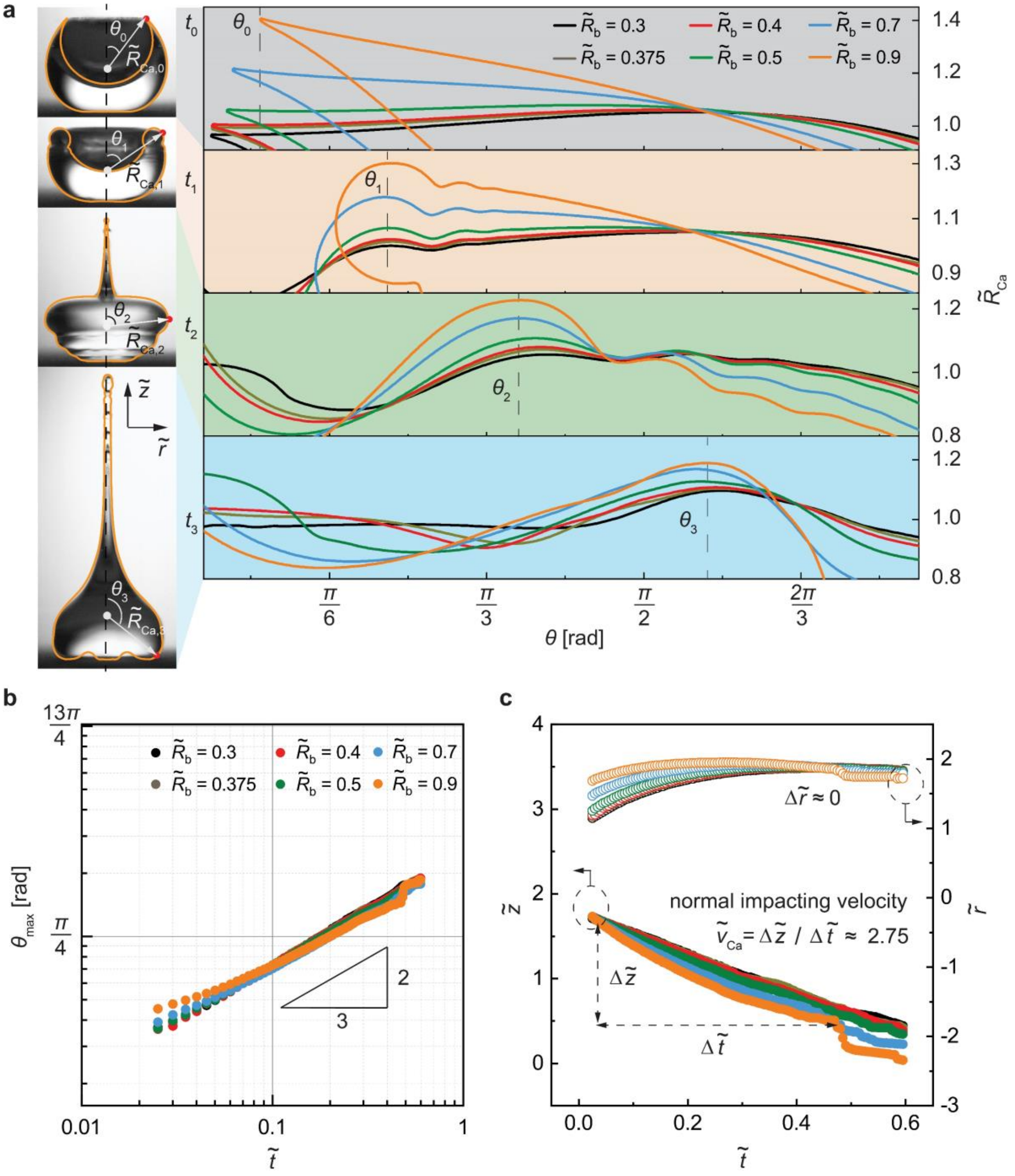

Figure 4-3. Propagation of capillary waves on droplet surface. a (Left panel) Selected snapshots of capillary wave propagation on the droplet surface at various bubble bursting stages of t_0 (initial stage with open cavity), t_1 (early stage with rim retraction), t_2 (middle

stage with jet formation) and t_3 (late stage with capillary wave impact), respectively. The droplet has $Bo = 0.29$ and $\tilde{R}_\mathrm{b} = R_\mathrm{b}/R_\mathrm{d} = 0.9$. The orange profiles were obtained from DNS simulations. The radial distance from the droplet's center of mass to the droplet surface profile is defined as $\tilde{R}_\mathrm{Ca}$. The polar angle relevant to the z-axis is defined as θ. Here θ_0 , θ_1 , θ_2 and θ_3 denote the polar angles of the maximum radial distance $\tilde{R}_\mathrm{Ca,m}$ corresponding to the initial stage, early stage, middle stage and late stage of bubble burst, respectively. a (Right panel) Spatiotemporal evolution of the capillary wave profiles, showing $\tilde{R}_\mathrm{Ca}$ as a function of θ at the corresponding moments of t_0 , t_1 , t_2 and t_3 , respectively. b Temporal evolutions of the polar angle θ_max at the maximum radial distance $\tilde{R}_\mathrm{Ca,m}$ as a function of time $\tilde{t}$. c Temporal evolutions of the vertical displacement $\Delta\tilde{z}$ and radial displacement $\Delta\tilde{r}$ of the point $\left(\theta_\mathrm{max}, \tilde{R}_\mathrm{Ca,m}\right)$ corresponding to the maximum magnitude or peak of capillary waves. The hollow droplets have bubble radii $\tilde{R}_\mathrm{b}$ varying from 0.3 to 0.9.

4.4. Capillary wave propagation

We then analyzed the propagation velocity of the capillary waves incurred by bubble bursting. The spatiotemporal evolutions of the capillary waves are depicted in Fig. 3a by plotting the nondimensionalized droplet center-to-surface distance $\tilde{R}_\mathrm{Ca}$ versus the polar angle θ at certain moments of t_0 (initial stage with open cavity), t_1 (early stage with rim retraction), t_2 (middle stage with jet formation) and t_3 (late stage with capillary wave impacting), respectively. It can be seen that the polar locations of the capillary wave peaks with the maximum magnitudes, denoted by θ_max, traveled to nearly the same position at the subsequent moments of t_1, t_2 and t_3, respectively, regardless of the bubble radii $\tilde{R}_\mathrm{b}$ (Supplementary movie 3). As revealed in Fig. 3b, the propagation of the capillary wave peaks follows $\theta_\mathrm{max} \sim \tilde{t}^{\frac{2}{3}}$, which is abided by inertia-capillary interactions[147, 148]. To characterize the propagation velocity of the capillary waves, we tracked the movement of the wave's peaks (red dots in Fig. 3a) with the corresponding radial and vertical trajectories shown in Fig. 3c. The radial displacement $\Delta\tilde{r}$ approached zero after the initial phase, indicating that the capillary waves impacted nearly vertically towards the substrate surface. For the hollow droplets with the bubble radii $\tilde{R}_\mathrm{b}$ varying from 0.3 to 0.9, the impacting velocities of the capillary waves remained approximately constant at $\tilde{v}_{\mathrm{Ca}} = \Delta\tilde{z}/\Delta\tilde{t} \approx 2.75$. Such consistent impacting velocity of the capillary waves in these cases with different $\tilde{R}_{\mathrm{b}}$ can be explained by the dispersion relation for a droplet undergoing capillary oscillations[149]: $\omega_l^2 = \frac{l(l+2)(l-1)\gamma}{\rho_{\mathrm{d}} {R_0}^3}$, where ω_l is the eigenfrequency, l the oscillation mode, and R_0 the droplet radius (Supplementary Discussion 4). Despite various bubble radii R_{b}, the hollow droplets were observed to oscillate in the similar fashion, i.e., transitioning from a truncated sphere back to a sphere upon bubble burst, inferring the same mode l in their oscillations. Consequently, for hollow droplets of the same initial size $R_0 = R_{\mathrm{d}}$, the oscillations of these droplets exhibited the same angular frequency ω_l and the capillary wave propagation velocity can be scaled as $v_{\mathrm{Ca}} \sim R_{\mathrm{d}} \cdot \omega_l$, which remains constant for the hollow droplets with varying R_{b}.

4.5. Capillary wave impacting and droplet rebound

To elucidate how the impacting capillary waves stimulate droplet jumping, we extracted the pressure field at the droplet base from our DNS simulations as well as the temporal evolutions of its center-of-mass velocity and height, respectively (Supplementary movie 4). It is note-worthy that the pressure distribution at the droplet base confirms the direct and localized capillary waves impact along the droplet perimeter. The normal reaction force F of the droplet is determined by integrating the pressure field at the droplet base [150] $F(t) = \int_A (p_{\mathrm{d}} - p_0) dA$, where p_{d} is the pressure at droplet base, p_0 is the ambient pressure and A is the droplet base area. By nondimensionalizing p_{d} and A with respect to γ/R_{d} and R_{d}^2, respectively, the resulting nondimensionalized normal impacting force $\tilde{F} = \frac{F}{\gamma R_{\mathrm{d}}}$ was obtained as shown in Fig. 4a. A small increase in $\tilde{F}$ was observed when the jet formed at $\tilde{t} \approx 0.085$ and then it quickly decreased back to $\tilde{F} \approx 1.2$, corresponding to the droplet's nondimensional gravitational force $\widetilde{Mg} = \frac{Mg}{\gamma R_{\mathrm{d}}}$, where M represents the droplet mass. Then, $\tilde{F}$ remained nearly unchanged until the arrival of the precursor of capillary wave trains at $\tilde{t} \approx 0.25$, at which point $\tilde{F}$ began to oscillate. The strongest capillary wave impacted on the substrate at $\tilde{t}_{\mathrm{Ca,s}} \approx 0.75$ and persisted until $\tilde{t}_{\mathrm{Ca,e}} \approx 1.085$, at which point $\tilde{F}$ diminished back to the gravity force. This interval was defined as the capillary impacting period of $\Delta\tilde{t}_{\mathrm{Ca}} = 0.335$. Ultimately, $\tilde{F}$ gradually decayed to zero at $\tilde{t} \approx 1.3$, signifying the droplet's out-of-surface jumping.

Figure 4b shows the temporal evolutions of the droplet's center-of-mass velocity $\tilde{v}_{\mathrm{cm}}$ and height $\tilde{h}_{\mathrm{cm}}$, respectively. It is observed that before the strongest capillary impacting at $\tilde{t}_{\mathrm{Ca,s}} \approx 0.75$, both $\tilde{v}_{\mathrm{cm}}$ and $\tilde{h}_{\mathrm{cm}}$ remained relatively stable, indicating that the neither the jet nor the precursor of capillary waves played a major role in the droplet's jumping. It was not until the arrival and impacting of the strongest capillary wave that $\tilde{v}_{\mathrm{cm}}$ started a steep increase. With a net upward force ($\tilde{F} > \widetilde{Mg}$) during the capillary impacting interval $\Delta\tilde{t}_{\mathrm{Ca}}$, $\tilde{v}_{\mathrm{cm}}$ continued increasing until $\tilde{t}_{\mathrm{Ca,e}} \approx 1.085$, after which it began to decrease. Concurrently, $\tilde{h}_{\mathrm{cm}}$ kept on ascending until reaching its apex at $\tilde{t} \approx 1.9$ with all the kinetic energy converted to the potential energy of gravity.

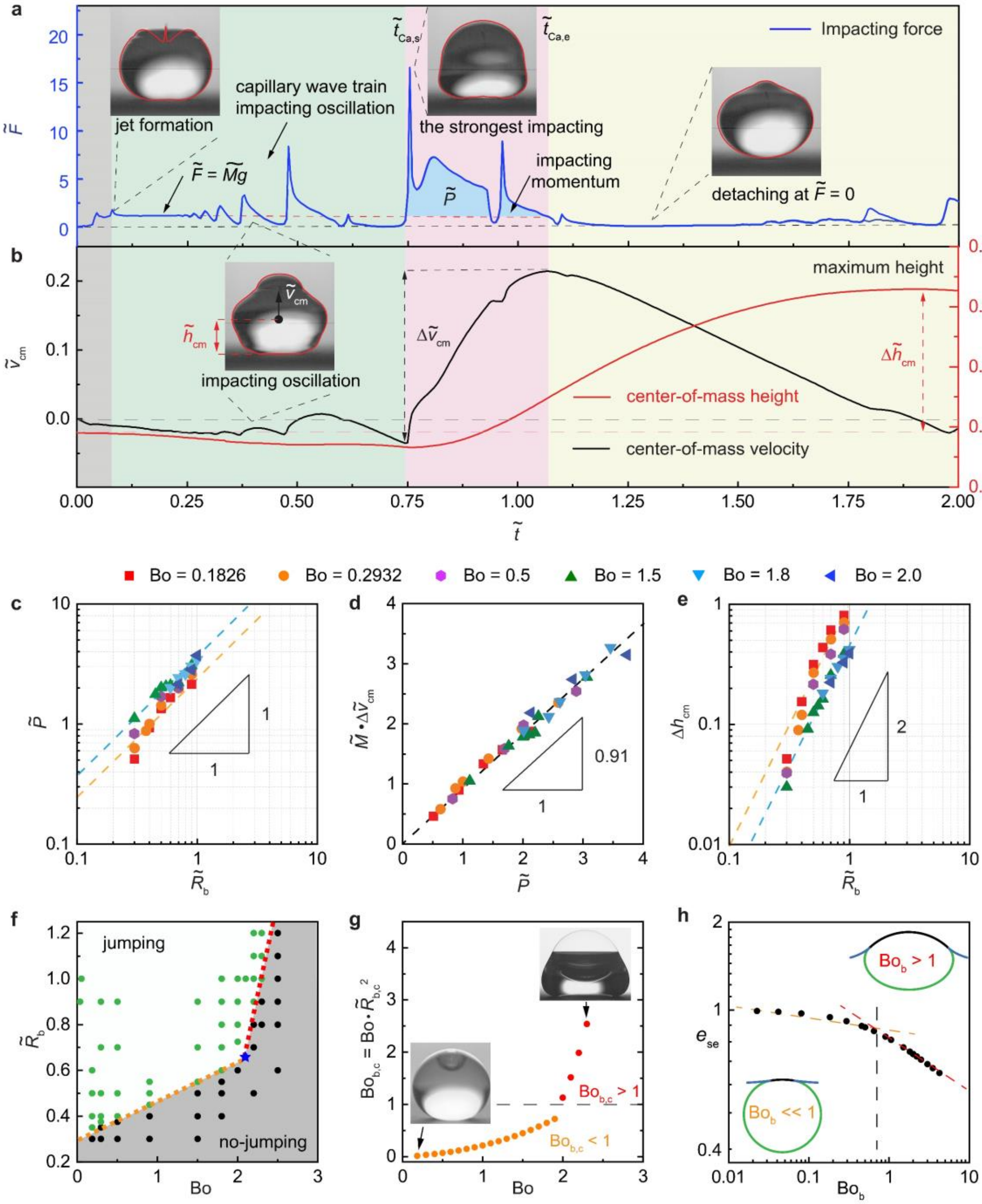

Figure 4-4. Impacting of capillary waves on the substrate and droplet's rebound jumping. **a** Temporal evolution of the impacting force $\tilde{\boldsymbol{F}}$ for a hollow droplet with $\boldsymbol{Bo} = \mathbf{0.29}$ and $\tilde{\boldsymbol{R}}_{\mathbf{b}} = \mathbf{0.4}$. **b** Temporal evolutions of the droplet's center-of-mass velocity $\tilde{\boldsymbol{v}}_{\mathbf{cm}}$ and height $\tilde{\boldsymbol{h}}_{\mathbf{cm}}$ for the same hollow droplet. **c** Plot of the impacting momentum $\tilde{\boldsymbol{P}}$ as a function of $\tilde{\boldsymbol{R}}_{\mathbf{b}}$ over a wide range of Bond numbers from 0.18 to 2.0. **d** Plot of the change in droplet center-of-mass momentum $\tilde{\boldsymbol{M}} \cdot \Delta\tilde{\boldsymbol{v}}_{\mathbf{cm}}$ following the impact of the strongest

capillary wave, versus the impacting momentum $\boldsymbol{\tilde{P}}$. Here $\boldsymbol{\tilde{M}} = \boldsymbol{\tilde{\rho}_{\mathrm{d}}\tilde{V}}$ represents the droplet mass. The dash line has a slope of 0.91. **e** Plot of the maximum rise $\Delta\boldsymbol{\tilde{h}_{\mathrm{cm}}}$ of droplet center-of-mass versus $\boldsymbol{\tilde{R}_{\mathrm{b}}}$. **f** Phase map of hollow droplet jumping behaviors with different droplet $\boldsymbol{Bo}$ and different bubble radius $\boldsymbol{\tilde{R}_{\mathrm{b}}}$. The symbol star stands for the inflection point of the two dashed lines. **g** Plot of the critical bubble Bond number $\boldsymbol{Bo_{\mathrm{b,c}}}$ with different droplet $\boldsymbol{Bo}$. The critical value $\boldsymbol{Bo_{\mathrm{b,c}}} = \boldsymbol{Bo} \cdot \boldsymbol{\tilde{R}^{2}_{\mathrm{b,c}}}$ is calculated from the critical bubble size $\boldsymbol{\tilde{R}_{\mathrm{b,c}}}$, which triggers the out-of-surface jumping of the droplet (collapsing on the orange and red dashed lines in f). **h** Plot of the bubble surface energy efficiency $\boldsymbol{e_{\mathrm{se}}}$ as a function of the bubble Bond number $\boldsymbol{Bo_{\mathrm{b}}}$. The efficiency $\boldsymbol{e_{\mathrm{se}}}$ is calculated as the ratio of the bubble surface area within the droplet (illustrated by the green curve in h) to the total surface area of bubble. The direct and localized impact of capillary waves on the substrate is given in supplementary movie 4.

It becomes evident that the impact of the strongest capillary wave dominates the droplet's jumping behavior. The impact momentum $\tilde{P}$ of the capillary waves is calculated as[137]: $\tilde{P} = \int_{\tilde{t}_{\mathrm{Ca,s}}}^{\tilde{t}_{\mathrm{Ca,e}}} \tilde{F}\, d\tilde{t}$. Notably, it can also be expressed as the product of the capillary wave mass $\tilde{\rho}_{\mathrm{d}}\tilde{\Omega}_{\mathrm{Ca}}$ and the impacting velocity $\tilde{v}_{\mathrm{Ca}}$. As discussed in Eq. (1), the mass of the capillary waves is proportional to the bubble radius, i.e., $\tilde{\rho}_{\mathrm{d}}\tilde{\Omega}_{\mathrm{Ca}} \sim \tilde{R}_{\mathrm{b}}$, while the impacting velocity $\tilde{v}_{\mathrm{Ca}}$ has been shown to be independent of $\tilde{R}_{\mathrm{b}}$. Therefore, the impacting momentum $\tilde{P}$ is predicted to be proportional to the bubble radius $\tilde{R}_{\mathrm{b}}$:

$$\tilde{P} = \tilde{\rho}_{\mathrm{d}}\tilde{\Omega}_{\mathrm{Ca}} \cdot \tilde{v}_{\mathrm{Ca}} \sim \tilde{R}_{\mathrm{b}} \tag{4-2}$$

which is verified by the linear increase of $\tilde{P}$ with $\tilde{R}_{\mathrm{b}}$ in Fig. 4c. Subsequently, the impacting momentum $\tilde{P}$ leads to the change in the momentum of the droplet's center of mass[137]: $\tilde{P} = \tilde{M} \cdot \Delta\tilde{v}_{\mathrm{cm}}$, where $\tilde{M} = \tilde{\rho}_{\mathrm{d}}\tilde{V}$ is the droplet mass and $\Delta\tilde{v}_{\mathrm{cm}}$ is the change of droplet's center of mass velocity caused by the impacting. Strikingly, Fig. 4d manifests the linear relationship between $\tilde{P}$ and $\tilde{M} \cdot \Delta\tilde{v}_{\mathrm{cm}}$ with a slope of 0.91, signifying that approximately 91% of the impacting momentum was efficiently converted into the jumping momentum.

Once the droplet acquired sufficient jumping momentum, it launched off the substrate until reaching its maximum height with the kinetic energy converted into gravitational energy, as described by: $\widetilde{Mg} \cdot \Delta\tilde{h}_{\mathrm{cm}} = \frac{1}{2}\widetilde{M} \cdot (\Delta\tilde{v}_{\mathrm{cm}})^2$. Integrating this relationship with the expression for $\tilde{P}$, the maximum jumping height of the droplet reads:

$$\Delta\tilde{h}_{\mathrm{cm}} \sim \tilde{R}_{\mathrm{b}}^2 \tag{4-3}$$

which is corroborated by the distinct square-law relationship between $\Delta\tilde{h}_{\mathrm{cm}}$ and $\tilde{R}_{\mathrm{b}}$ in Fig. 4e. This square-law relationship can be also obtained through an intuitive energy balance analysis. That is, the surface energy released by the bubble, $\Delta E_{\mathrm{se}} \sim \gamma R_{\mathrm{b}}^2$, is eventually converted into the gravitational energy $Mg\Delta h_{\mathrm{cm}}$, yielding $\Delta h_{\mathrm{cm}} \sim R_{\mathrm{b}}^2$ as derived from our theoretical analysis of Eq. (3).

Explicitly, our mechanistic model predicts that the increasing radius of the injected bubble results in a quadratic rise of the droplet's jumping height. To pin down the critical bubble radius $\tilde{R}_{\mathrm{b,c}}$ necessary for triggering droplet jumping, we plotted the experimental results as a phase map of $\tilde{R}_{\mathrm{b}}$ and Bo in Fig. 4f. The green dots indicate the successful droplet jumping cases while the black dots represent the failure to detach from the surface. The evaluation of these jumping behaviors was mainly based on experimental observations and was quantitatively confirmed by whether the impacting force $\tilde{F}$ in our DNS simulations approaches zero, as discussed in Fig. 4a. As a result, the critical bubble radius $\tilde{R}_{\mathrm{b,c}}$ is determined by the dashed lines (orange and red), demarcating the jumping and no-jumping regions in Fig. 4f. Notably, with $\tilde{R}_{\mathrm{b,c}}$ collapsing onto the two dashed lines, an inflection point as stood by the star in Fig. 4f is evident between them. To explain this infection, we plotted the corresponding Bond number for the critical bubble $Bo_{\mathrm{b,c}} = Bo \cdot \tilde{R}_{\mathrm{b,c}}^2$ versus Bo in Fig. 4g, revealing that the inflection of $\tilde{R}_{\mathrm{b,c}}$ in Fig. 4f corresponds to a transition at $Bo_{\mathrm{b,c}} \approx 1$. Specifically, for $\tilde{R}_{\mathrm{b,c}}$ on the orange dashed line, $Bo_{\mathrm{b,c}} < 1$; for $\tilde{R}_{\mathrm{b,c}}$ on the red dashed line, $Bo_{\mathrm{b,c}} > 1$. Therefore, it is the magnitude of bubble Bond number $Bo_{\mathrm{b}} = \rho_{\mathrm{d}} g R_{\mathrm{b}}^2/\gamma$ that determines the slope and inflection of the boundary lines on the phase map.

In essence, the magnitude of Bo_{b} reflects the relative significance of the buoyant force acting on the bubble, which in turn influences the efficiency of the bubble's surface energy in activating droplet's jumping. When Bo_{b} is small, the buoyant force acting on the bubble is negligible, and thus most of the bubble remains submerged, as depicted by the contour in Fig. 4h (with $Bo_{\mathrm{b}} = 0.08$). This allows for the effective utilization of the majority of the bubble's surface energy for droplet jumping. Conversely, when $Bo_{\mathrm{b}} > 1$, the buoyant force becomes significant, causing a substantial portion of the bubble to float above the droplet surface, as illustrated in Fig. 4h (with $Bo_{\mathrm{b}} = 2.2$). Since only the surface energy associated with the submerged part of the bubble contributes to droplet jumping, the effective energy contribution from the bubble decreases with increasing Bo_{b}. To quantify the effective contribution of the submerged bubble surface, we calculated the ratio (from DNS profiles) of the bubble surface area within the droplet (the green curve in Fig. 4h) to the total bubble surface area, defining this ratio as the surface energy efficiency e_{se}. As shown in Fig. 4h, e_{se} remains a relatively high value (close to 1) when $Bo_{\mathrm{b}} < 1$, but decreases rapidly when $Bo_{\mathrm{b}} > 1$. When e_{se} is high, an even small increase in critical bubble size $\tilde{R}_{\mathrm{b,c}}$ would provide sufficient surface energy to lift a larger droplet, resulting in a gradual slope of the orange dashed line in the phase map of Fig. 4f. Conversely, when e_{se} is low, a more substantial increase in $\tilde{R}_{\mathrm{b,c}}$ is required to lift a larger droplet, leading to a steeper slope of the red dashed line in Fig. 4f.

4.6. Conclusions

By linking and interrelating the two basic fluid dynamic processes, i.e., bubble bursting and droplet actuations on non-wetting surfaces, this study reveals a previously unexplored mechanism of bubble burst-induced droplet jumping, which remarkably expands the size spectrum of self-propelled droplets from mm scale to cm scale. In particular, a mechanistic framework is established for the roles of capillary wave impacting in dominating the puddle droplet jumping process, which is supported by experiments and numerical simulations, with the derived scaling laws valid even for $Bo > 2.0$. By pinpointing the roles of capillary wave impacting in fluid-solid interactions, this study points to a new avenue for fluid actuation and control, with potential applications in particle enrichment, remote dispersion and transport.

Chapter 5

Summary of Contribution

This dissertation advances the understanding of droplet-substrate interactions through a detailed investigation of processes spanning droplet evaporation, Leidenfrost-like droplet jumping, and bubble burst-induced droplet actuation.

In Chapter 2, the evaporation dynamics of sessile water droplets on micro-pillared superhydrophobic surfaces were comprehensively studied at moderate temperatures (40 °C–120 °C). The evaporation rates from both the droplet cap and the interstitial liquid-vapor interface at the droplet base were systematically analyzed, providing new insights into the distinct contributions of these components. A thermal circuit model was developed to predict evaporation rates and cap temperatures across different evaporation modes. The model revealed that in the constant contact radius (CCR) mode, the evaporation rate decrease is primarily driven by the droplet base, whereas in the constant contact angle (CCA) mode, the droplet cap dominates this decline. An effective thermal conductivity correction factor was introduced to account for internal fluid motion on high-temperature substrates, enabling accurate predictions of evaporation dynamics and elucidating temperature differences between the droplet base and the substrate surface. This work offers a robust framework for understanding and controlling droplet evaporation on microstructured surfaces.

In Chapter 3, the phenomenon of Leidenfrost-like droplet jumping on micropillared surfaces at relatively low temperatures was explored. Droplet levitation and rapid self-propelled jumping were achieved at temperatures as low as 130 °C, significantly below the traditional Leidenfrost threshold of 230 °C. This behavior was attributed to inertia-controlled vapor bubble growth at the droplet base, modulated by the thermal boundary layer thickness through pillar height adjustments. The distinct bubble growth modes—heat-transfer-limited and inertia-controlled—were shown to dictate jumping behaviors, characterized by constant velocity and constant energy regimes, respectively. This work highlights a novel approach for the rapid and controlled removal of wetting liquids from rough surfaces, with applications in anti-fouling and heat transfer systems.

In Chapter 4, the integration of bubble bursting and droplet dynamics revealed a previously unexplored mechanism of bubble burst-induced droplet jumping. This mechanism overcomes the theoretical capillary length limitation, enabling the out-of-surface jumping of water droplets with diameters in the centimeter scale. The synergistic effects of upward jet generation and capillary wave propagation were demonstrated to provide efficient momentum transfer for droplet jumping. Experiments and numerical simulations established a mechanistic framework, identifying the dominant role of capillary wave impacts in facilitating the process. The derived scaling laws, valid for Bond numbers exceeding 2, expand the size spectrum for droplet jumping and offer new perspectives on fluid-solid interactions. This mechanism opens avenues for fluid actuation and control, with potential applications in particle enrichment, dispersion, and transport.

Collectively, this dissertation contributes to the broader understanding of droplet behaviors and their governing mechanisms, providing practical insights and tools for applications ranging from thermal management to surface engineering and beyond.

Building on the findings of this dissertation, several promising directions emerge for future exploration. The Leidenfrost-like droplet jumping mechanism demonstrated here, which required pre-depositing droplets on cold surfaces before transferring them to a heated substrate, could be extended to more practical contexts. For instance, lightly textured superhydrophobic surfaces preheated to superheated states could enable self-propulsion of jets or spray droplets, making this mechanism applicable to dynamic systems like spray cooling or droplet-impact processes in industrial heat exchangers. Additionally, the bubble burst-induced droplet jumping mechanism could inspire novel studies in confined systems, such as microchannels or porous media, where bubble-induced fluid dynamics may be leveraged for fluid transport, mixing, or particle manipulation, with potential applications in lab-on-chip technologies or targeted drug delivery. Further, tailoring surface microstructures or incorporating responsive materials could enable tunable droplet behaviors, optimizing evaporation and jumping processes for thermal management or anti-fouling applications. Advanced numerical simulations, coupled with experimental investigations, could offer deeper insights into the interplay between capillary waves, jet formation, and droplet dynamics under varying fluid properties, surface geometries, or environmental conditions. Lastly, translating these mechanisms into practical devices or industrial systems, such as for enhanced cooling efficiency, controlled droplet transport, or rapid liquid removal, presents an exciting opportunity to bridge fundamental discoveries with real-world applications.

Appendix

Appendix A: Supporting Information for Chapter 2

S1. Droplet evaporation rate on sample 2 and sample 3

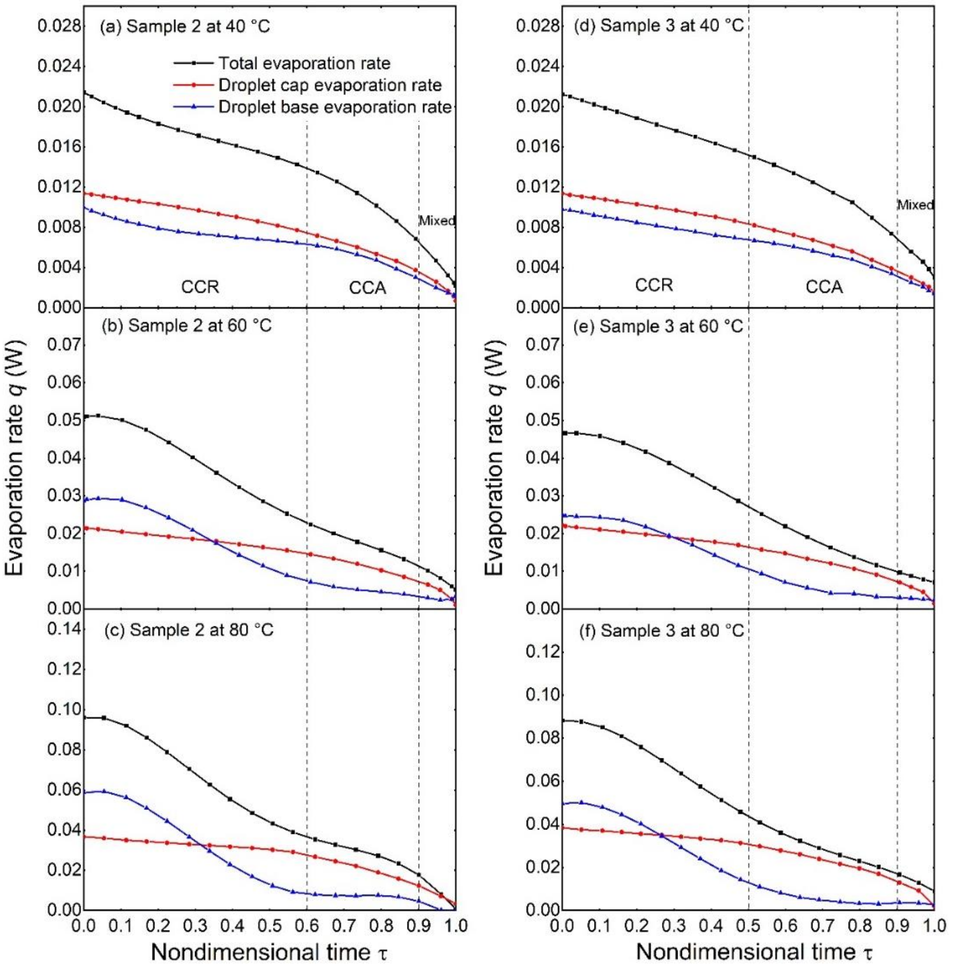

Figure A-1. Total evaporation rate, droplet cap surface evaporation rate and droplet base evaporation rate on sample 2 with (a) 40 °C substrate base temperature, (b) 60 °C substrate base temperature and (c) 80 °C substrate base temperature. Total evaporation rate, droplet cap surface evaporation rate and droplet base evaporation rate on sample 3 with (d) 40 °C substrate base temperature, (e) 60 °C substrate base temperature and (f) 80 °C substrate base temperature

S2. IR camera calibration.

The IR camera FLIR A655sc (The camera has an IR resolution of 640 pixels × 480 pixels and the spectral range of the camera is 7.5 – 14.0 μm) was calibrated before testing the surface temperature of the droplet.

Water in a beaker was heated up to the boiling point (about 100°C under 1 atmosphere pressure). The water-air interface temperature was measure by the IR camera and a K-type thermocouple simultaneously. The water emissivity is set as 0.99 and the comparison of the measuring results of the IR camera and the thermocouple is shown in Fig. S2.

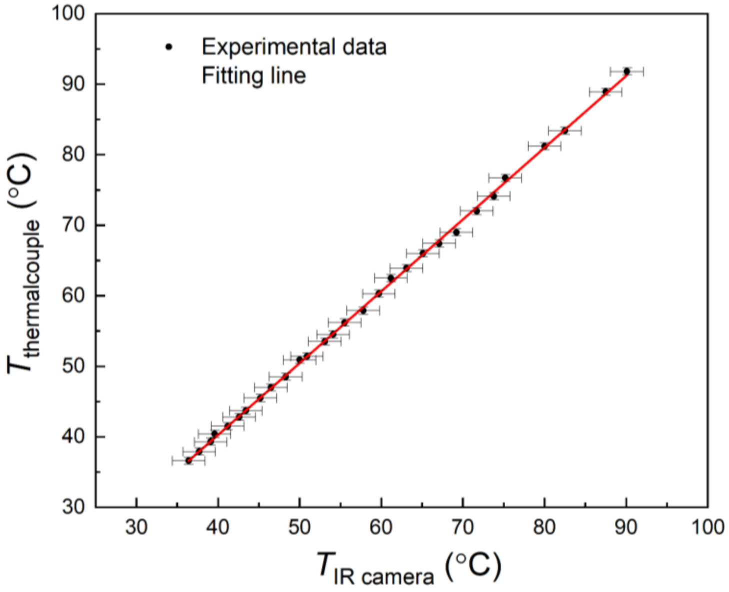

Figure A-2. Comparison of thermocouple and IR camera temperature measurement**.**

The equation of the fitting line is:

$$T_{\text{thermal couple}} = 1.02 \times T_{\text{IR camera}} - 0.46(°\text{C}) \qquad \text{(A-1)}$$

S3. Curvature surface temperature measurement correction.

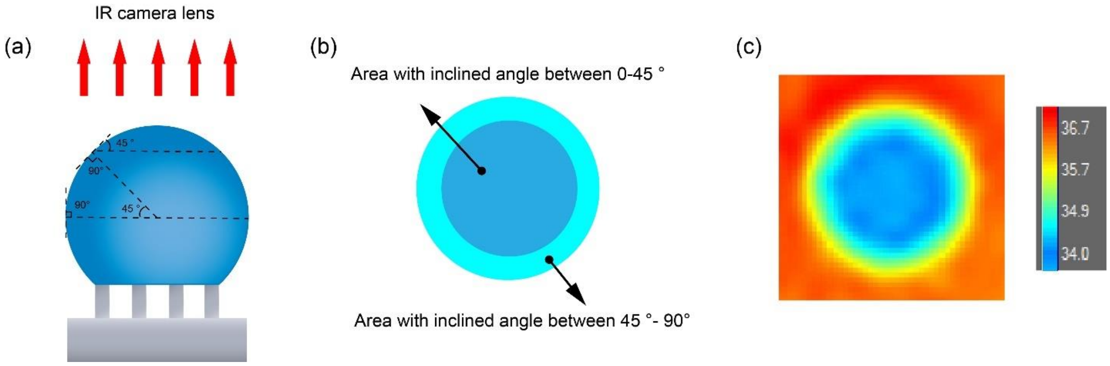

Figure A-3. Droplet surface temperature with IR camera (a) Side view of droplet cap surface for droplet evaporation on the micro-structured substrate. (b) Top view of droplet cap surface for droplet evaporation on the micro-structured substrate. (c) Top view IR thermography of droplet cap surface.

Because of the small diameters (below the capillary length) of the droplets tested in this study and the superhydrophobicity of the micro-structured substrates, the droplet resting on the substrate shows a large contact angle and the surface of the droplet forms spherical cap shape. The curvature of the surface would cause less radiation to be absorbed by the IR camera and cause a reduction of the measured surface temperature. Also, the relative high temperature of the silicon substrate background would at the same time caused a temperature rise of the measuring surface temperature. It is necessary to make correction to the temperature measurement.

Mentioned by F. Carle[151] that “for droplets with contact angles below 40° the influence on the reflectivity due to the angle of visualization between the IR camera and the droplet interface can be neglected”. Also, in the previous study of D.J. Watmough et al [152]. they concluded that the temperature reduction caused by the surface curvature can generally be neglected for surface with inclined angle less then 45°. In this study, we used the IR camera to measure the temperature of the upper hemispherical surface of the droplet, which contains inclined angle ranging from 0° to 90° as shown in Fig. S3 (a). We divided the upper hemispherical surface of the droplet into two parts: area with inclined angle between 0°- 45° and area with inclined angle between 45°-90° as shown in Fig. S3 (b). Surface temperature of the first part measured by the IR camera can be assumed to be real since the effects of the surface curvature are neglectable. And we need to correct the surface temperature in the second part with large inclined angle. The emissivity and reflectivity of the water cap surface can be calculated with the refraction index *n* and absorption coefficient *k* of water and air[153]. The reflectivity on a curved surface can be divided as parallel and normal refractilities[154]:

$$\rho_p = \frac{(n_1 cos\beta - u)^2 + v^2}{(n_1 cos\beta + u)^2 + v^2} \tag{A-2}$$

$$\rho_n = \frac{\left((n_2^2 - k_2^2)cos\beta - n_1 u\right)^2 + (2n_2 k_2 cos\beta - n_1 v)^2}{\left((n_2^2 - k_2^2)cos\beta + n_1 u\right)^2 + (2n_2 k_2 cos\beta + n_1 v)^2} \tag{A-3}$$

where ρ_p and ρ_n donate the parallel and normal refractilities. u, v and β are three intermediate quantities and can be expressed as:

$$u^2 = \frac{1}{2}(n_2^2 - k_2^2 - n_1^2 sin^2\beta) + \frac{1}{2}\sqrt{(n_2^2 - k_2^2 - n_1^2 sin^2\beta)^2 + 4n_2^2 k_2^2} \tag{A-4}$$

$$v^2 = -\frac{1}{2}(n_2^2 - k_2^2 - n_1^2 sin^2\beta) + \frac{1}{2}\sqrt{(n_2^2 - k_2^2 - n_1^2 sin^2\beta)^2 + 4n_2^2 k_2^2} \tag{A-5}$$

$$\beta = cos^{-1}\left(\frac{cos^{-1}(r + bcos\theta)}{sin\theta cos\varphi\sqrt{r^2 + b^2 sin^2\theta}}\right) \tag{A-6}$$

where θ and φ are the polar angle and azimuthal angle of point on the droplet cap surface. *r* and *b* are the radial position and height position of the droplet, respectively.

Using the equation presented by A. Chandramohan et al.[155] the curved surface temperature can be corrected by the local surface reflectivity:

$$\rho_r = \frac{\rho_p + \rho_n}{2} \tag{A-7}$$

$$0.97\sigma T_0^4 = \varepsilon_1 \sigma T_1^4 + \rho_r \varepsilon_2 \sigma T_2^4 \tag{A-8}$$

where ρ_r is the surface reflection, ε_1 is the water emissivity, ε_2 is the background emissivity, σ is the Stefan-Boltzmann constant, T_0, T_1 and T_2 are the surface temperature before correction, surface temperature after correction and the background temperature.

We calculated the average temperature of the upper hemispherical cap surface of the droplet for comparison with the prediction surface temperature of the thermal circuit model.

$$T_{ave} = \frac{\int_0^{\frac{\pi}{2}} 2\pi r^2 T_1 sin\theta d\theta}{2\pi r^2} = \int_0^{\frac{\pi}{2}} T_1 sin\theta d\theta \tag{A-9}$$

S4. Microscope images of substrate used in this study.

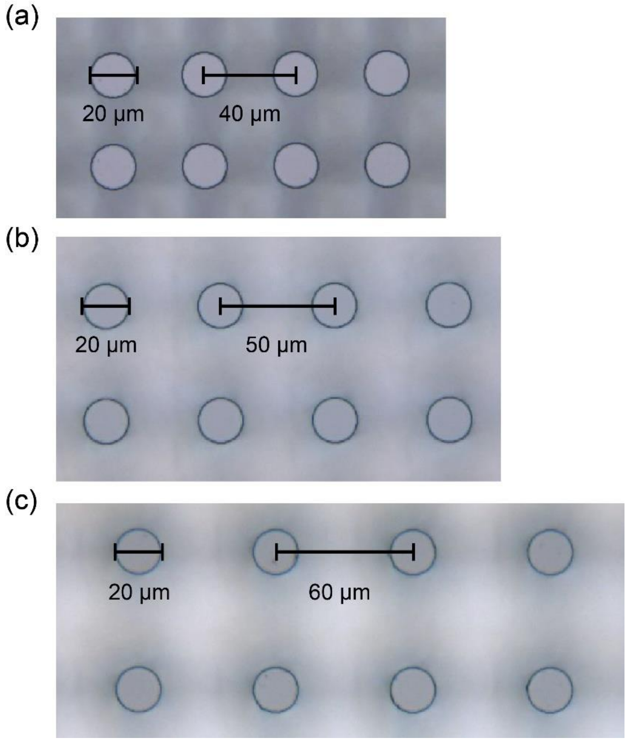

Figure A-4. Microscope images of substrate used in this study. (a) sample1, (b) sample2 and (c) sample3.

Appendix B: Supporting Information for Chapter 3

Supplementary Figures

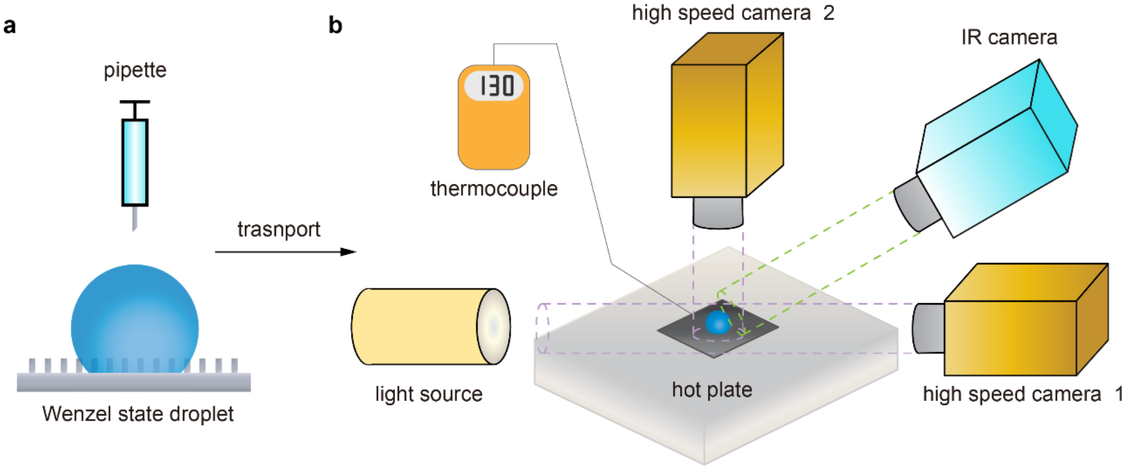

Figure B-1. Experimental setup for the Leidenfrost-like droplet jumping study. a A water droplet is initially deposited on the micropillared substrate in Wenzel state and then both the droplet and the substrate are carefully translated to a hot plate preheated at 130 °C. **b** Experimental setup for droplet jumping observation. The temperature of the substrate is measured by a K-type thermocouple embedded in the hot plate underneath the substrate. Surface temperature of the droplet is monitored by an IR camera (FLIR A655sc) after moving the substrate on the hot plate. The vibration and jumping processes of the boiling droplet are recorded by a side view high-speed camera (nac MEMRECAM HX-3) and the vapor bubble growth process is monitored by another high-speed camera from the top (Photron FASTCAM SA-6).

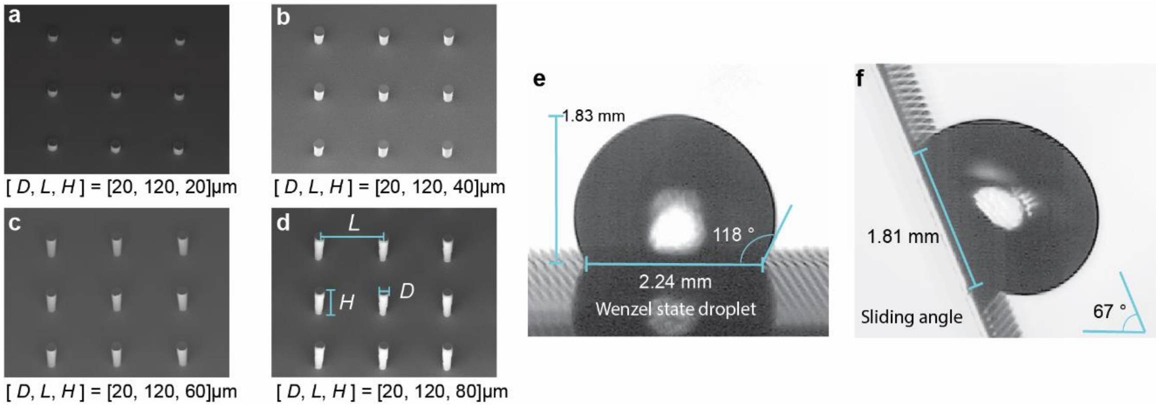

[D, L, H] = [20, 120, 20]μm

[D, L, H] = [20, 120, 40]μm

[D, L, H] = [20, 120, 60]μm

[D, L, H] = [20, 120, 80]μm

Figure B-2. Substrate topology details of the engineered surfaces used in this study. a The scanning electron micrography (SEM) of substrate $[\boldsymbol{D},\ \boldsymbol{L},\ \boldsymbol{H}] = [\mathbf{20}, \mathbf{120}, \mathbf{20}]\boldsymbol{\mu}\mathbf{m}$. **b** SEM image of substrate $[\boldsymbol{D},\ \boldsymbol{L},\ \boldsymbol{H}] = [\mathbf{20}, \mathbf{120}, \mathbf{40}]\boldsymbol{\mu}\mathbf{m}$. **c** SEM image of substrate $[\boldsymbol{D},\ \boldsymbol{L},\ \boldsymbol{H}] = [\mathbf{20}, \mathbf{120}, \mathbf{60}]\boldsymbol{\mu}\mathbf{m}$. **d** SEM image of substrate $[\boldsymbol{D},\ \boldsymbol{L},\ \boldsymbol{H}] = [\mathbf{20}, \mathbf{120}, \mathbf{80}]\boldsymbol{\mu}\mathbf{m}$. **e** Wenzel state droplet on substrate $[\boldsymbol{D},\ \boldsymbol{L},\ \boldsymbol{H}] = [\mathbf{20}, \mathbf{120}, \mathbf{80}]\boldsymbol{\mu}\mathbf{m}$ at room temperature. The height of the sessile droplet is 1.83 mm; the contact diameter of the droplet is 2.24 mm; the contact angle of the droplet is 118°. **f** Sliding angle of the droplet on the substrate $[\boldsymbol{D},\ \boldsymbol{L},\ \boldsymbol{H}] = [\mathbf{20}, \mathbf{120}, \mathbf{80}]\boldsymbol{\mu}\mathbf{m}$ at room temperature is 67°.

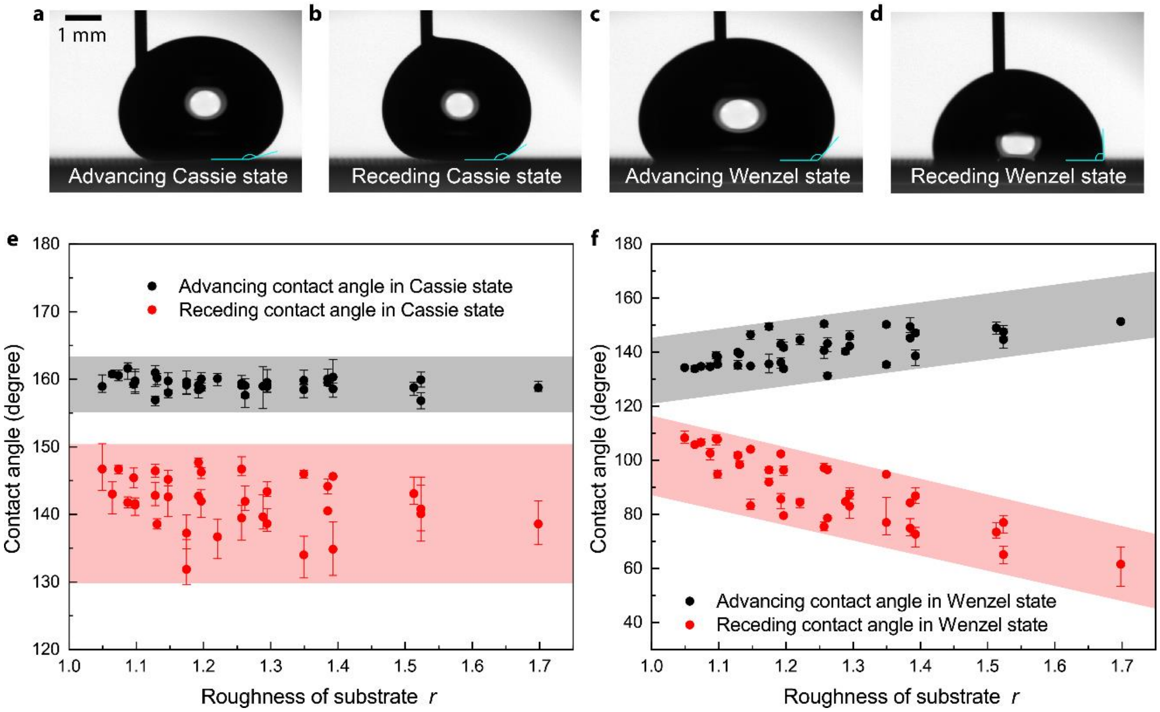

Figure B-3. Droplet contact angles on the engineered substrates. **a** Schematic of advancing contact angle (ACA) measurement in Cassie state on the micropillared substrate $[\boldsymbol{D},\ \boldsymbol{L},\ \boldsymbol{H}] = [\mathbf{20}, \mathbf{120}, \mathbf{20}]\boldsymbol{\mu}\mathbf{m}$. **b** Schematic of receding contact angle (RCA) measurement in Cassie state on the micropillared substrate $[\boldsymbol{D},\ \boldsymbol{L},\ \boldsymbol{H}] = [\mathbf{20}, \mathbf{120}, \mathbf{20}]\boldsymbol{\mu}\mathbf{m}$. **c** Schematic of advancing contact angle measurement in Wenzel state on the micropillared substrate $[\boldsymbol{D},\ \boldsymbol{L},\ \boldsymbol{H}] = [\mathbf{20}, \mathbf{120}, \mathbf{20}]\boldsymbol{\mu}\mathbf{m}$. **d** Schematic of receding contact angle measurement in Wenzel state on the micropillared substrate $[\boldsymbol{D},\ \boldsymbol{L},\ \boldsymbol{H}] = [\mathbf{20}, \mathbf{120}, \mathbf{20}]\boldsymbol{\mu}\mathbf{m}$. **e** Relationship between the substrate roughness $\boldsymbol{r}$ and the ACA/RCA of droplets in the Cassie state. **f** Relationship between the substrate roughness $\boldsymbol{r}$ and the ACA/RCA of droplets in the Wenzel state.

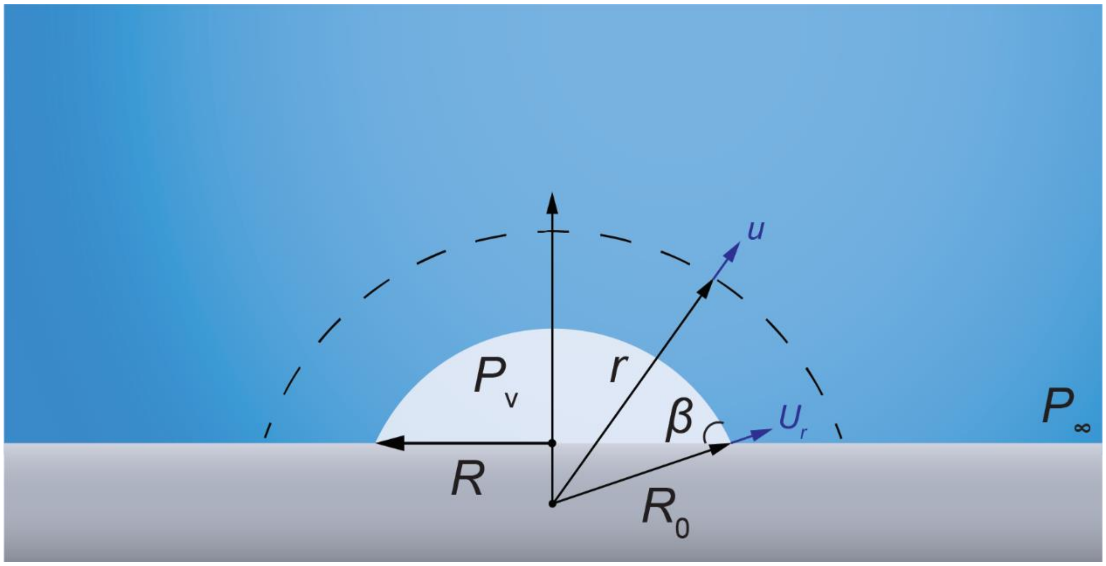

Figure B-4. Diagram of vapor bubble expansion via momentum interaction with the surrounding liquid at the droplet base.

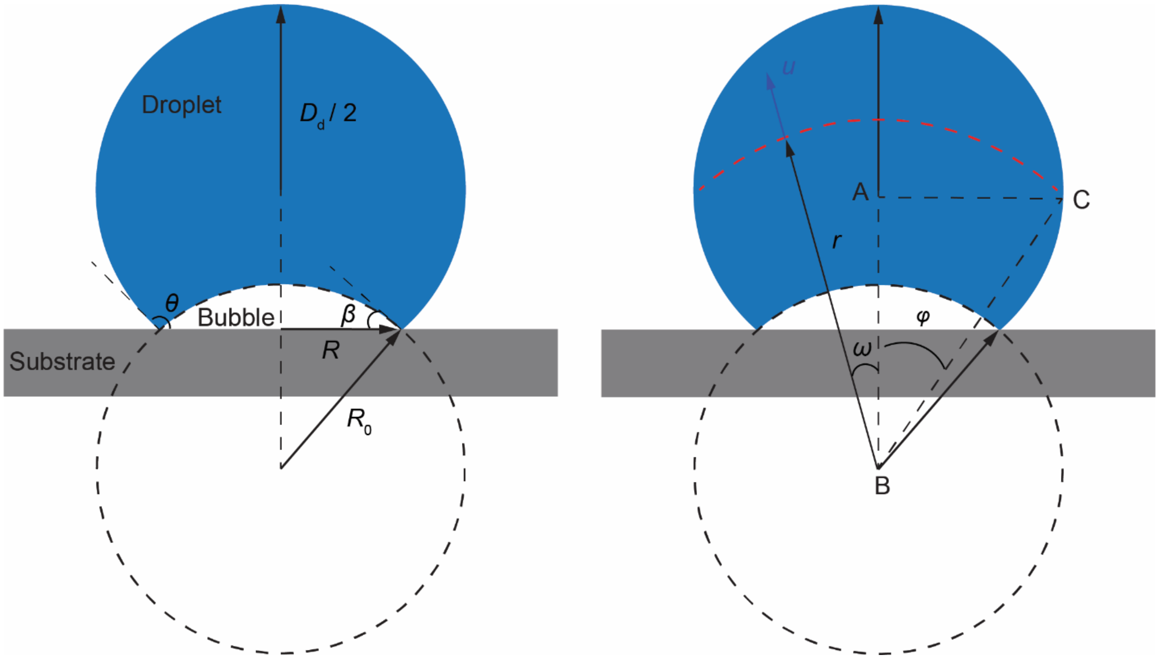

Figure B-5. Diagram of bubble-droplet geometry when the droplet is about to jump off the substrate.

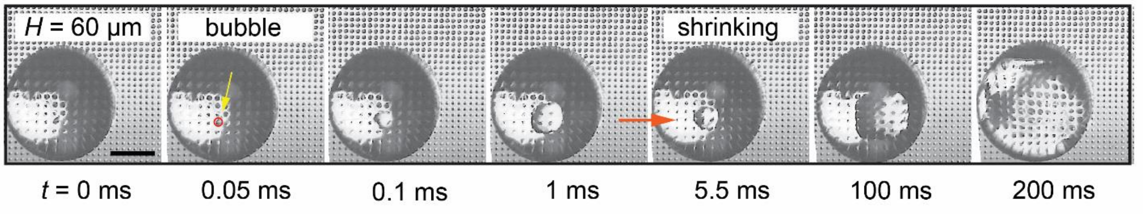

Figure B-6. Top-view snapshots of vapor bubble growth on substrate $[\boldsymbol{D},\ \boldsymbol{L},\ \boldsymbol{H}] = [\mathbf{20}, \mathbf{120}, \mathbf{60}]$ μm at 130 °C.

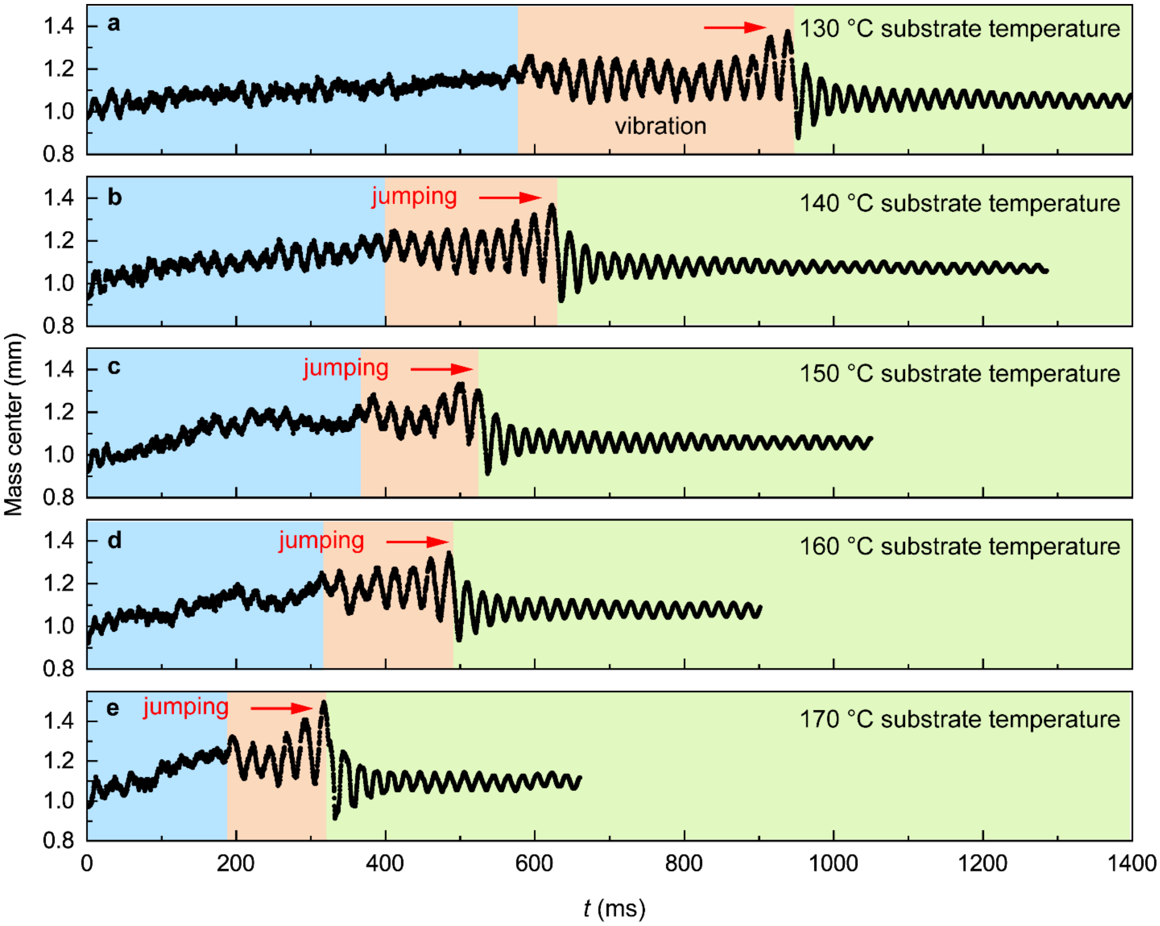

Figure B-7. Droplet mass center variation on the hot substrate $[\boldsymbol{D},\ \boldsymbol{L},\ \boldsymbol{H}] = [\mathbf{20}, \mathbf{120}, \mathbf{20}]$μm at different temperatures. a Droplet height variation on substrate at 130 °C. **b** Droplet height variation on substrate at 140 °C. **c** Droplet height variation on substrate at 150 °C. **d** Droplet height variation on substrate at 160 °C. **e** Droplet height variation on substrate at 170 °C.

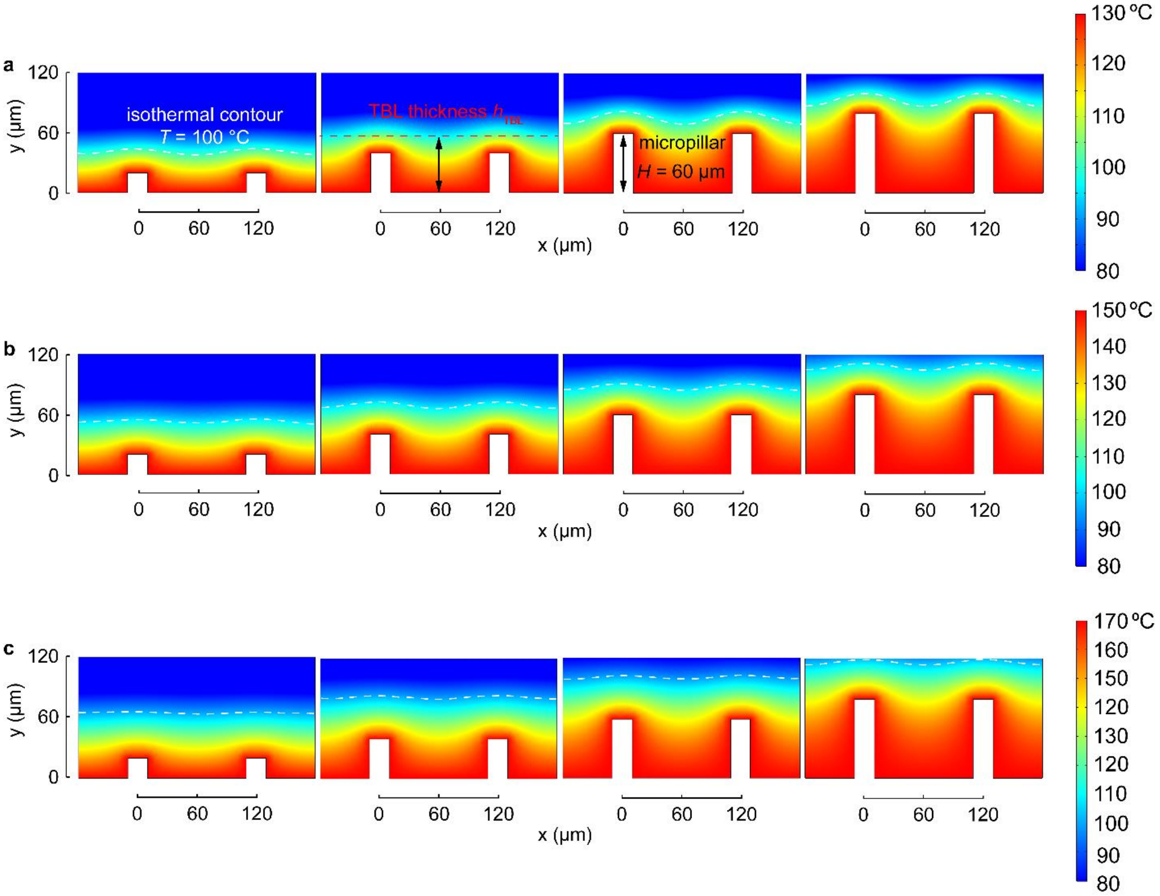

Figure B-8. Simulated temperature distribution of quiescent TBL on the substrates with micropillar height ranging from $\mathbf{20\ \mu m}$ to $\mathbf{80\ \mu m}$. a Simulated TBL on substrates at 130 °C. **b** Simulated TBL on substrates at 150 °C. **c** Simulated TBL on substrates at 170 °C. The isothermal contour of 100 °C is donated by the white dash line. The thickness of TBL is defined as $\boldsymbol{h}_{\mathbf{TBL}} = \frac{\boldsymbol{V}_{\mathbf{sup}}}{\boldsymbol{L}_{\mathbf{p}}}$, where $\boldsymbol{V}_{\mathbf{sup}}$ corresponds to the total volume of superheated liquid and $\boldsymbol{L}_{\mathbf{p}}$ is the projected length of the computational domain.

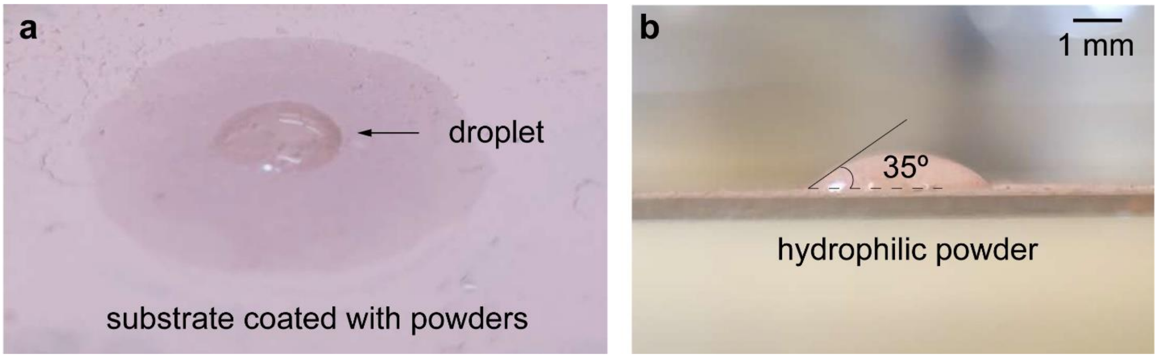

Figure B-9. Hydrophilic powder particles. a Coating of prism polishing powder particles (Cerium Oxide Polishing Powder 1306-38-3) on a substrate. **b** Contact angle of water droplet on the prism powder surface.

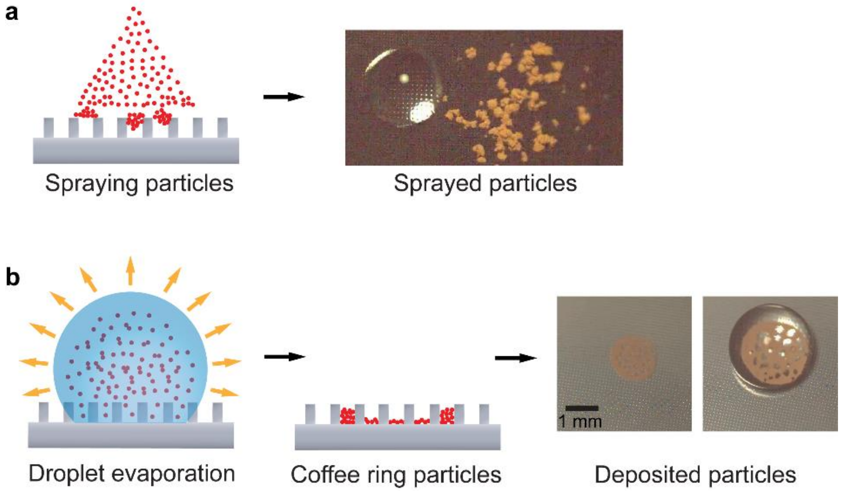

Figure B-10. Deposition of prism powder particles on the micropillared substate. a Sprayed particles on a substrate. **b** Deposition of particles on a substrate via evaporation-assisted coffee ring effect. Right panels are experimental results.

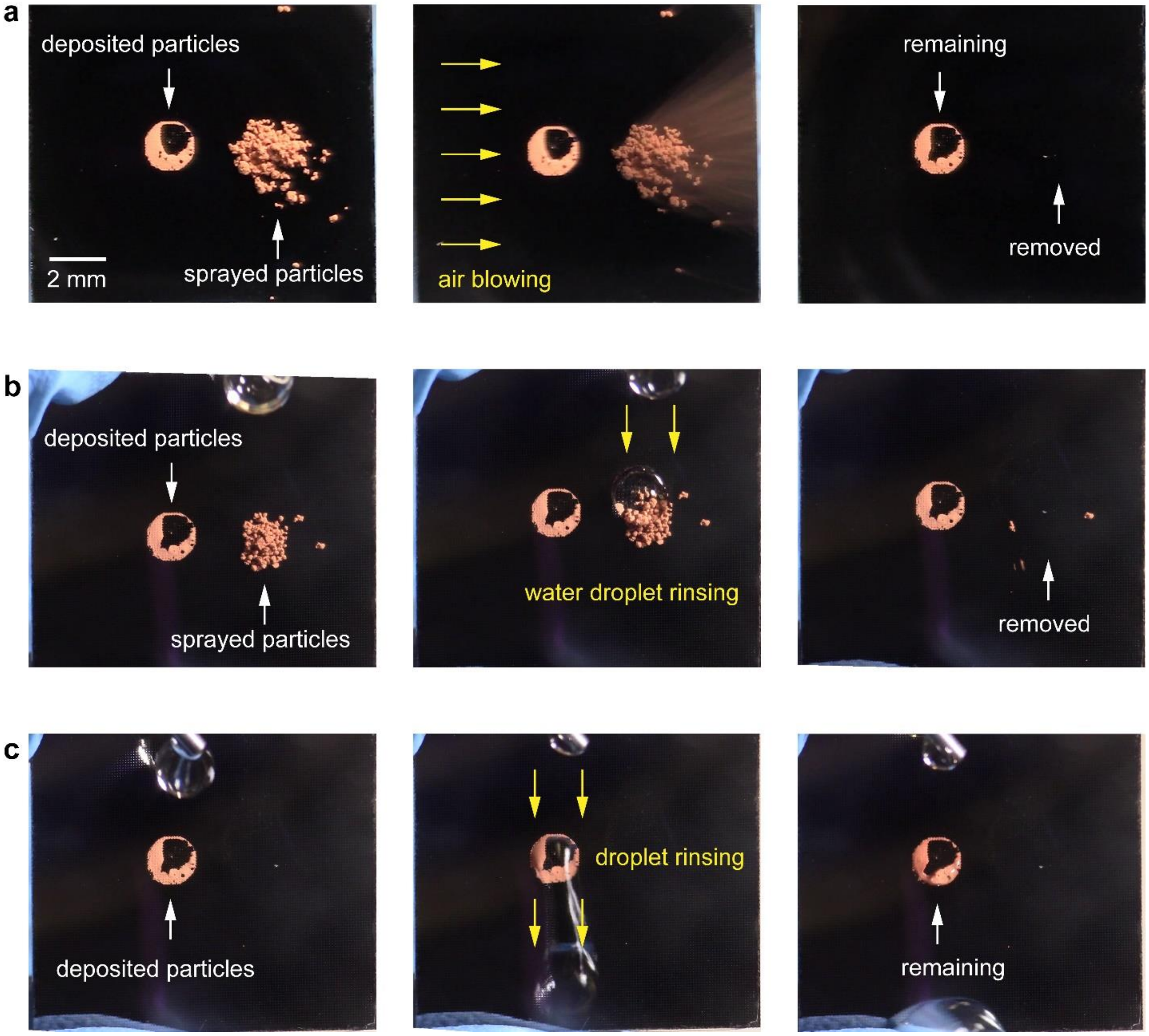

Figure B-11. Purging of powder particles on the substrate $[\boldsymbol{D},\ \boldsymbol{L},\ \boldsymbol{H}] = [\mathbf{20}, \mathbf{120}, \mathbf{20}]\,\boldsymbol{\mu}\mathbf{m}$. a Particles sprayed on the substrate can be easily blown away. However, deposited particles via droplet evaporation, *i.e.*, coffee ring effect, cannot be easily removed by gas blowing. **b** Particles sprayed on the substrate can be easily removed by water droplet rinsing, *i.e.*, lotus effect. **c** Particles deposited via droplet evaporation cannot be easily removed by water droplet rinsing.

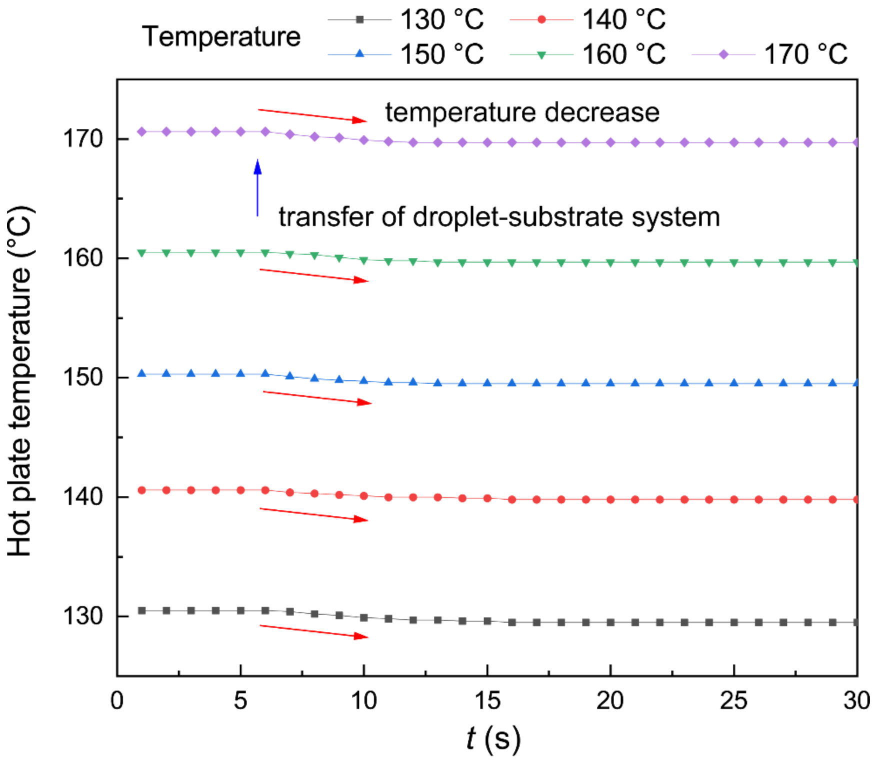

Figure B-12. Surface temperature evolution of the hot plate before and after the transfer of droplet-substrate system. Along with the transfer of the droplet-substrate system, the hot plate temperature is continuously monitored by a K-type thermocouple embedded in the hot plate. The thermocouple is positioned in a carved channel which is about 0.5 mm below the 2 cm by 2 cm substrate. The blue arrow indicates the anchoring moment of the droplet-substrate system on the hot plate.

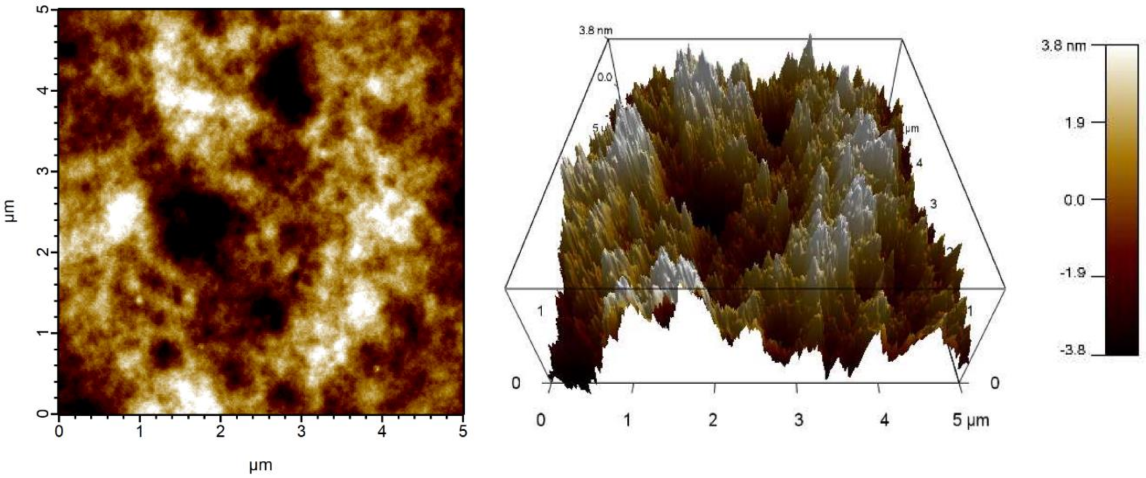

Figure B-13. Surface morphology of a substrate coated with fluoropolymer. The surface roughness was measured by an atomic force microscopy (Asylum Jupiter XR).

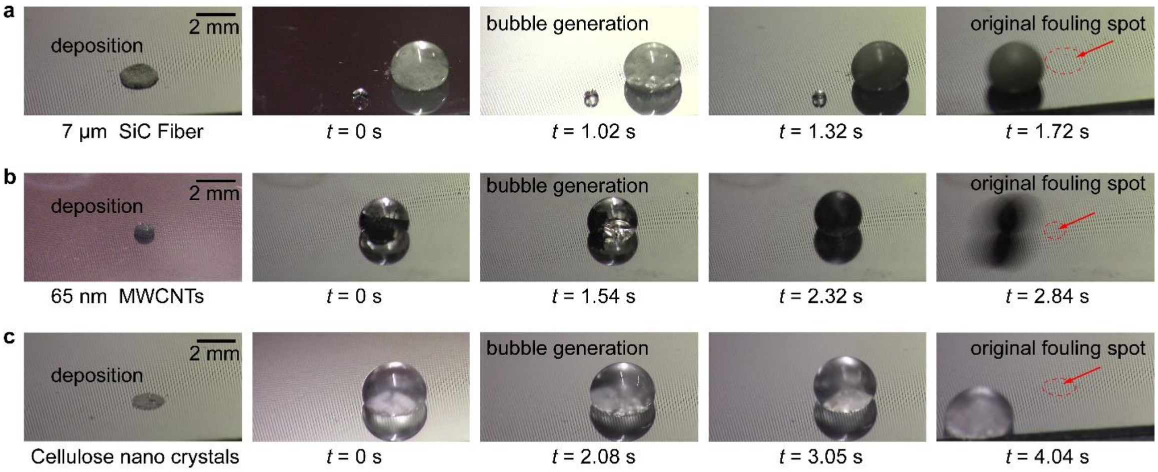

Figure B-14. Experimental snapshots of dislodging and removal of various types of fouling from surface roughness by sliding water droplet on the tilted substrate $[\boldsymbol{D},\ \boldsymbol{L},\ \boldsymbol{H}] = [\mathbf{20}, \mathbf{120}, \mathbf{20}]$ μm at 130 °C. a SF-7 7**μm** SiC Fiber (SI-TUFF). **b** 50 – 80 nm MWCNTs (US Research Nanomaterials). **c** Cellulose nano crystals (CelluForce).

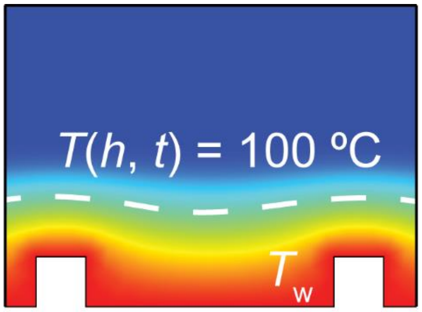

Figure B-15. Diagram of thermal boundary layer propagation over the micropillared surface.

Supplementary Discussion 1: Contact angle on microstructured substrates

It can be seen in Fig. S2e that, for droplets in Cassie state, both the advancing contact angle (ACA) and the receding contact angle (RCA) are almost independent of the substrate roughness. In this study, the increase of the substrate roughness $r = \frac{L^2+\pi DH}{L^2}$ is mainly caused by the increase of the micropillar height H. The Cassie state droplet resides only on the tips of the micropillars and as a result, the increase of the substrate roughness r has no obvious influence on the Cassie state droplet's ACA and RCA.

However, it is observed in Fig. S2f that the ACA of droplet in Wenzel state increases with the increase of the substrate roughness and the RCA of the droplet in Wenzel state decreases with the increase of the substrate roughness. The increase of the micropillar height (increase of the substrate roughness) leads to the increase of the adhesion between the Wenzel state droplet and the substrate. Thus, it requires a larger ACA or a smaller RCA to generate a sufficient depinning force to actuate the pinned droplet.

ACA and RCA of droplets in both Cassie state and Wenzel state have been measured and are listed in Supplementary Table 1. To measure the ACA, the droplet was deposited on the substrate with a syringe needle inserted in to the droplet body from the top. Water was slowly and steadily pumped into the droplet to gradually increase the droplet volume. Simultaneously, the droplet's contact angle continuously increased while its contact line kept pinned. The transient contact angle was recorded as the ACA when the initially pinned contact line started to move. The opposite was done to measure the RCA: water liquid was pumped out from the droplet and the transient contact angle was recorded as the RCA when the droplet's contact line started to shrink. It is noteworthy that the RCA usually depends on the size of the droplet. The measured RCA might not be accurate when the sessile droplet volume is too small. Korhonen *et al.*[156] proposed a reasonable lower limit of 5 µL for the droplet volume in order to measure a reliable RCA of a sessile water droplet. Thus, in this study, all the RCAs were measured with droplet volume larger than 5 µL.

Supplementary Discussion 2: Rayleigh-Plesset equation

As demonstrated in Fig. S4, U_r is the radial velocity of the expanding bubble interface with spherical radius R_0. Considering the radial waterflow around the vapor bubble that follows the continuity equation $\frac{\partial r^2 u}{\partial r} = 0$, the radial waterflow velocity u at arbitrary coordinate r in the liquid domain can be calculated as $u = U_r \frac{R_0^2}{r^2}$. Then the kinetic energy of the water domain caused by the expansion bubble can be calculated as:

$$KE = \frac{1}{2}\rho_\mathrm{l} \int_{R_0}^{R_d} u^2 \cdot 2\pi r^2 (1 - \cos\beta) dr \tag{B-1}$$

where R_d is the radius of the droplet and we consider the bubble size is much smaller than the droplet size $R_d \gg R_0$.

The vaporization-induced bubble overpressure drives the receding of the surrounding liquid. The net work done against the surrounding liquid as the bubble grows from $r = 0$ to R_0 is given by:

$$W = \int_0^{R_0} \left(P_v - P_\infty - \frac{2\sigma}{r}\right)\left(2\pi r^2 (1 - \cos\beta)\right) dr \tag{B-2}$$

The energy stored inside the vapor bubble with overpressure is then converted into the kinetic energy of the water droplet, so we have $KE = W$. Thus, we obtain:

$$(1 - \cos\beta)\pi\rho_\mathrm{l}\left(\frac{dR_0}{dt}\right)^2 R_0^3 = \left(P_v - P_\infty - \frac{2\sigma}{R}\right) 2\pi(1 - \cos\beta)\frac{R_0^3}{3} \tag{B-3}$$

Then differentiating the entire equation with respect to R_0, the Rayleigh-Plesset equation is obtained:

$$\rho_\mathrm{l} R_0 \ddot{R}_0 + \rho_\mathrm{l}\frac{3\dot{R}_0^2}{2} = \left(P_v - P_\infty - \frac{2\sigma}{R}\right) \tag{B-4}$$

Assuming the constant contact angle β during the bubble expanding process, we can express the bubble contact radius as $R = R_0 \sin\beta$. As a result, the Rayleigh-Plesset equation with respect to the bubble contact radius is obtained:

$$\rho_\mathrm{l} R\ddot{R} + \rho_\mathrm{l}\frac{3\dot{R}^2}{2} = \left(P_v - P_\infty - \frac{2\sigma}{R}\right)\sin^2\beta \tag{3-1}$$

The inertia-controlled bubble expansion can be divided into two stages by considering the variation of the overpressure. In the first stage, the pressure term on the right-hand-side of the equation is assumed to be constant considering the constant substrate superheat $P_v - P_\infty - \frac{2\sigma}{R} \approx \left(\frac{\Delta T}{T_\mathrm{sat}(P_\mathrm{a})}\right) h_\mathrm{lv}\rho_\mathrm{v}$. Multiplying both sides of the equation with $2R^2\dot{R}$, we can get the differential form as:

$$d\left(\rho_\mathrm{l} R^3 \dot{R}^2\right)/dt = d\left[\frac{2R^3}{3}\left(\frac{\Delta T}{T_\mathrm{sat}(P_\mathrm{a})}\right)\frac{h_\mathrm{lv}\rho_\mathrm{v}}{\rho_\mathrm{l}}\sin^2\beta\right]/dt \tag{B-5}$$

Then we do the time integration from 0 to t for the equation in the first stage:

$$\int_0^t \frac{d\left(\rho_{\mathrm{l}} R^3 \dot{R}^2\right)}{dt} dt = \left(\frac{\Delta T}{T_{\mathrm{sat}}(P_{\mathrm{a}})}\right) \frac{h_{\mathrm{lv}} \rho_{\mathrm{v}}}{\rho_{\mathrm{l}}} \sin^2 \beta \int_0^t \frac{d\left(2R^3\right)}{3dt} dt \qquad \text{(B-6)}$$

With the temporal boundary condition $R(t = 0) = 0$, we obtain the analytical solution for the vapor bubble contact radius $R(t)$:

$$R^3 \dot{R}^2 = \frac{2}{3}\left(\frac{\Delta T}{T_{\mathrm{sat}}(P_{\mathrm{a}})}\right) \frac{h_{\mathrm{lv}} \rho_{\mathrm{v}}}{\rho_{\mathrm{l}}} \sin^2 \beta \, R^3 \qquad \text{(B-7)}$$

Then the contact radius in the first stage can be solved as:

$$R\,(t) = \left[\frac{2}{3}\left(\frac{\Delta T}{T_{\mathrm{sat}}(P_{\mathrm{a}})}\right) \frac{h_{\mathrm{lv}} \rho_{\mathrm{v}}}{\rho_{\mathrm{l}}}\right]^{\frac{1}{2}} \sin\beta \cdot t \qquad \text{(3-2)}$$

During the second stage, the overpressure of the vapor bubble decreases to zero $P_v - P_\infty - \frac{2\sigma}{R} \approx 0$. And the equation reduces to the inertia form: $\rho_{\mathrm{l}} R\ddot{R} + \rho_{\mathrm{l}} \frac{3\dot{R}^2}{2} = \frac{d}{dt}\left(\rho_{\mathrm{l}} R^3 \dot{R}^2\right) = 0$. Then we integrate the differential form of the equation in the second stage. Assuming the first stage sustains between 0 to $t_1 = 0.1\ ms$ and the second stage start from t_1 with the bubble contact radius $R(t = t_1) = R_1$, we get:

$$\int_{t_1}^t \frac{d}{dt}\left(\rho_{\mathrm{l}} R^3 \dot{R}^2\right) dt = 0 \qquad \text{(B-8a)}$$

$$R^{3/2} \dot{R} = R_1^{3/2} \dot{R}_1 \qquad \text{(B-8b)}$$

here $R^{\frac{3}{2}}\dot{R}$ is the differential form of $\frac{d}{dt}\left(R^{5/2}\right)$, we get:

$$\int_{t_1}^t \frac{d}{dt}\left(R^{5/2}\right) dt = R_1^{3/2} \dot{R}_1 (t - t_1) \qquad \text{(B-9a)}$$

$$R^{5/2} = R_1^{3/2} \dot{R}_1 (t - t_1) + R_1^{5/2} = R_1^{3/2} \dot{R}_1 \left(t - t_1 + \frac{R_1}{\dot{R}_1}\right) \qquad \text{(B-9b)}$$

As a result, we have:

$$R = \left[R_1^{3/2} \dot{R}_1 \left(t - t_1 + \frac{R_1}{\dot{R}_1}\right)\right]^{0.4} \qquad \text{(B-10)}$$

We can also approximate R_1 from the above equation by taking $\frac{R_1}{\dot{R}_1} \approx t_1$ so that R during the second stage can be scaled as:

$$R = \left(R_1^{3/2} \dot{R}_1\, t\right)^{0.4} \sim t^{0.4} \qquad \text{(B-11)}$$

Supplementary Discussion 3: Upward momentum calculation

We here calculate the upward momentum as the droplet is about to detach from the substrate. In this scenario (as depicted in Fig. S5), the vapor bubble has a spherical radius of R_0 and a contact radius of R on the substrate. The apparent contact angle of the vapor bubble on the substrate is β, which relates the spherical radius and the contact radius as $R = R_0 \sin\beta$. Simultaneously, the water droplet maintains a constant diameter of D_{d} (equivalent to a radius of $\frac{D_{\mathrm{d}}}{2}$) and a contact angle of θ on the substrate. The contact angles for both the vapor bubble (β) and the water droplet (θ) are essentially determined by the same Yang-Laplace equation at the three-phase contact line. Thus, the vapor bubble's contact angle β is approximately the supplementary angle of the water droplet's contact angle θ, which means that $\beta + \theta \approx \pi$. With the relationship established between these two contact angles, the vapor bubble's spherical radius R_0 is equal to the radius of the water droplet, *i.e.*, $R_0 = \frac{D_{\mathrm{d}}}{2}$.

Now, assuming that the isotropic expansion of the vapor bubble leads to the radial water flow away from the bubble, we apply the continuity equation $\frac{\partial r^2 u}{\partial r} = 0$ where u is the radial water flow velocity and r is the radial coordinate of the droplet domain as shown in Fig. S5. Given the expansion velocity at the vapor bubble interface, denoted as $\dot{R}_0$, we can calculate the radial water flow velocity, u, at any position r inside the droplet using the equation: $u = \frac{\dot{R}_0 R_0^2}{r^2}$.

Subsequently, we determine the component of the radial water flow velocity in the z-axis direction as $U_r \cos\omega$. The upward equivalent momentum can then be calculated by integrating with the mass of the entire droplet. At the moment when the droplet is about to detach, the z-momentum of the water droplet can be expressed as an integral:

$$M_z = \rho_{\mathrm{l}} \int_{R_0}^{\frac{D_{\mathrm{d}}}{2}+2R_0\cos\beta} dr \ \cdot \int_0^{\varphi} (u\cos\omega) \cdot (2\pi r \sin\omega) \cdot (r d\omega) \tag{B-12}$$

Note that φ is the angle in the triangle ABC and can be expressed as:

$$\cos\varphi = \frac{AB^2 + BC^2 - AC^2}{2AB \cdot BC} = \frac{(2R_0\cos\beta)^2 + r^2 - R_0^2}{4rR_0\cos\beta} \tag{B-13}$$

As a result, z-momentum of the water droplet can be simplified as:

$$M_z = 2\pi\rho\dot{R}_0 R_0^2 \int_{R_0}^{R_0(1+2\cos\beta)} dr \ \cdot \int_0^{\varphi} \sin\omega \cdot \cos\omega \cdot d\omega \tag{B-14}$$

Considering that

$$\int_0^{\varphi} \sin\omega \cdot \cos\omega \cdot d\omega = -\frac{1}{4}\int_0^{\varphi} d\big(\cos(2\omega)\big) = \frac{1}{4}\big(1-\cos(2\varphi)\big) = \frac{1}{2}(1-\cos^2\varphi) \quad \text{(B-15)}$$

$$M_z = 2\pi\rho\dot{R}_0R_0^2\int_{R_0}^{R_0(1+2\cos\theta)}\frac{1}{2}(1-\cos^2\varphi)dr \quad \text{(B-16)}$$

$$\frac{1}{2}(1-\cos^2\varphi) = \frac{1}{2}\left[1-\frac{(2R_0\cos\beta)^2+r^2-R_0^2}{4rR_0\cos\beta}\right]\cdot\left[1+\frac{(2R_0\cos\beta)^2+r^2-R_0^2}{4rR_0\cos\beta}\right] \quad \text{(B-17)}$$

$$M_z = \pi\rho\dot{R}_0R_0^2\int_{R_0}^{R_0(1+2\cos\theta)}\left[1-\frac{(2R_0\cos\beta)^2+r^2-R_0^2}{4rR_0\cos\beta}\right]\cdot\left[1+\frac{(2R_0\cos\beta)^2+r^2-R_0^2}{4rR_0\cos\beta}\right]dr \quad \text{(B-18)}$$

Thus, we obtain:

$$M_z = \frac{(4-3\cos\beta)\cos\beta\pi\rho_1\dot{R}R^3}{3\sin^4\beta} \quad \text{(B-19)}$$

And the propulsive force is then evaluated by taking the time differentiation of the droplet momentum:

$$F_\mathrm{z} \approx \frac{(4-3\cos\beta)\cos\beta\pi\rho_1R^2\dot{R}^2}{\sin^4\beta} \quad \text{(3-4)}$$

Supplementary Discussion 4: Thermal boundary layer propagation

As shown in Fig. S15, the top isothermal surface temperature of the thermal boundary layer is defined as the fluid's saturation temperature (100 °C for water). With the substrate wall temperature T_w known and the initial temperature of water droplet at 20 °C, we have the heat transfer equation of the TBL as:

$$\frac{\partial T(h,t)}{\partial t} = \alpha_\mathrm{w}\frac{\partial^2 T(h,t)}{\partial h^2} \quad \text{(B-20)}$$

with boundary conditions: $T(0,t) = T_\mathrm{w}$, $T(h,0) = T_0 = 20\ ^\circ\mathrm{C}$. Then the heat transfer equation can be solved as[157]:

$$\frac{T(h,t)-T_\mathrm{w}}{T_0-T_\mathrm{w}} = \mathrm{erf}\left(\frac{h}{2\sqrt{\alpha_\mathrm{w}t}}\right) \quad \text{(B-21)}$$

where erf is the error function defined by the following integral:

$$\mathrm{erf}(\eta) = \frac{2}{\sqrt{\pi}}\int_0^{\eta}\exp(-\eta^2)\,d\eta \quad \text{(B-22)}$$

As a result, we obtain the TBL thickness $h_\mathrm{TBL} = 2\sqrt{\alpha_\mathrm{w}t}\cdot\mathrm{erf}^{-1}\left(\frac{T(h,t)-T_\mathrm{w}}{T_0-T_\mathrm{w}}\right)$ and the propagation velocity of the thermal boundary layer is $v_\mathrm{TBL} = \frac{dh}{dt} = \mathrm{erf}^{-1}\left(\frac{T(h,t)-T_\mathrm{w}}{T_0-T_\mathrm{w}}\right)\sqrt{\frac{\alpha_\mathrm{w}}{t}}$.

Supplementary Discussion 5: COMSOL simulation setup

Fig. 5b depicts the simulated temperature distribution in water droplet on the micropillared substrates by COMSOL® 5.6. In the simulation, a small control volume spanning 2 micropillars horizontally and extending 120 μm into the water body was considered. The temperature variation of the hot plate was negligible during the experiments as evidenced in Fig. S12. Direct and intimate contact of the substrate base surface with the hot plate leads us to assume a constant temperature of the substrate base (for example 130 °C). Given the substantial thermal diffusivity of silicon ($\alpha_{\mathrm{si}} = 88\ mm^2$/s) in comparison to water ($\alpha_{\mathrm{w}} = 0.165\ m^2/s$), the heat transfer process can be approximated as follows: Upon placing the droplet-substrate system onto the 130 °C hot plate, the temperature of the entire silicon substrate is expected to rapidly reach 130 °C. Consequently, heat will then propagate from the silicon substrate to the droplet, initiating a gradual increase in the temperature of the water droplet. Thus, we assume a constant uniform substrate temperature as the initial condition of the simulation. The control volume's side surface was assigned periodic boundary conditions to account for the repetitive pillars. The thermal timescale[109] was calculated to be about 25 ms, thus the simulations were conducted to capture the temperature distribution within 25 ms after substrate heating. Utilizing COMSOL® Multiphysics, we obtained the temperature distribution in the vicinity of the substrates with varying micropillar heights as shown in Supplementary Fig. 8. Specifically, we calculated the TBL thickness as $h_{\mathrm{TBL}} = \frac{V_{\mathrm{sup}}}{L_{\mathrm{p}}}$, where V_{sup} corresponds to the total volume of superheated liquid and L_{p} is the projected length of the computational domain.

Supplementary Discussion 6: Adhesion powders

The prism powder particles tested in Fig. 6 are hydrophilic and the contact angle of water droplet on the powder-coated surface is around 35° as shown in Supplementary Fig. 9. To mimic the gradual deposition of fouling particles on the surface of heat exchangers, the powder particles are initially suspended in a water droplet and then evaporation-assisted coffee ring effect leads them to deposit into the surface roughness as shown in Supplementary Fig. 10. The evaporation-induced deposition ensures a relatively tight adherence of powders to the surface, making them resistant to easy removal through conventional methods such as gas blowing or cold water droplet rinsing at room temperature, as illustrated in Supplementary Fig. 11 and Supplementary Movies 8 and 9.

Supplementary Table 2. Experimental values of advancing contact angle (ACA) and receding contact angle (RCA) on the silicon-based micropillared substrates used in this study.

Specifications	Cassie state ACA (°)	Cassie state RCA (°)	Wenzel state ACA (°)	Wenzel state RCA (°)
[D, L, H] = [20, 120, 20] μm	161±2	141±1	135±2	103±2
[D, L, H] = [20, 120, 40] μm	160±2	138±3	136±4	92±2
[D, L, H] = [20, 120, 60] μm	158±2	139±3	131±2	78±2
[D, L, H] = [20, 120, 80] μm	158±2	146±1	135±2	77±9
[D, L, H] = [20, 140, 20] μm	161±1	143±3	134±2	106±1
[D, L, H] = [20, 140, 40] μm	161±3	146±1	135±2	102±4
[D, L, H] = [20, 140, 60] μm	159±2	148±1	136±3	86±4
[D, L, H] = [20, 140, 80] μm	159±1	147±2	141±3	75±2
[D, L, H] = [20, 160, 20] μm	159±2	147±4	134±1	108±2
[D, L, H] = [20, 160, 40] μm	160±2	141±2	136±2	95±3
[D, L, H] = [20, 160, 60] μm	160±2	145±2	135±1	83±2
[D, L, H] = [20, 160, 80] μm	159±1	146±1	134±2	80±3
[D, L, H] = [30, 120, 20] μm	160±1	139±1	139±1	98±1
[D, L, H] = [30, 120, 40] μm	159±2	142±3	143±1	97±2
[D, L, H] = [30, 120, 60] μm	159±2	135±4	139±1	73±2
[D, L, H] = [30, 120, 80] μm	157±2	140±5	148±1	77±5
[D, L, H] = [30, 140, 20] μm	159±1	145±2	139±1	108±4
[D, L, H] = [30, 140, 40] μm	158±2	143±1	143±4	102±3
[D, L, H] = [30, 140, 60] μm	159±4	140±4	140±4	85±1
[D, L, H] = [30, 140, 80] μm	160±1	144±2	145±3	75±1
[D, L, H] = [30, 160, 20] μm	161±1	147±1	135±2	107±4
[D, L, H] = [30, 160, 40] μm	158±1	143±3	147±2	104±3
[D, L, H] = [30, 160, 60] μm	160±2	137±3	145±2	85±3
[D, L, H] = [30, 160, 80] μm	160±2	143±2	142±1	83±6
[D, L, H] = [40, 120, 20] μm	159±2	132±5	149±2	96±2
[D, L, H] = [40, 120, 40] μm	160±2	134±4	160±2	102±1
[D, L, H] = [40, 120, 60] μm	160±2	121±5	145±4	65±4
[D, L, H] = [40, 120, 80] μm	159±1	139±4	151±1	62±8
[D, L, H] = [40, 140, 20] μm	157±1	143±2	140±1	102±2
[D, L, H] = [40, 140, 40] μm	159±2	139±4	150±2	97±2
[D, L, H] = [40, 140, 60] μm	160±2	141±1	149±4	84±1
[D, L, H] = [40, 140, 80] μm	159±2	143±3	149±3	73±4

[*D*, *L*, *H*] = [40, 160, 20] µm	160±2	142±1	138±1	108±1
[*D*, *L*, *H*] = [40, 160, 40] µm	160±2	142±3	142±2	96±3
[*D*, *L*, *H*] = [40, 160, 60] µm	159±1	139±3	146±2	88±3
[*D*, *L*, *H*] = [40, 160, 80] µm	160±3	146±1	147±2	87±4

Appendix C: Supporting Information for Chapter 4

Supplementary Figures

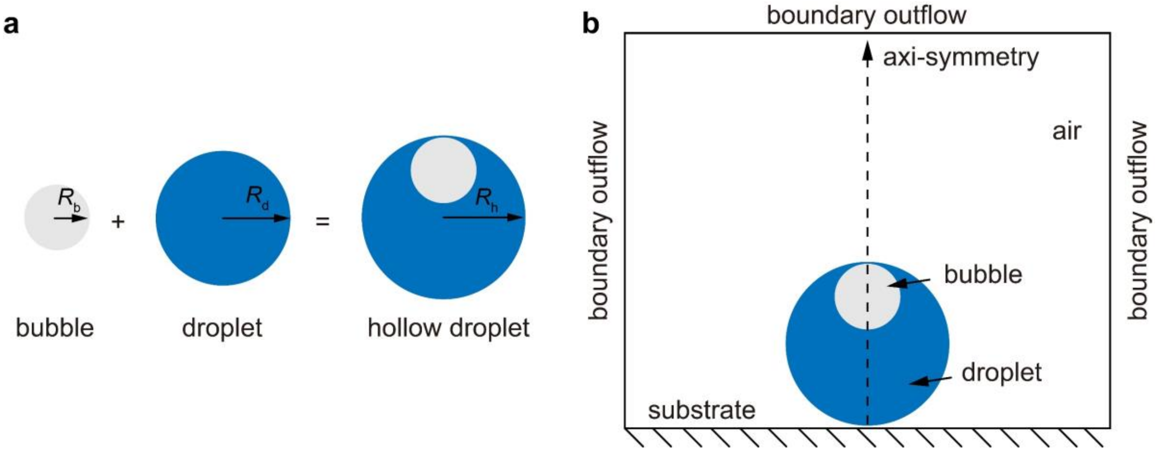

Figure C-1. Direct numerical simulation setup. a Definition of the geometry radii of the initial water droplet $\boldsymbol{R}_{\mathbf{d}}$, injected air bubble $\boldsymbol{R}_{\mathbf{b}}$ and hollow droplet $\boldsymbol{R}_{\mathbf{h}}$. **b** Axisymmetric computational domain used to study the bubble burst-induced droplet jumping.

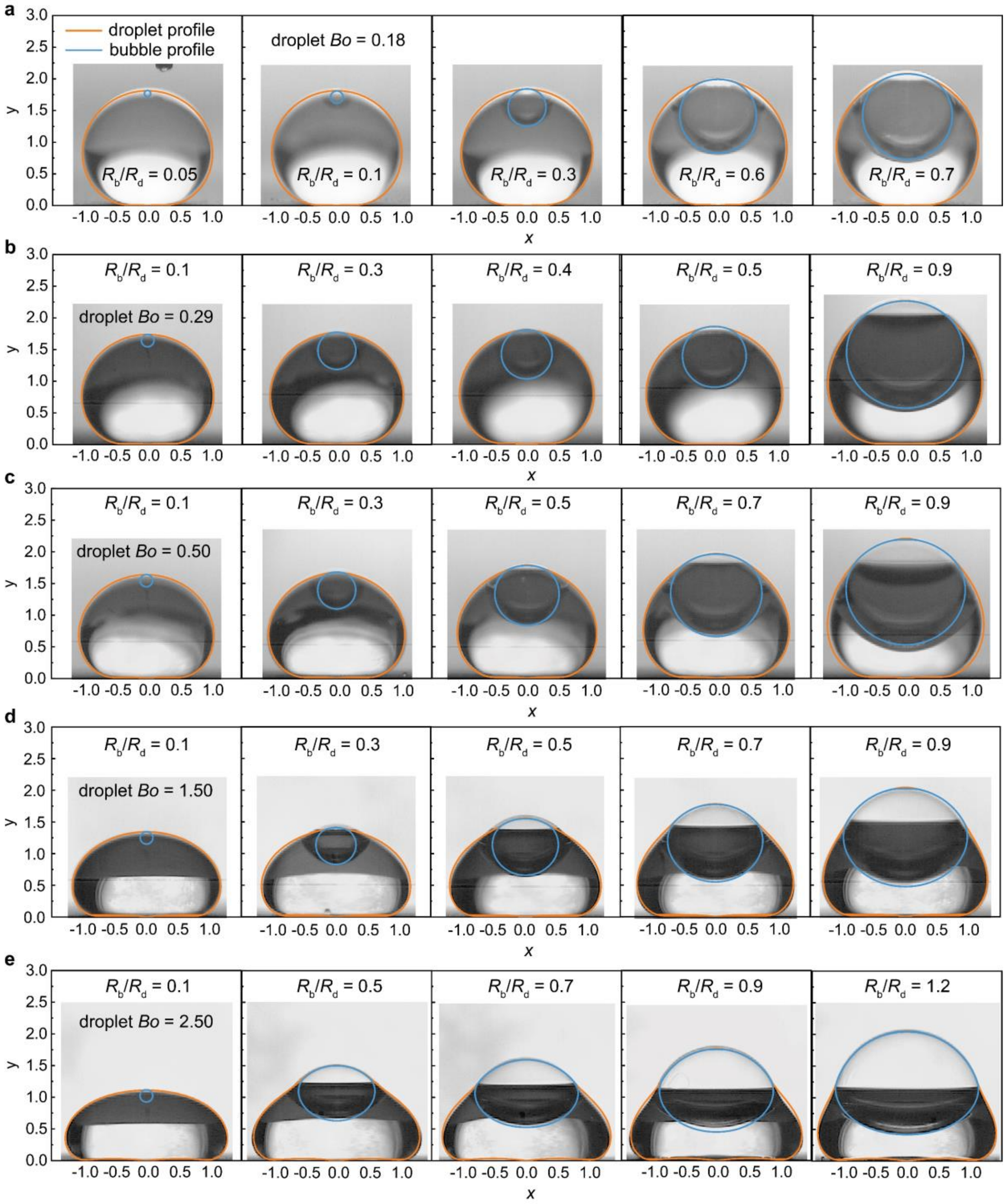

Figure C-2. Comparison of hollow droplet profiles from DNS simulations with experimental snapshots. a-e Profiles of sessile droplets and floating bubbles generated from simulations with varying droplet Bond numbers and injected bubble sizes. Using the bubble size obtained from simulations, we compare the simulated profiles with experimental snapshots to estimate the injected bubble dimensions.

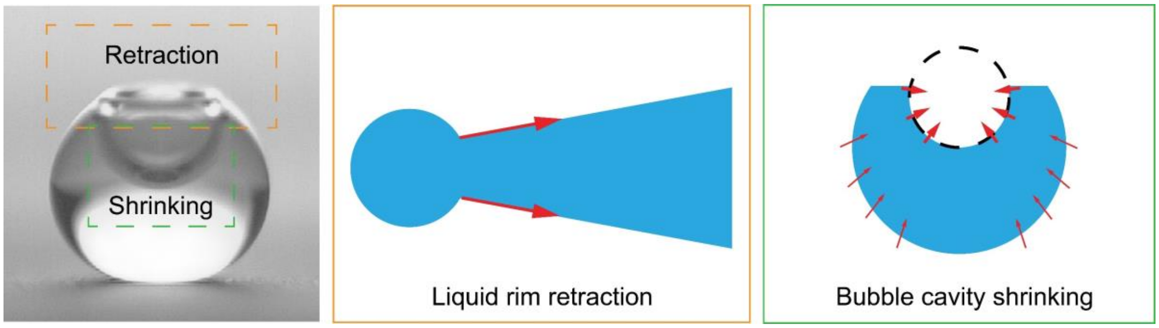

Figure C-3. Combined flow of liquid rim retraction and bubble cavity shrinking.

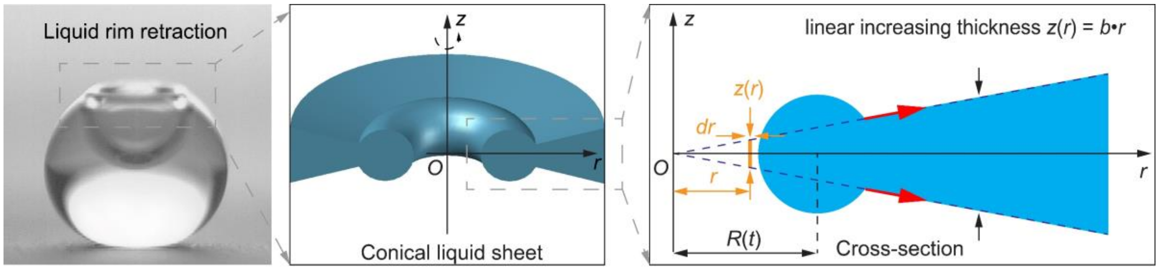

Figure C-4. Liquid rim retraction modeled as a conical liquid sheet retraction.

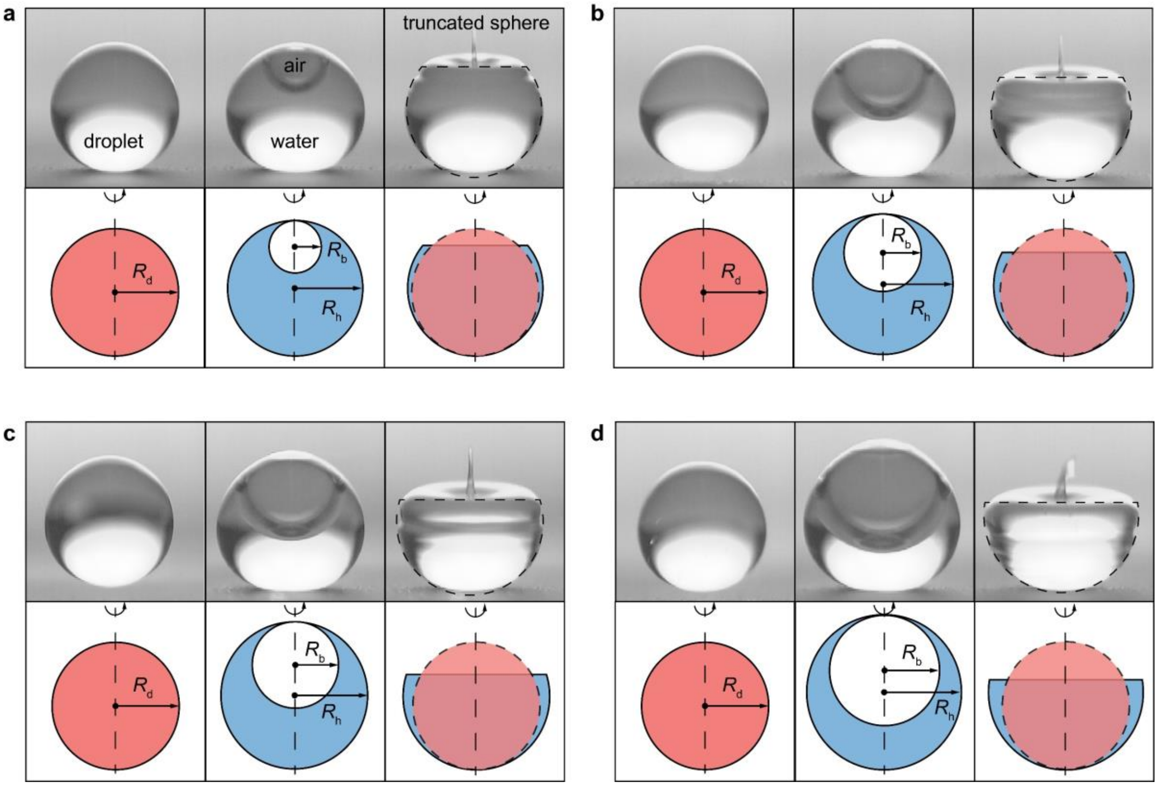

Figure C-5. Formation of the truncated spherical droplet after bubble bursting. a-d Experimental snapshots and schematic diagrams illustrating the formation of truncated spherical droplets across varying bubble sizes, with a droplet Bond number of 0.29.

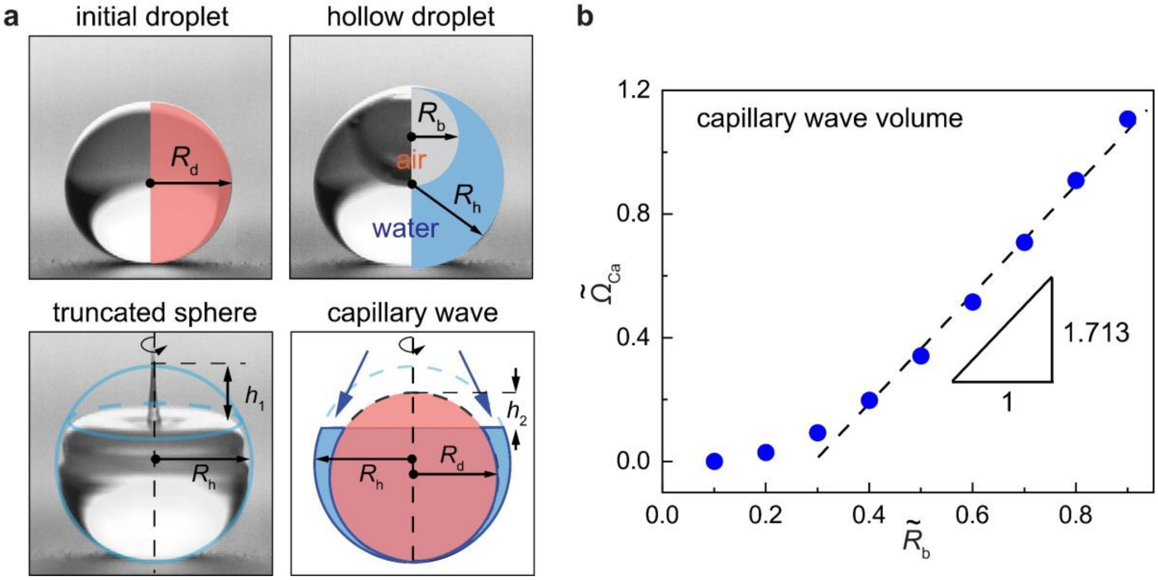

Figure C-6. Capillary wave volume calculation. a Definition of the capillary wave domain and geometry. **b** Plot of the calculated capillary wave volume $\boldsymbol{\tilde{\Omega}_{Ca}}$ as a function of injected bubble radius $\boldsymbol{\tilde{R}_b}$, regarding a droplet of constant radius $\boldsymbol{R_d}$. It can be seen that $\boldsymbol{\tilde{\Omega}_{Ca}}$ scales almost linearly with $\boldsymbol{\tilde{R}_b}$ when $\boldsymbol{\tilde{R}_b > 0.3}$.

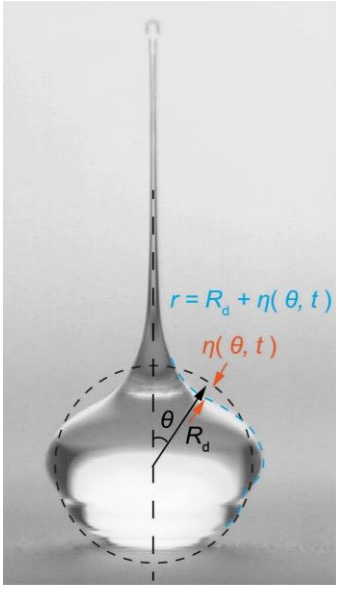

Figure C-7. Definition of droplet interface profile. The radial distance between the droplet interface and its center of mass is defined as $\boldsymbol{r} = \boldsymbol{R}_\mathbf{d} + \boldsymbol{\eta}(\boldsymbol{\theta}, \boldsymbol{t})$, where $\boldsymbol{R}_\mathbf{d}$ represents the initial droplet radius, and $\boldsymbol{\eta}(\boldsymbol{\theta}, \boldsymbol{t})$ denotes a surface perturbation.

Supplementary Discussion 1: Basilisk direct numerical simulation

To accurately capture the static shape of the sessile droplet under gravity and systematically describe the subsequent processes such as liquid rim retraction, cavity collapse, jet formation, capillary wave impacting and droplet rebound jumping, we conducted direct numerical simulations (DNS) using the open-source platform Basilisk[144, 145]. This section outlines the framework used for DNS in our exploration of the bubble burst-induced droplet jumping, as shown in Fig. S1.

The governing equations for the droplet jumping process are the Navier-Stokes equations:

$$\rho \frac{\partial \boldsymbol{u}}{\partial t} + \rho \nabla \cdot (\boldsymbol{u}\boldsymbol{u}) = -\nabla p + \nabla \cdot (2\mu \boldsymbol{D}) + \boldsymbol{f} \tag{C-1}$$

$$\nabla \cdot \boldsymbol{u} = 0 \tag{C-2}$$

where $\boldsymbol{u}$ is the fluid velocity field, p is the pressure field, $\boldsymbol{D} = [\nabla \boldsymbol{u} + (\nabla \boldsymbol{u})^T]/2$ is the deformation tensor, and $\boldsymbol{f}$ represents the external forces. Here ρ and μ are the fluid density and viscosity, respectively. Incompressibility is assumed, making the velocity field divergence-free.

The droplet jumping process involves multiphase (primarily two-phase) flow dynamics. In the simulation, we applied the “one fluid” method, with the fluid density and viscosity determined using the liquid volume fraction c:

$$\rho = c\rho_{\mathrm{d}} + (1-c)\rho_{\mathrm{g}} \tag{C-3}$$

$$\mu = c\mu_{\mathrm{d}} + (1-c)\mu_{\mathrm{g}} \tag{C-4}$$

with ρ_{d}, ρ_{g} and μ_{d}, μ_{g} the densities and viscosities of the liquid and gas. Here we have $c = 1$ for liquid and $c = 0$ for gas.

Considering the constant values of liquid and gas density, the advection equation for density can thus be simplified by the advection equation for the volume fraction:

$$\frac{\partial \rho}{\partial t} + \nabla \cdot (\rho \boldsymbol{u}) = 0 \tag{C-5}$$

$$\frac{\partial c}{\partial t} + \nabla \cdot (c \boldsymbol{u}) = 0 \tag{C-6}$$

The external force term $\boldsymbol{f}$ includes body force and surface force:

$$\boldsymbol{f}=\rho\boldsymbol{g}+\gamma\kappa\delta_{\mathrm{s}}\boldsymbol{n} \tag{C-7}$$

where $\boldsymbol{g}$ is the gravitational acceleration, γ is the surface tension coefficient, κ is the curvature of the interface, $\boldsymbol{n}$ is the interface normal and δ_{s} is the Dirac distribution function.

For the simulation, the time discretization uses a second-order accurate staggered method. As a result, the discretized Navier-Stokes equations become[145]:

$$\rho_{n+\frac{1}{2}}\left[\frac{\boldsymbol{u}_{n+1}-\boldsymbol{u}_n}{\Delta t}+\boldsymbol{u}_{n+\frac{1}{2}}\cdot\nabla\boldsymbol{u}_{n+\frac{1}{2}}\right]=-\nabla p_{n+\frac{1}{2}}+\nabla\cdot\left[\mu_{n+\frac{1}{2}}(\boldsymbol{D}_{n+1}+\boldsymbol{D}_n)\right]+(\gamma\kappa\delta_s\boldsymbol{n})_{n+\frac{1}{2}} \tag{C-8}$$

$$\frac{c_{n+\frac{1}{2}}-c_{n-\frac{1}{2}}}{\Delta t}+\nabla\cdot(c_n\boldsymbol{u}_n)=0 \tag{C-9}$$

$$\nabla\cdot\boldsymbol{u}_n=0 \tag{C-10}$$

Using a time splitting projection method, the discretized Navier-Stokes equations can be further simplified as:

$$\rho_{n+\frac{1}{2}}\left[\frac{\boldsymbol{u}_*-\boldsymbol{u}_n}{\Delta t}+\boldsymbol{u}_{n+\frac{1}{2}}\cdot\nabla\boldsymbol{u}_{n+\frac{1}{2}}\right]=\nabla\cdot\left[\mu_{n+\frac{1}{2}}(\boldsymbol{D}_*+\boldsymbol{D}_n)\right]+(\gamma\kappa\delta_s\boldsymbol{n})_{n+\frac{1}{2}} \tag{C-11}$$

$$\boldsymbol{u}_{n+1}=\boldsymbol{u}_*-\frac{\Delta t}{\rho_{n+\frac{1}{2}}}\nabla p_{n+\frac{1}{2}} \tag{C-12}$$

$$\nabla\cdot\boldsymbol{u}_{n+1}=0 \tag{C-13}$$

To solve the above equations the following Poisson equation is required:

$$\nabla\cdot\left[\frac{\Delta t}{\rho_{n+\frac{1}{2}}}\nabla p_{n+\frac{1}{2}}\right]=\nabla\cdot\boldsymbol{u}_* \tag{C-14}$$

This equation is solved using a quad/octree-based multilevel solver, incorporating an underlying linear Gauss-Seidel method[144]. Here the $n+\frac{1}{2}$ represents the fractional time step as introduced by the Godunov produce[158].

To obtain the temporary velocity $\boldsymbol{u}_*$, we reorganized the momentum equation as:

$$\frac{\rho_{n+\frac{1}{2}}}{\Delta t}\boldsymbol{u}_*-\nabla\cdot\left(\mu_{n+\frac{1}{2}}\boldsymbol{D}_*\right)=\nabla\cdot\left(\mu_{n+\frac{1}{2}}\boldsymbol{D}_n\right)+(\gamma\kappa\delta_{\mathrm{s}}\boldsymbol{n})_{n+\frac{1}{2}}+\rho_{n+\frac{1}{2}}\left[\frac{\boldsymbol{u}_n}{\Delta t}-\boldsymbol{u}_{n+\frac{1}{2}}\cdot\nabla\boldsymbol{u}_{n+\frac{1}{2}}\right] \tag{C-15}$$

It is observed that the right-hand side of the equation depends only on values at times n and $n+\frac{1}{2}$. To numerically solve the equation, the viscous terms are discretized using the Crank-Nicholson scheme, which is second-order accurate and unconditional stable. The velocity advection term is estimated using the Bell-Collella-Glaz second order unsplit upwind scheme[158], which remains stable for CFL < 1. Additionally, the liquid-gas interface is reconstructed at each time step, with the interface normal $\boldsymbol{n}$ computed using a mixed Youngs-centered method[159]. The surface tension force is calculated via a balanced-force surface tension approach[160], while the interface curvature is obtained using a second-order height function technique[145].

In conducting the DNS, we nondimensionalize the velocity field using the inertia-capillary velocity $\sqrt{\gamma/(\rho_\mathrm{d}R_\mathrm{d})}$, length by the droplet radius R_d, time by the inertia-capillary timescale $\sqrt{\rho_\mathrm{d}R_\mathrm{d}^3/\gamma}$, and pressure by the Laplace pressure γ/R_d. Consequently, the Navier-Stokes equations of the system can be nondimensionalized and presented as:

$$\frac{\partial\tilde{\boldsymbol{u}}}{\partial\tilde{t}}+\widetilde{\nabla}\cdot(\tilde{\boldsymbol{u}}\tilde{\boldsymbol{u}})=\frac{1}{\tilde{\rho}}\left(-\widetilde{\nabla}\tilde{p}+Oh\cdot\widetilde{\nabla}^2\tilde{\boldsymbol{u}}-\tilde{\rho}Bo\hat{\boldsymbol{z}}+\tilde{\boldsymbol{f}}\right) \tag{C-16}$$

$$\widetilde{\nabla}\cdot\tilde{\boldsymbol{u}}=0 \tag{C-17}$$

where Oh and Bo represent the Ohnesorge and Bond numbers. Initially, the system involves three phases: liquid, bubble and air. Using the one-fluid approximation, the density and the Oh are expressed as:

$$\tilde{\rho}=c_1+c_2\frac{\rho_\mathrm{b}}{\rho_\mathrm{d}}+(1-c_1-c_2)\frac{\rho_\mathrm{a}}{\rho_\mathrm{d}} \tag{C-18}$$

$$Oh=c_1Oh_\mathrm{d}+c_2Oh_\mathrm{b}+(1-c_1-c_2)Oh_\mathrm{a} \tag{C-19}$$

where c_1 and c_2 are the volume fractions for liquid and bubble regions, respectively. The subscript d denotes for the droplet liquid region, b donates for the bubble region and a donates for the surrounding air region. The Ohnesorge numbers for the corresponding regions are expressed as: $Oh_\mathrm{d}=\mu_\mathrm{d}/\sqrt{\gamma\rho_\mathrm{d}R_\mathrm{d}}$, $Oh_\mathrm{b}=\mu_\mathrm{b}/\sqrt{\gamma\rho_\mathrm{d}R_\mathrm{d}}$ and $Oh_\mathrm{a}=\mu_\mathrm{a}/\sqrt{\gamma\rho_\mathrm{d}R_\mathrm{d}}$ with μ the dynamic viscosity of the corresponding region. Note that since the bubble is essentially formed by the injected air, the density and viscosity of the bubble region and the surrounding air regions are assumed equal: $\rho_{\mathrm{b}} = \rho_{\mathrm{a}}$ and $\mu_{\mathrm{b}} = \mu_{\mathrm{a}}$.

We have $\tilde{\boldsymbol{f}}$ representing the surface tension force, and it is calculated as a singular body force at the interface:

$$\tilde{\boldsymbol{f}} \approx \tilde{\kappa}_1 \tilde{\nabla} c_1 + \tilde{\kappa}_2 \tilde{\nabla} c_2 \tag{C-20}$$

Before the simulation of the droplet jumping dynamic process, we should first determine the static shape of the sessile hollow droplet, which would be used as the initial shape condition for the subsequent simulation. Initially, all hollow droplets assume a perfect shape but deform under the influence of gravity, causing the liquid parts to gradually flatten while the air bubble floats. Experimentally, the silicon wafer substrate is coated carefully to obtain the non-wetting and non-adhesion properties. Correspondingly, in the simulation, we maintain the ideal non-wetting and non-adhesion conditions by introducing a thin air layer between the droplet base and the substrate surface[133]. The static state of the hollow droplet is established by calculating the nondimensional kinetic energy of the entire system; a value less than 10^{-6} indicates that the static state has been achieved. The profiles of the eventually static hollow droplets of various sizes are presented in Fig. S2.

We do not attempt to numerically resolve the breakup of the initial film (the bubble cap); instead, we begin the simulation directly with the open cavity[161]. Using the initial profile of the droplet, we can obtain the profile of the sessile droplet with the open cavity. At this stage, the system is treated as a two-phase problem with:

$$Oh = \phi_1 Oh_{\mathrm{d}} + (1 - \phi_1) Oh_{\mathrm{a}} \tag{C-21}$$

$$\tilde{\rho} = \phi_1 + (1 - \phi_1) \frac{\rho_{\mathrm{a}}}{\rho_{\mathrm{d}}} \tag{C-22}$$

In this study, we utilized adaptive mesh refinement (AMR) approach of Basilisk to accurately resolve the bubble cavity collapsing, jetting formation at a high resolution, achieving a grid size equivalent to 4096^2. This resolution is crucial for obtaining numerically converged results, especially for the narrow, high-speed jets.

The volume of the droplet can be accurately measured using a pipette (Fisherbrand FBE00100), allowing for precise determination of its radius. However, the irregular shape of the air bubble complicates direct measurement of its radius. Therefore, we determine the radius of the air bubble by comparing experimental snapshots with the simulation profile, as illustrated in Fig. S2, where the radius of the simulation air bubble is known. The numerical results exhibit a strong correlation with the experimental snapshots of hollow droplets with varying sizes and varying bubble sizes.

Supplementary Discussion 2: Liquid rim retraction and droplet shrinking

After the bubble bursts, the fluid motion of the droplet can be characterized by a combination of liquid rim retraction[162] and bubble cavity shrinking, as illustrated in Fig. S3. Typically, the retraction velocity of the liquid rim exceeds that of the shrinking bubble cavity. Here, we provide a detailed discussion of these two velocities.

Following the rupture of the bubble cap, the initial orifice expands radially due to capillary forces, which drive the retraction of the liquid shell surrounding the hollow droplet. Experimentally, the thickness of the droplet shell is not uniform; instead, it progressively increases. To simplify this process and provide a theoretical estimation, we model the retraction as that of a conical liquid sheet, where the film thickness increases linearly along its length $z(r) = b \cdot r$, as shown in Fig. S4.

Based on this geometric simplification, we can calculate the momentum of the retracting liquid rim. The conical geometry allows us to integrate the gradually increasing thickness of the liquid sheet, yielding a more accurate estimate of the rim's momentum while the rim is retracting:

$$M_{\mathrm{r}}(t) = \rho_{\mathrm{d}} \int_0^{R(t)} 2\pi r z(r) dr \cdot \frac{dR}{dt} \tag{C-23}$$

At the same time, the capillary force in the radial r direction is calculated as:

$$F_{\mathrm{r}}(t) = 2\pi R(t) \cdot 2\gamma \cdot \left[1 + \frac{1}{4} \frac{dz(R)}{dr}^2\right]^{-1/2} \tag{C-24}$$

As a result, the force balance yields:

$$\frac{d}{dt}\left(\rho_{\mathrm{d}} \int_0^{R(t)} 2\pi r z(r) dr \cdot \frac{dR}{dt}\right) = 2\pi R(t) \cdot 2\gamma \cdot \left[1 + \frac{1}{4} \frac{dz(R)}{dr}^2\right]^{-1/2} \tag{C-25}$$

with $R(0) = 0$.

Eventually, we can find that:

$$R(t) = \left(\sqrt{\frac{27\gamma}{5\rho_{\mathrm{d}} b\sqrt{1+b^2/4}}}\,t\right)^{\frac{2}{3}} \sim (\gamma t^2/\rho_{\mathrm{d}})^{\frac{1}{3}} \qquad \text{(C-26)}$$

And the liquid rim retraction velocity v_{r} is calculated as:

$$v_{\mathrm{r}}(t) = \frac{dR}{dt} = \frac{2}{3}\sqrt[3]{\frac{27\gamma}{5\rho_{\mathrm{d}} b\sqrt{1+b^2/4}}} \cdot t^{-\frac{1}{3}} \sim \sqrt[3]{\frac{\gamma}{\rho_{\mathrm{d}}}} \cdot t^{-\frac{1}{3}} \qquad \text{(C-27)}$$

Notice that a singularity occurs at $t = 0$, indicating that the radial velocity v_{r} starts at a very large value and gradually decreases over time, folloing a $t^{-1/3}$ decay. Here we estimate the lateral retraction velocity at $t_{\mathrm{r}} = \sqrt{\rho_{\mathrm{d}} R_{\mathrm{b}}^3/\gamma}$. Consequently, the lateral characteristic retraction velocity can be scaled as:

$$v_{\mathrm{r}}(t_{\mathrm{r}}) \sim \sqrt{\frac{\gamma}{\rho_{\mathrm{d}} R_{\mathrm{b}}}} \qquad \text{(C-28)}$$

Simultanesouly, the shrinking of the bubble cavity, driven by the Laplace pressure difference γ/R_{b}, can be characterized by the inertia-capillary velocity. Using the bubble radius R_{b} as the characteristic length, the shrinking velocity of the cavity can be scaled as $v_{\mathrm{c}}(t) \sim \sqrt{\gamma/\rho_{\mathrm{d}} R_{\mathrm{b}}}$. The shrinking of the bubble cavity induces a roughly radial velocity field within the droplet, which drives the contraction of the droplet's outer surface. Based on the conservation of mass, the shrinking velocity of the droplet's outer surface can be scaled as:

$$v_{\mathrm{s}}(t) \sim \frac{R_{\mathrm{b}}^2}{R_{\mathrm{h}}^2}\sqrt{\frac{\gamma}{\rho_{\mathrm{d}} R_{\mathrm{b}}}} \qquad \text{(C-29)}$$

It is clear that the shrinking velocity v_{s} is significantly smaller than the laterally characteristic retraction velocity $v_{\mathrm{r}}(t_{\mathrm{r}})$, and far smaller than the initially large retraction velocity $v_{\mathrm{r}}(t_0)$. Thus, it is reasonable to conclude that the rim retraction velocity dominates over the shrinking velocity of bubble cavity throughout the process.

Supplementary Discussion 3: Capillary wave volume calculation

As shown in Fig. S6, a droplet with radius R_d is initially deposited on the non-wetting substrate. Then an air bubble with radius R_b is injected into it, forming a stable hollow droplet with a radius R_h. Based on volume conservation, we have:

$$\frac{4}{3}\pi R_\mathrm{h}^3 = \frac{4}{3}\pi R_\mathrm{d}^3 + \frac{4}{3}\pi R_\mathrm{b}^3 \tag{C-30}$$

After the bubble bursting, the liquid rim filled the bubble cavity with the rest of the droplet profile remaining almost unaltered. Then we have the droplet in the truncated spherical shape with the same volume:

$$\frac{4\pi}{3} R_\mathrm{d}^3 = \frac{4\pi}{3} R_\mathrm{h}^3 - \frac{\pi}{3} h_1^2(3R_\mathrm{h} - h_1) \tag{C-31}$$

Then, the truncated sphere droplet would intend to recover the initial spherical shape with the non-overlapping region between the truncated sphere and the original droplet sphere being defined as the domain of capillary waves. Based on this geometry configuration, we have:

$$h_2 = 2R_\mathrm{d} - (2R_\mathrm{h} - h_1) \tag{C-32}$$

Finally, the volume of the capillary wave is calculated as:

$$\Omega_\mathrm{Ca}(R_\mathrm{b}, R_\mathrm{d}) = \frac{\pi}{3} h_2^2(3R_\mathrm{d} - h_2) \tag{C-33}$$

It is challenging to calculate the volume of the capillary wave Ω_Ca explicitly and we calculate it numerically. Here we nondimensionalize all the length scale with R_d, and as a result we have $\tilde{R}_\mathrm{d} = R_\mathrm{d}/R_\mathrm{d} = 1$ and $\tilde{R}_\mathrm{b} = R_\mathrm{b}/R_\mathrm{d}$ varying from 0.1 to 0.9. The nondimensional capillary wave $\widetilde{\Omega}_\mathrm{Ca} = \Omega_\mathrm{Ca}/R_\mathrm{d}^3$ is then calculated and plotted in Fig. S6b.

As a result, based on the geometry calculation, we find that the volume of the capillary wave $\widetilde{\Omega}_\mathrm{Ca}$ is proportional to the bubble radius $\tilde{R}_\mathrm{b}$ as $\tilde{R}_\mathrm{b} > 0.3$:

$$\widetilde{\Omega}_\mathrm{Ca} \sim \tilde{R}_\mathrm{b} \tag{C-34}$$

Supplementary Discussion 4: Droplet capillary oscillation

In the droplet jumping process, the flow is considered irrotational. Consequently, the velocity potential ($\boldsymbol{u} = \nabla\phi(r,\theta,t)$) satisfies the Laplace equation:

$$\nabla^2\phi = 0 \tag{C-35}$$

To analyze the kinematic boundary condition at the droplet interface, we define the radial distance between the droplet interface and its center of mass as $r = R_{\mathrm{d}} + \eta(\theta,t)$, where R_{d} represents the initial droplet radius, and $\eta(\theta,t)$ denotes a surface perturbation as shown in Fig. S7. This allows us to express the interface equation as:

$$H(r,\theta,t) = r - [R_{\mathrm{d}} + \eta(\theta,t)] = 0 \tag{C-36}$$

Taking the total derivative of the interface equation and expressing it in spherical coordinates yields:

$$\frac{DH}{Dt} = \frac{\partial H}{\partial t} + (\boldsymbol{u}\cdot\nabla)H = \frac{\partial H}{\partial t} + \frac{\partial\phi}{\partial r}\frac{\partial H}{\partial r} + \frac{1}{r^2}\frac{\partial\phi}{\partial\theta}\frac{\partial H}{\partial\theta} = 0 \tag{C-37}$$

$$-\frac{\partial\eta}{\partial t} + \frac{\partial\phi}{\partial r} + \frac{1}{r^2}\frac{\partial\phi}{\partial\theta}\left(-\frac{\partial\eta(\theta,t)}{\partial\theta}\right) = 0 \tag{C-38}$$

with $r = R_{\mathrm{d}} + \eta(\theta,t)$.

Next, we consider the pressure boundary condition. The pressure difference between the inside and outside of the droplet is given by[163]:

$$p^{\mathrm{in}} - p^{\mathrm{out}} = \gamma\left(\frac{1}{R_1} + \frac{1}{R_2}\right) \tag{C-39}$$

where R_1 and R_2 are the principal radii of curvature.

We have the pressure p expressed as the summation of base pressure p_{b} and the perturbation pressure p_{p}:

$$p^{\mathrm{in}} = p_{\mathrm{b}}^{\mathrm{in}} + p_{\mathrm{p}}^{\mathrm{in}} \tag{C-40}$$

For the base pressure we have:

$$p_{\mathrm{b}}^{\mathrm{in}} - p_{\mathrm{b}}^{\mathrm{out}} = \frac{2\gamma}{R_{\mathrm{b}}} \tag{C-41}$$

In the spherical coordinate, the surface curvature is calculated as:

$$\left(\frac{1}{R_1}+\frac{1}{R_2}\right)=\nabla\cdot\boldsymbol{n}=\frac{2}{r}-\frac{1}{r^2}\cot\theta\frac{\partial\eta}{\partial\theta}-\frac{1}{r^2}\frac{\partial^2\eta}{\partial\theta^2} \qquad \text{(C-42)}$$

with $r=R_\mathrm{d}+\eta$, we have:

$$\nabla\cdot\boldsymbol{n}=\frac{2}{R_\mathrm{d}+\eta}-\frac{1}{(R_\mathrm{d}+\eta)^2}\cot\theta\frac{\partial\eta}{\partial\theta}-\frac{1}{(R_\mathrm{d}+\eta)^2}\frac{\partial^2\eta}{\partial\theta^2} \qquad \text{(C-43)}$$

As a result, we will have:

$$\left(p_\mathrm{b}^\mathrm{in}-p_\mathrm{b}^\mathrm{out}\right)_{r=R_\mathrm{d}}+\left(p_\mathrm{p}^\mathrm{in}-p_\mathrm{p}^\mathrm{out}\right)_{r=R_\mathrm{d}+\eta(\theta,t)}=\gamma\left(\frac{2}{R_\mathrm{d}+\eta}-\frac{1}{(R_\mathrm{d}+\eta)^2}\cot\theta\frac{\partial\eta}{\partial\theta}-\frac{1}{(R_\mathrm{d}+\eta)^2}\frac{\partial^2\eta}{\partial\theta^2}\right) \qquad \text{(C-44)}$$

Since $\eta \ll R_\mathrm{d}$, we have:

$$\frac{2}{R_\mathrm{d}+\eta}=\frac{2}{R_\mathrm{d}\left(1+\frac{\eta}{R_\mathrm{d}}\right)}\approx\frac{2}{R_\mathrm{d}}\left(1-\frac{\eta}{R_\mathrm{d}}\right) \qquad \text{(C-45)}$$

with $\left(p_\mathrm{b}^\mathrm{in}-p_\mathrm{b}^\mathrm{out}\right)_{r=R_\mathrm{d}}=\frac{2\gamma}{R_\mathrm{d}}$, the pressure equation simplifies to:

$$\left(p_\mathrm{p}^\mathrm{in}-p_\mathrm{p}^\mathrm{out}\right)_{r=R_\mathrm{d}+\eta(\theta,t)}=\gamma\left(-\frac{2\eta}{R_\mathrm{d}^2}-\frac{1}{R_\mathrm{d}^2}\cot\theta\frac{\partial\eta}{\partial\theta}-\frac{1}{R_\mathrm{d}^2}\frac{\partial^2\eta}{\partial\theta^2}\right) \qquad \text{(C-46)}$$

Assuming the fluid flow to be potential and inviscid, we have the linear form of the unsteady Bernoulli equation:

$$\nabla\left(\frac{\partial\phi}{\partial t}+\frac{p}{\rho}+\phi\right)=0 \qquad \text{(C-47)}$$

yielding

$$\frac{p^\mathrm{in}}{\rho}=\frac{p_\mathrm{b}^\mathrm{in}+p_\mathrm{p}^\mathrm{in}}{\rho}=-\frac{\partial\phi^\mathrm{in}}{\partial t}+D_1 \qquad \text{(C-48)}$$

$$\frac{p^\mathrm{out}}{\rho}=\frac{p_\mathrm{b}^\mathrm{out}+p_\mathrm{p}^\mathrm{out}}{\rho}=-\frac{\partial\phi^\mathrm{out}}{\partial t}+D_2 \qquad \text{(C-49)}$$

The constants cancel out with the base pressure term:

$$\left(p_\mathrm{b}^\mathrm{in}-p_\mathrm{b}^\mathrm{out}\right)_{r=R_\mathrm{d}}=\frac{2\gamma}{R_\mathrm{d}} \qquad \text{(C-50)}$$

Finally, we obtain:

$$\rho_\mathrm{a}\left(\frac{\partial\phi^\mathrm{out}(r,\theta,t)}{\partial t}\right)_{r=R_\mathrm{d}}-\rho_\mathrm{d}\left(\frac{\partial\phi^\mathrm{in}(r,\theta,t)}{\partial t}\right)_{r=R_\mathrm{d}}=\gamma\left(-\frac{2\eta}{R_\mathrm{d}^2}-\frac{1}{R_\mathrm{d}^2}\cot\theta\frac{\partial\eta}{\partial\theta}-\frac{1}{R_\mathrm{d}^2}\frac{\partial^2\eta}{\partial\theta^2}\right) \qquad \text{(C-51)}$$

For a theoretical estimation in this work, we ignore the nonlinear terms in the boundary conditions and use a linear approximation. Specifically, we define a small parameter ϵ and expand η and ϕ as:

$$\phi(r,\theta,t) = 0 + \epsilon\phi_1 + \epsilon^2\phi_2 + O(\epsilon^2) \tag{C-52}$$

$$\eta(\theta,t) = 0 + \epsilon\eta_1 + \epsilon^2\eta_2 + O(\epsilon^2) \tag{C-53}$$

As a result, we have the Taylor expansion for the velocity potential:

$$\left(\frac{\partial\phi(r,\theta,t)}{\partial r}\right)_{r=R_\mathrm{d}+\eta(\theta,t)} = \left(\frac{\partial\phi}{\partial r}\right)_{r=R_\mathrm{d}} + \left(\frac{\partial^2\phi}{\partial r^2}\right)_{r=R_\mathrm{d}} \cdot \eta(\theta,t) + \cdots \tag{C-54}$$

where the term $\left(\frac{\partial^2\phi}{\partial r^2}\right)_{r=R_\mathrm{d}} \cdot \eta(\theta,t)$ includes $\phi \cdot \eta$, which is of order is $O(\epsilon^2)$. Therefore, in the linear analysis, we only consider the first term in the expansion.

Applying this to the kinematic boundary condition gives us:

$$-\frac{\partial\eta}{\partial t} + \frac{\partial\phi}{\partial r} = 0 \tag{C-55}$$

at $r = R_\mathrm{d}$.

And also, for the pressure boundary condition, we have:

$$\rho_\mathrm{a}\left(\frac{\partial\phi^\mathrm{out}(r,\theta,t)}{\partial t}\right)_{r=R_\mathrm{d}} - \rho_\mathrm{d}\left(\frac{\partial\phi^\mathrm{in}(r,\theta,t)}{\partial t}\right)_{r=R_\mathrm{d}} = \gamma\left(-\frac{2\eta}{R_\mathrm{d}^2} - \frac{1}{R_\mathrm{d}^2}\cot\theta\frac{\partial\eta}{\partial\theta} - \frac{1}{R_\mathrm{d}^2}\frac{\partial^2\eta}{\partial\theta^2}\right) \tag{C-56}$$

In summary, the governing equations and boundary conditions are as follows:
Laplace equation:

$$\frac{1}{r^2}\frac{\partial}{\partial r}\left(r^2\frac{\partial\phi}{\partial r}\right) + \frac{1}{r^2\sin\theta}\frac{\partial}{\partial\theta}\left(\sin\theta\frac{\partial\phi}{\partial\theta}\right) = 0 \tag{C-57}$$

linearized kinematic boundary conditions:

$$\left(-\frac{\partial\eta}{\partial t} + \frac{\partial\phi^\mathrm{in}}{\partial r}\right)_{r=R_\mathrm{d}} = \left(-\frac{\partial\eta}{\partial t} + \frac{\partial\phi^\mathrm{out}}{\partial r}\right)_{r=R_\mathrm{d}} = 0 \tag{C-58}$$

linearized pressure boundary conditions:

$$\rho_\mathrm{a}\left(\frac{\partial\phi^\mathrm{out}(r,\theta,t)}{\partial t}\right)_{r=R_\mathrm{d}} - \rho_\mathrm{d}\left(\frac{\partial\phi^\mathrm{in}(r,\theta,t)}{\partial t}\right)_{r=R_\mathrm{d}} = \gamma\left(-\frac{2\eta}{R_\mathrm{d}^2} - \frac{1}{R_\mathrm{d}^2}\cot\theta\frac{\partial\eta}{\partial\theta} - \frac{1}{R_\mathrm{d}^2}\frac{\partial^2\eta}{\partial\theta^2}\right) \tag{C-51}$$

In the following, we will have a theoretical estimation based on the governing equation and the boundary conditions. Traditionally, using the method of separation of variables, we assume that ϕ can be expressed in the form:

$$\phi(r,\theta,t) = \Phi(r)\Psi(\theta)E(t) \tag{C-59}$$

Substituting this form into the Laplace equation yields:

$$\Phi''(r)\Psi(\theta) + \Psi(\theta)\frac{2}{r}\Phi'(r) + \frac{1}{r^2}\cot\theta\Psi'(\theta)\Phi(r) + \frac{1}{r^2}\Psi''(\theta)\Phi(r) = 0 \tag{C-60}$$

As a result, we can find:

$$\frac{\Phi''}{\Phi} + \frac{2}{r}\frac{\Phi'}{\Phi} + \frac{1}{r^2}\cot\theta\frac{\Psi'}{\Psi} + \frac{1}{r^2}\frac{\Psi''}{\Psi} = 0 \tag{C-61}$$

$$r^2\frac{\Phi''}{\Phi} + 2r\frac{\Phi'}{\Phi} = -\left(\frac{\Psi''}{\Psi} + \cot\theta\frac{\Psi'}{\Psi}\right) = l(l+1) \tag{C-62}$$

with l the integer $0,\ 1,\ 2,\ 3$ ...

Now, we have:

$$\frac{d^2\Psi}{d\theta^2} + \cot\theta\frac{d\Psi}{d\theta} + l(l+1)\Psi = 0 \tag{C-63}$$

Let $x = \cos\theta$, with $0 \le \theta \le \pi$ and $-1 \le x \le 1$, and we will have:

$$(1-x^2)\frac{d^2\Psi}{dx^2} - 2x\frac{d\Psi}{dx} + l(l+1)\Psi = 0 \tag{C-64}$$

which is the well-known Legendre's equation. The general solution to this equation is the linear combination of the Legendre functions: $P_l(x)$ and $Q_l(x)$. Then, the equation becomes:

$$\Psi(\theta) = \sum_{l=0}^{\infty} \alpha_l P_l(\cos\theta) + \beta_l Q_l(\cos\theta) \tag{C-65}$$

where $Q_l(x)$ is singular at $x = \pm 1$, we might not consider Q_l.

Then, we come to $\Phi(r)$:

$$r^2\frac{d^2\Phi}{dr^2} + 2r\frac{d\Phi}{dr} - l(l+1)\Phi = 0 \tag{C-66}$$

Notice the structure that $r^2\frac{d^2\Phi}{dr^2}$ and $r\frac{d\Phi}{dr}$, assuming $\Phi = r^\lambda$, we have:

$$[\lambda(\lambda-1)2 + \lambda - l(l+1)]r^\lambda = 0 \tag{C-67}$$

which gives us $\lambda = l$ or $\lambda = -(l+1)$

Thus, we finally find the theoretical expression:

$$\Phi(r) = \sum_{l=0}^{\infty} \alpha_l r^l + \beta_l r^{-(l+1)} \tag{C-68}$$

Adding them together, we have the expression for the velocity potential:

$$\phi(r,\theta,t) = \sum_{l=0}^{\infty} \left[\alpha_l r^l + \beta_l r^{-(l+1)}\right] P_l(\cos\theta) \cdot E_l(t) \tag{C-69}$$

Specifically, in the droplet domain, we have $r \rightarrow 0$:

$$\phi_d(r,\theta,t) = \sum_{l=0}^{\infty} \alpha_l r^l \cdot P_l(\cos\theta) \cdot E_l(t) \tag{C-70}$$

and in the air domain we have $r \rightarrow \infty$:

$$\phi_a(r,\theta,t) = \sum_{l=0}^{\infty} \beta_l r^{-(l+1)} \cdot P_l(\cos\theta) \cdot E_l(t) \tag{C-71}$$

Assume the time-dependent function has the form of $E_l(t) = e^{i\omega_l t}$, we have the specific expressions as:

$$\phi_d(r,\theta,t) = \sum_{l=0}^{\infty} A_l r^l \cdot P_l(\cos\theta) \cdot e^{i\omega_l t} \tag{C-72}$$

$$\phi_a(r,\theta,t) = \sum_{l=0}^{\infty} B_l r^{-(l+1)} \cdot P_l(\cos\theta) \cdot e^{i\omega_l t} \tag{C-73}$$

$$\eta(\theta,t) = \sum_{l=0}^{\infty} C_l \cdot P_l(\cos\theta) \cdot e^{i\omega_l t} \tag{C-74}$$

with the coefficients A_l , B_l and C_l to be determined.

With the specific expressions determined, we have the following boundary conditions.

The kinematic boundary condition gives:

$$i\omega_l C_l P_l(\cos\theta) e^{i\omega_l t} = l A_l {R_\mathrm{d}}^{l-1} \cdot P_l(\cos\theta) \cdot e^{i\omega_l t} = -(l+1) B_l {R_\mathrm{d}}^{-(l+2)} \cdot P_l(\cos\theta) \cdot e^{i\omega_l t} \tag{C-75}$$

The pressure boundary condition gives:

$$\rho_a i\omega_l B_l {R_\mathrm{d}}^{-(l+1)} \cdot P_l(\cos\theta) \cdot e^{i\omega_l t} - \rho_d i\omega_l {R_\mathrm{d}}^{l} \cdot P_l(\cos\theta) \cdot e^{i\omega_l t} = -\frac{\gamma}{R_\mathrm{d}^2} C_l \cdot e^{i\omega_l t} (2 - l - l^2) P_l(\cos\theta) \tag{C-76}$$

Now we have:

$$i\omega_l C_l = l A_l {R_\mathrm{d}}^{l-1} \tag{C-77}$$

$$lA_l{R_\mathrm{d}}^{l-1} = -(l+1)B_l{R_\mathrm{d}}^{-(l+2)} \tag{C-78}$$

$$\rho_\mathrm{a} i\omega_l B_l {R_\mathrm{d}}^{-(l+1)} - \rho_\mathrm{d} i\omega_l {R_\mathrm{d}}^{l} = -\frac{\gamma}{R_\mathrm{d}^2} C_l(l+2)(l-1) \tag{C-79}$$

Three equations can be solved for three unknowns A_l , B_l and C_l. At last, we obtain the well-known dispersion relation, which descripts the free oscillation of a spherical droplet.

$$\omega_l^2 = \frac{\gamma}{{R_\mathrm{d}}^3}\frac{l(l+1)(l+2)(l-1)}{(l+1)\rho_\mathrm{d}+l\rho_\mathrm{a}} \tag{C-80}$$

Bibliography

[1] D. Zang, S. Tarafdar, Y.Y. Tarasevich, M.D. Choudhury, T. Dutta, Evaporation of a Droplet: From physics to applications, Physics Reports, 804 (2019) 1-56.

[2] G. Hubbard, V. Denny, A. Mills, Droplet evaporation: effects of transients and variable properties, International journal of heat and mass transfer, 18(9) (1975) 1003-1008.

[3] G. McHale, S. Aqil, N. Shirtcliffe, M. Newton, H.Y. Erbil, Analysis of droplet evaporation on a superhydrophobic surface, Langmuir, 21(24) (2005) 11053-11060.

[4] X. He, J. Cheng, C. Patrick Collier, B.R. Srijanto, D.P. Briggs, Evaporation of squeezed water droplets between two parallel hydrophobic/superhydrophobic surfaces, Journal of Colloid and Interface Science, 576 (2020) 127-138.

[5] X. He, J. Cheng, Evaporation-triggered directional transport of asymmetrically confined droplets, Journal of Colloid and Interface Science, 604 (2021) 550-561.

[6] R. Enright, N. Miljkovic, J. Sprittles, K. Nolan, R. Mitchell, E.N. Wang, How coalescing droplets jump, ACS nano, 8(10) (2014) 10352-10362.

[7] D. Richard, C. Clanet, D. Quéré, Contact time of a bouncing drop, Nature, 417(6891) (2002) 811-811.

[8] X. He, L. Zhao, J. Cheng, Coalescence-Induced Swift Jumping of Nanodroplets on Curved Surfaces, Langmuir, 35(30) (2019) 9979-9987.

[9] S. Herbert, S. Fischer, T. Gambaryan-Roisman, P. Stephan, Local heat transfer and phase change phenomena during single drop impingement on a hot surface, International Journal of Heat and Mass Transfer, 61 (2013) 605-614.

[10] S. Daniel, M.K. Chaudhury, J.C. Chen, Fast drop movements resulting from the phase change on a gradient surface, Science, 291(5504) (2001) 633-636.

[11] H.J. Cho, D.J. Preston, Y. Zhu, E.N. Wang, Nanoengineered materials for liquid–vapour phase-change heat transfer, Nature Reviews Materials, 2(2) (2016) 1-17.

[12] Q. Sun, D. Wang, Y. Li, J. Zhang, S. Ye, J. Cui, L. Chen, Z. Wang, H.-J. Butt, D. Vollmer, Surface charge printing for programmed droplet transport, Nature materials, 18(9) (2019) 936-941.

[13] R.G. Larson, Transport and deposition patterns in drying sessile droplets, AIChE Journal, 60(5) (2014) 1538-1571.

[14] D. Attinger, C. Frankiewicz, A.R. Betz, T.M. Schutzius, R. Ganguly, A. Das, C.-J. Kim, C.M. Megaridis, Surface engineering for phase change heat transfer: A review, MRS Energy & Sustainability, 1 (2014) E4.

[15] H. Liu, Science and Engineering of Droplets:: Fundamentals and Applications, William Andrew, 1999.

[16] X.-M. Li, D. Reinhoudt, M. Crego-Calama, What do we need for a superhydrophobic surface? A review on the recent progress in the preparation of superhydrophobic surfaces, Chemical Society Reviews, 36(8) (2007) 1350-1368.

[17] P. Roach, N.J. Shirtcliffe, M.I. Newton, Progess in superhydrophobic surface development, Soft matter, 4(2) (2008) 224-240.

[18] D. Quéré, Wetting and roughness, Annu. Rev. Mater. Res., 38(1) (2008) 71-99.

[19] A. Cazabat, M.C. Stuart, Dynamics of wetting: effects of surface roughness, The Journal of Physical Chemistry, 90(22) (1986) 5845-5849.

[20] K. Kubiak, M. Wilson, T. Mathia, P. Carval, Wettability versus roughness of engineering surfaces, Wear, 271(3-4) (2011) 523-528.

[21] T. Young, III. An essay on the cohesion of fluids, Philosophical transactions of the royal society of London, (95) (1805) 65-87.

[22] R.N. Wenzel, Resistance of solid surfaces to wetting by water, Industrial & engineering chemistry, 28(8) (1936) 988-994.

[23] A. Cassie, S. Baxter, Wettability of porous surfaces, Transactions of the Faraday society, 40 (1944) 546-551.

[24] R. Mangel, E. Baer, The evaporation of water drops from a" Teflon" surface, Chemical Engineering Science, 17(9) (1962) 705-706.

[25] R. Picknett, R. Bexon, The evaporation of sessile or pendant drops in still air, Journal of colloid and Interface Science, 61(2) (1977) 336-350.

[26] Y.O. Popov, Evaporative deposition patterns: Spatial dimensions of the deposit, Physical Review E, 71(3) (2005) 036313.

[27] C. Snow, Potential problems and capacitance for a conductor bounded by two intersecting spheres, Journal of Research of the National Bureau of Standards, 43 (1949) 337.

[28] D. Quéré, Leidenfrost dynamics, Annual Review of Fluid Mechanics, 45(1) (2013) 197-215.

[29] A.-L. Biance, C. Clanet, D. Quéré, Leidenfrost drops, Physics of fluids, 15(6) (2003) 1632-1637.

[30] B. Gottfried, C. Lee, K. Bell, The Leidenfrost phenomenon: film boiling of liquid droplets on a flat plate, International Journal of heat and mass transfer, 9(11) (1966) 1167-1188.

[31] N. Farokhnia, S.M. Sajadi, P. Irajizad, H. Ghasemi, Decoupled hierarchical structures for suppression of Leidenfrost phenomenon, Langmuir, 33(10) (2017) 2541-2550.

[32] M. Jiang, Y. Wang, F. Liu, H. Du, Y. Li, H. Zhang, S. To, S. Wang, C. Pan, J. Yu, Inhibiting the Leidenfrost effect above 1,000 C for sustained thermal cooling, Nature, 601(7894) (2022) 568-572.

[33] W. Huang, L. Zhao, X. He, Y. Li, C.P. Collier, Z. Zheng, J. Liu, D.P. Briggs, J. Cheng, Low-temperature Leidenfrost-like jumping of sessile droplets on microstructured surfaces, Nature Physics, (2024) 1-8.

[34] D. Khojasteh, M. Kazerooni, S. Salarian, R. Kamali, Droplet impact on superhydrophobic surfaces: A review of recent developments, Journal of industrial and engineering chemistry, 42 (2016) 1-14.

[35] J.B. Boreyko, C.-H. Chen, Self-propelled dropwise condensate on superhydrophobic surfaces, Physical review letters, 103(18) (2009) 184501.

[36] P. Calvert, Inkjet Printing for Materials and Devices, Chem. Mater., 13(10) (2001) 3299-3305.

[37] A. Wu, L. Yu, Z. Li, H. Yang, E. Wang, Atomic force microscope investigation of large-circle DNA molecules, Anal Biochem, 325(2) (2004) 293-300.

[38] W. Jia, H.H. Qiu, Experimental investigation of droplet dynamics and heat transfer in spray cooling, Exp. Therm. Fluid Sci., 27(7) (2003) 829-838.

[39] J. Song, W. Cheng, M. Nie, X. He, W. Nam, J. Cheng, W. Zhou, Partial Leidenfrost Evaporation-Assisted Ultrasensitive Surface-Enhanced Raman Spectroscopy in a Janus Water Droplet on Hierarchical Plasmonic Micro-/Nanostructures, ACS Nano, 14(8) (2020) 9521-9531.

[40] S.A. Putnam, A.M. Briones, L.W. Byrd, J.S. Ervin, M.S. Hanchak, A. White, J.G. Jones, Microdroplet evaporation on superheated surfaces, International Journal of Heat and Mass Transfer, 55(21) (2012) 5793-5807.

[41] P. Tsai, R.G. Lammertink, M. Wessling, D. Lohse, Evaporation-triggered wetting transition for water droplets upon hydrophobic microstructures, Physical review letters, 104(11) (2010) 116102.

[42] L. Zhao, J. Cheng, The mechanism and universal scaling law of the contact line friction for the Cassie-state droplets on nanostructured ultrahydrophobic surfaces, Nanoscale, 10(14) (2018) 6426-6436.

[43] L.S. Lam, M. Hodes, R. Enright, Analysis of Galinstan-Based Microgap Cooling Enhancement Using Structured Surfaces, Journal of Heat Transfer, 137(9) (2015).

[44] A. Al-Sharafi, B.S. Yilbas, H. Ali, Droplet Heat Transfer on Micropost Arrays With Hydrophobic and Hydrophilic Characteristics, Journal of Heat Transfer, 140(7) (2018).

[45] L. Bansal, S. Chakraborty, S. Basu, Confinement-induced alterations in the evaporation dynamics of sessile droplets, Soft Matter, 13(5) (2017) 969-977.

[46] S. Semenov, F. Carle, M. Medale, D. Brutin, Boundary conditions for a one-sided numerical model of evaporative instabilities in sessile drops of ethanol on heated substrates, Phys Rev E, 96(6-1) (2017) 063113.

[47] P.a. Bexon, The Evaporation of Sessile or Pendant Drops in Still Air, Journal of Colloid and Interface Science, 61(2) (1977) 336-350.

[48] M.E.R. Shanahan, Simple Theory of "Stick-Slip" Wetting Hysteresis, Langmuir, 11(3) (1995) 1041-1043.

[49] N.N. Lebedev, Special Functions and Their Applications, Prentice-Hall, Englewood Cliffs, NJ, USA, 1965.

[50] R.G.L. Hua Hu, Evaporation of a Sessile droplet on a substrate, J Phys Chem B, 106 (2002) 1334-1344.

[51] Robert D. Deegan, Olgica Bakajin, Todd F. Dupont, Greg Huber, Sidney R. Nagel, T.A. Witten, Contact line deposits in an evaporating drop, Phys Rev E, 62 (2000).

[52] Y.O. Popov, Evaporative deposition patterns: spatial dimensions of the deposit, Phys. Rev. E 71(3) (2005) 1-17.

[53] M.A. Kadhim, N. Kapur, J.L. Summers, H. Thompson, Experimental and Theoretical Investigation of Droplet Evaporation on Heated Hydrophilic and Hydrophobic Surfaces, Langmuir, 35(19) (2019) 6256-6266.

[54] T.A.H. Nguyen, A.V. Nguyen, M.A. Hampton, Z.P. Xu, L. Huang, V. Rudolph, Theoretical and experimental analysis of droplet evaporation on solid surfaces, Chemical Engineering Science, 69(1) (2012) 522-529.

[55] H. Gelderblom, Á.G. Marín, H. Nair, A. van Houselt, L. Lefferts, J.H. Snoeijer, D. Lohse, How water droplets evaporate on a superhydrophobic substrate, Physical Review E, 83(2) (2011) 026306.
[56] S. Dash, S.V. Garimella, Droplet evaporation on heated hydrophobic and superhydrophobic surfaces, Phys Rev E, 89 (2014) 042402.
[57] S. Dash, S.V. Garimella, Droplet evaporation dynamics on a superhydrophobic surface with negligible hysteresis, Langmuir, 29(34) (2013) 10785-10795.
[58] A. Aldhaleai, F. Khan, T. Thundat, P.A. Tsai, Evaporation dynamics of water droplets on superhydrophobic nanograss surfaces, International Journal of Heat and Mass Transfer, 160 (2020).
[59] K. Gleason, H. Voota, S.A. Putnam, Steady-state droplet evaporation: Contact angle influence on the evaporation efficiency, International Journal of Heat and Mass Transfer, 101 (2016) 418-426.
[60] G. McHale, S. Aqil, N.J. Shirtcliffe, M.I. Newton, H.Y. Erbil, Analysis of droplet evaporation on a superhydrophobic surface, Langmuir, 21 (2005) 11053-11060.
[61] S. Adera, R. Raj, R. Enright, E.N. Wang, Non-wetting droplets on hot superhydrophilic surfaces, Nat. Commun., 4 (2013) 2518.
[62] M. Wei, Y. Song, Y. Zhu, D.J. Preston, C.S. Tan, E.N. Wang, Heat transfer suppression by suspended droplets on microstructured surfaces, Applied Physics Letters, 116(23) (2020).
[63] H.-m. Kwon, J.C. Bird, K.K. Varanasi, Increasing Leidenfrost point using micro-nano hierarchical surface structures, Applied Physics Letters, 103(20) (2013).
[64] M. Badv, I.H. Jaffer, J.I. Weitz, T.F. Didar, An omniphobic lubricant-infused coating produced by chemical vapor deposition of hydrophobic organosilanes attenuates clotting on catheter surfaces, Sci. Rep., 7(1) (2017) 11639.
[65] R. Hays, D. Maynes, J. Crockett, Thermal transport to droplets on heated superhydrophobic substrates, Int. J. Heat Mass Transfer, 98 (2016) 70-80.
[66] Y. Maeda, F. Lv, P. Zhang, Y. Takata, D. Orejon, Condensate droplet size distribution and heat transfer on hierarchical slippery lubricant infused porous surfaces, Applied Thermal Engineering, 176 (2020) 115386.
[67] Seri Lee, Seaho Song, Van Au, K.P. Moran, Constriction Spreading resistance model for electroics packing, in: ASME/JSME Thermal Engineering Conference, 1995.
[68] D.P. Kennedy, Spreading Resistance in Cylindrical Semiconductor Devices, Journal of Applied Physics, 31(8) (1960) 1490-1497.
[69] M. di Marzo, D.D. Evans, Evaporation of a water droplet deposited on a hot high thermal conductivity solid surface, United States, 1986.
[70] K.M. Itaru Michiyoshe, Heat transfer characteristics of evaporation of a liquid droplet on heated surfaces, international Journal of Heat and Mass Transfer, 21 (1977) 605-613.
[71] M. Seki, H. Kawamura, K. Sanokawa, Transient temperature profile of a hot wall due to an impinging liquid droplet, Journal of Heat Transfer, 100 (1987) 167-169.
[72] K. Gleason, S.A. Putnam, Microdroplet evaporation with a forced pinned contact line, Langmuir, 30(34) (2014) 10548-10555.

[73] P.J. Sáenz, K. Sefiane, J. Kim, O.K. Matar, P. Valluri, Evaporation of sessile drops: a three-dimensional approach, Journal of Fluid Mechanics, 772 (2015) 705-739.

[74] W.A.S. B. Abrambon, Droplet vaporization model for spray combusition calculations, International Journal of Heat and Mass Transfer, 32 (1989) 1605-1618.

[75] D.A. del Cerro, A.G. Marin, G.R. Romer, B. Pathiraj, D. Lohse, A.J. Huis in 't Veld, Leidenfrost point reduction on micropatterned metallic surfaces, Langmuir, 28(42) (2012) 15106-15110.

[76] S.H. Kim, H. Seon Ahn, J. Kim, M. Kaviany, M. Hwan Kim, Dynamics of water droplet on a heated nanotubes surface, Applied Physics Letters, 102(23) (2013).

[77] J.G. Leidenfrost, De aquae communis nonnullis qualitatibus tractatus, Ovenius, 1756.

[78] J.G. Leidenfrost, On the fixation of water in diverse fire, International Journal of Heat and Mass Transfer, 9(11) (1966) 1153-1166.

[79] I.U. Vakarelski, N.A. Patankar, J.O. Marston, D.Y. Chan, S.T. Thoroddsen, Stabilization of Leidenfrost vapour layer by textured superhydrophobic surfaces, Nature, 489(7415) (2012) 274-277.

[80] G. Liang, I. Mudawar, Review of spray cooling–Part 1: Single-phase and nucleate boiling regimes, and critical heat flux, International Journal of Heat and Mass Transfer, 115 (2017) 1174-1205.

[81] R. Abdelaziz, D. Disci-Zayed, M.K. Hedayati, J.-H. Pöhls, A.U. Zillohu, B. Erkartal, V.S.K. Chakravadhanula, V. Duppel, L. Kienle, M. Elbahri, Green chemistry and nanofabrication in a levitated Leidenfrost drop, Nature Communications, 4(1) (2013) 2400.

[82] Y.Y. Jiang, C.C. Wu, L.R. Li, K. Wang, Z. Tao, F. Gao, W.F. Cheng, J.T. Cheng, X.Y. Zhao, S. Priya, W.W. Deng, All electrospray printed perovskite solar cells, Nano Energy, 53 (2018) 440-448.

[83] P. Galliker, J. Schneider, H. Eghlidi, S. Kress, V. Sandoghdar, D. Poulikakos, Direct printing of nanostructures by electrostatic autofocussing of ink nanodroplets, Nature communications, 3(1) (2012) 890.

[84] D. Quéré, Wetting and roughness, Annu. Rev. Mater. Res., 38 (2008) 71-99.

[85] A. Bouillant, T. Mouterde, P. Bourrianne, A. Lagarde, C. Clanet, D. Quéré, Leidenfrost wheels, Nature Physics, 14(12) (2018) 1188-1192.

[86] P. Bourrianne, C. Lv, D. Quéré, The cold Leidenfrost regime, Science Advances, 5(6) (2019) eaaw0304.

[87] H. Linke, B. Alemán, L. Melling, M. Taormina, M. Francis, C. Dow-Hygelund, V. Narayanan, R. Taylor, A. Stout, Self-propelled Leidenfrost droplets, Physical review letters, 96(15) (2006) 154502.

[88] G. Lagubeau, M. Le Merrer, C. Clanet, D. Quéré, Leidenfrost on a ratchet, Nature Physics, 7(5) (2011) 395-398.

[89] R.A. Cengel, Introduction to thermodynamics and heat transfer, McGraw-Hill, 2008.

[90] V.K. Dhir, BOILING HEAT TRANSFER, Annual Review of Fluid Mechanics, 30(1) (1998) 365-401.

[91] D. Arnaldo del Cerro, Á.G. Marín, G.R. Römer, B. Pathiraj, D. Lohse, A.J. Huis in't Veld, Leidenfrost point reduction on micropatterned metallic surfaces, Langmuir, 28(42) (2012) 15106-15110.

[92] J. Li, Y. Hou, Y. Liu, C. Hao, M. Li, M.K. Chaudhury, S. Yao, Z. Wang, Directional transport of high-temperature Janus droplets mediated by structural topography, Nature Physics, 12(6) (2016) 606-612.

[93] C. Liu, C. Lu, Z. Yuan, C. Lv, Y. Liu, Steerable drops on heated concentric microgroove arrays, Nature Communications, 13(1) (2022) 3141.

[94] M. Bohnet, Fouling of heat transfer surfaces, Chemical engineering & technology, 10(1) (1987) 113-125.

[95] Y. Lu, S. Sathasivam, J. Song, C.R. Crick, C.J. Carmalt, I.P. Parkin, Robust self-cleaning surfaces that function when exposed to either air or oil, Science, 347(6226) (2015) 1132-1135.

[96] D. Tian, Y. Song, L. Jiang, Patterning of controllable surface wettability for printing techniques, Chemical society reviews, 42(12) (2013) 5184-5209.

[97] D.E. Kim, D.I. Yu, D.W. Jerng, M.H. Kim, H.S. Ahn, Review of boiling heat transfer enhancement on micro/nanostructured surfaces, Experimental Thermal and Fluid Science, 66 (2015) 173-196.

[98] A. Prosperetti, Vapor bubbles, Annual review of fluid mechanics, 49 (2017) 221-248.

[99] V.P. Carey, Liquid-vapor phase-change phenomena: an introduction to the thermophysics of vaporization and condensation processes in heat transfer equipment, CRC Press, 2020.

[100] J.T. Cheng, A. Vandadi, C.L. Chen, Condensation heat transfer on two-tier superhydrophobic surfaces, Appl Phys Lett, 101(13) (2012).

[101] R.N. Wenzel, Surface roughness and contact angle, The Journal of Physical Chemistry, 53(9) (1949) 1466-1467.

[102] D. Saranadhi, D. Chen, J.A. Kleingartner, S. Srinivasan, R.E. Cohen, G.H. McKinley, Sustained drag reduction in a turbulent flow using a low-temperature Leidenfrost surface, Science Advances, 2(10) (2016) e1600686.

[103] S. Adera, R. Raj, R. Enright, E.N. Wang, Non-wetting droplets on hot superhydrophilic surfaces, Nature Communications, 4(1) (2013) 2518.

[104] D. Harvey, J.M. Harper, J.C. Burton, Minimum Leidenfrost Temperature on Smooth Surfaces, Physical Review Letters, 127(10) (2021) 104501.

[105] G. Graeber, K. Regulagadda, P. Hodel, C. Küttel, D. Landolf, T.M. Schutzius, D. Poulikakos, Leidenfrost droplet trampolining, Nature Communications, 12(1) (2021) 1727.

[106] N.S. Dhillon, J. Buongiorno, K.K. Varanasi, Critical heat flux maxima during boiling crisis on textured surfaces, Nature Communications, 6(1) (2015) 8247.

[107] A. Benusiglio, D. Quéré, C. Clanet, Explosions at the water surface, Journal of Fluid Mechanics, 752 (2014) 123-139.

[108] K. Okumura, F. Chevy, D. Richard, D. Quéré, C. Clanet, Water spring: A model for bouncing drops, Europhysics Letters, 62(2) (2003) 237.

[109] M.A.J. van Limbeek, M. Shirota, P. Sleutel, C. Sun, A. Prosperetti, D. Lohse, Vapour cooling of poorly conducting hot substrates increases the dynamic Leidenfrost temperature, International Journal of Heat and Mass Transfer, 97 (2016) 101-109.

[110] J.T. Pham, M. Paven, S. Wooh, T. Kajiya, H.-J. Butt, D. Vollmer, Spontaneous jumping, bouncing and trampolining of hydrogel drops on a heated plate, Nature Communications, 8(1) (2017) 905.

[111] T.M. Schutzius, S. Jung, T. Maitra, G. Graeber, M. Köhme, D. Poulikakos, Spontaneous droplet trampolining on rigid superhydrophobic surfaces, Nature, 527(7576) (2015) 82-85.

[112] J.F. Joanny, P.G. de Gennes, A model for contact angle hysteresis, The Journal of Chemical Physics, 81(1) (1984) 552-562.

[113] P.J. Yunker, T. Still, M.A. Lohr, A.G. Yodh, Suppression of the coffee-ring effect by shape-dependent capillary interactions, Nature, 476(7360) (2011) 308-311.

[114] L. Bourouiba, The Fluid Dynamics of Disease Transmission, Annual Review of Fluid Mechanics, 53(Volume 53, 2021) (2021) 473-508.

[115] E.J. Baack, To succeed globally, disperse locally: effects of local pollen and seed dispersal on tetraploid establishment, Heredity, 94(5) (2005) 538-546.

[116] L.L. English, Some properties of oil emulsions influencing insecticidal efficiency, Illinois Natural History Survey Bulletin; v. 017, no. 05, (1928).

[117] V. Bergeron, D. Bonn, J.Y. Martin, L. Vovelle, Controlling droplet deposition with polymer additives, Nature, 405(6788) (2000) 772-775.

[118] R. Blossey, Self-cleaning surfaces—virtual realities, Nature materials, 2(5) (2003) 301-306.

[119] W. Huang, L. Zhao, X. He, Y. Li, C.P. Collier, Z. Zheng, J. Liu, D.P. Briggs, J. Cheng, Low-temperature Leidenfrost-like jumping of sessile droplets on microstructured surfaces, Nature Physics, 20(8) (2024) 1274-1281.

[120] X. Deng, L. Mammen, H.-J. Butt, D. Vollmer, Candle Soot as a Template for a Transparent Robust Superamphiphobic Coating, Science, 335(6064) (2012) 67-70.

[121] D. Lohse, Fundamental Fluid Dynamics Challenges in Inkjet Printing, Annual Review of Fluid Mechanics, 54(Volume 54, 2022) (2022) 349-382.

[122] H. Sirringhaus, T. Kawase, R. Friend, T. Shimoda, M. Inbasekaran, W. Wu, E.P. Woo, High-resolution inkjet printing of all-polymer transistor circuits, Science, 290(5499) (2000) 2123-2126.

[123] R.D. Reitz, Directions in internal combustion engine research, Combustion and Flame, 160(1) (2013) 1-8.

[124] N. Miljkovic, R. Enright, Y. Nam, K. Lopez, N. Dou, J. Sack, E.N. Wang, Jumping-Droplet-Enhanced Condensation on Scalable Superhydrophobic Nanostructured Surfaces, Nano Letters, 13(1) (2013) 179-187.

[125] E. Villermaux, Fragmentation, Annual Review of Fluid Mechanics, 39(Volume 39, 2007) (2007) 419-446.

[126] A.L. Yarin, DROP IMPACT DYNAMICS: Splashing, Spreading, Receding, Bouncing…, Annual Review of Fluid Mechanics, 38(Volume 38, 2006) (2006) 159-192.

[127] C. Josserand, S.T. Thoroddsen, Drop Impact on a Solid Surface, Annual Review of Fluid Mechanics, 48(1) (2016) 365-391.

[128] X. Cheng, T.-P. Sun, L. Gordillo, Drop Impact Dynamics: Impact Force and Stress Distributions, Annual Review of Fluid Mechanics, 54(Volume 54, 2022) (2022) 57-81.

[129] J.E. Sprittles, Gas Microfilms in Droplet Dynamics: When Do Drops Bounce?, Annual Review of Fluid Mechanics, 56(Volume 56, 2024) (2024) 91-118.

[130] J. Eggers, J.E. Sprittles, J.H. Snoeijer, Coalescence Dynamics, Annual Review of Fluid Mechanics, (2024).

[131] P.-G. Gennes, F. Brochard-Wyart, D. Quéré, Capillarity and wetting phenomena: drops, bubbles, pearls, waves, Springer, 2004.

[132] A.-L. Biance, F. Chevy, C. Clanet, G. Lagubeau, D. QuÉRÉ, On the elasticity of an inertial liquid shock, Journal of Fluid Mechanics, 554 (2006) 47-66.

[133] V. Sanjay, P. Chantelot, D. Lohse, When does an impacting drop stop bouncing?, Journal of Fluid Mechanics, 958 (2023) A26.

[134] J.C. Bird, R. Dhiman, H.-M. Kwon, K.K. Varanasi, Reducing the contact time of a bouncing drop, Nature, 503(7476) (2013) 385-388.

[135] H. Vahabi, W. Wang, J.M. Mabry, A.K. Kota, Coalescence-induced jumping of droplets on superomniphobic surfaces with macrotexture, Science Advances, 4(11) (2018) eaau3488.

[136] X.K. He, L. Zhao, J.T. Cheng, Coalescence-Induced Swift Jumping of Nanodroplets on Curved Surfaces, Langmuir, 35(30) (2019) 9979-9987.

[137] T. Mouterde, T.-V. Nguyen, H. Takahashi, C. Clanet, I. Shimoyama, D. Quéré, How merging droplets jump off a superhydrophobic surface: Measurements and model, Physical Review Fluids, 2(11) (2017) 112001.

[138] R. Mukherjee, A.S. Berrier, K.R. Murphy, J.R. Vieitez, J.B. Boreyko, How Surface Orientation Affects Jumping-Droplet Condensation, Joule, 3(5) (2019) 1360-1376.

[139] X. Yan, Y. Qin, F. Chen, G. Zhao, S. Sett, M.J. Hoque, K.F. Rabbi, X. Zhang, Z. Wang, L. Li, F. Chen, J. Feng, N. Miljkovic, Laplace Pressure Driven Single-Droplet Jumping on Structured Surfaces, ACS Nano, 14(10) (2020) 12796-12809.

[140] J.C. Bird, R. de Ruiter, L. Courbin, H.A. Stone, Daughter bubble cascades produced by folding of ruptured thin films, Nature, 465(7299) (2010) 759-762.

[141] N. Savva, J.W.M. Bush, Viscous sheet retraction, Journal of Fluid Mechanics, 626 (2009) 211-240.

[142] J.M. Gordillo, J. Rodríguez-Rodríguez, Capillary waves control the ejection of bubble bursting jets, Journal of Fluid Mechanics, 867 (2019) 556-571.

[143] A. Gauthier, S. Symon, C. Clanet, D. Quéré, Water impacting on superhydrophobic macrotextures, Nature Communications, 6(1) (2015) 8001.

[144] S. Popinet, Gerris: a tree-based adaptive solver for the incompressible Euler equations in complex geometries, Journal of Computational Physics, 190(2) (2003) 572-600.

[145] S. Popinet, An accurate adaptive solver for surface-tension-driven interfacial flows, Journal of Computational Physics, 228(16) (2009) 5838-5866.

[146] J.M. Gordillo, F.J. Blanco-Rodríguez, Theory of the jets ejected after the inertial collapse of cavities with applications to bubble bursting jets, Physical Review Fluids, 8(7) (2023) 073606.
[147] M.A. Hack, P. Vondeling, M. Cornelissen, D. Lohse, J.H. Snoeijer, C. Diddens, T. Segers, Asymmetric coalescence of two droplets with different surface tensions is caused by capillary waves, Physical Review Fluids, 6(10) (2021) 104002.
[148] J.B. Keller, M.J. Miksis, Surface Tension Driven Flows, SIAM Journal on Applied Mathematics, 43(2) (1983) 268-277.
[149] L.D. Landau, E.M. Lifshitz, Fluid Mechanics: Volume 6, Elsevier, 1987.
[150] B. Zhang, V. Sanjay, S. Shi, Y. Zhao, C. Lv, X.-Q. Feng, D. Lohse, Impact Forces of Water Drops Falling on Superhydrophobic Surfaces, Physical Review Letters, 129(10) (2022) 104501.
[151] F. Carle, Flow Motion in Sessile Droplets: Evaporation and Nanoparticles Assembly (Ph. D. thesis), Aix-Marseille University, (2014).
[152] D.J. Watmough, P.W. Fowler, R. Oliver, The thermal scanning of a curved isothermal surface: implications for clinical thermography, Phys Med Biol, 15(1) (1970) 1-8.
[153] W.M. Irvine, J.B. Pollack, Infrared optical properties of water and ice spheres, Icarus, 8(1) (1968) 324-360.
[154] M.F. Modest, Radiative heat transfer, Academic press, 2013.
[155] A. Chandramohan, J.A. Weibel, S.V. Garimella, Spatiotemporal infrared measurement of interface temperatures during water droplet evaporation on a nonwetting substrate, Applied Physics Letters, 110(4) (2017).
[156] J.T. Korhonen, T. Huhtamäki, O. Ikkala, R.H. Ras, Reliable measurement of the receding contact angle, Langmuir, 29(12) (2013) 3858-3863.
[157] W. Tao, Numerical heat transfer, (2001).
[158] J.B. Bell, P. Colella, H.M. Glaz, A second-order projection method for the incompressible navier-stokes equations, Journal of Computational Physics, 85(2) (1989) 257-283.
[159] E. Aulisa, S. Manservisi, R. Scardovelli, S. Zaleski, Interface reconstruction with least-squares fit and split advection in three-dimensional Cartesian geometry, Journal of Computational Physics, 225(2) (2007) 2301-2319.
[160] M.M. Francois, S.J. Cummins, E.D. Dendy, D.B. Kothe, J.M. Sicilian, M.W. Williams, A balanced-force algorithm for continuous and sharp interfacial surface tension models within a volume tracking framework, Journal of Computational Physics, 213(1) (2006) 141-173.
[161] L. Deike, E. Ghabache, G. Liger-Belair, A.K. Das, S. Zaleski, S. Popinet, T. Séon, Dynamics of jets produced by bursting bubbles, Physical Review Fluids, 3(1) (2018) 013603.
[162] J.B. Keller, Breaking of liquid films and threads, The Physics of Fluids, 26(12) (1983) 3451-3453.
[163] S. Basak, P.K. Farsoiya, R. Dasgupta, Jetting in finite-amplitude, free, capillary-gravity waves, Journal of Fluid Mechanics, 909 (2021) A3.